On the wavefront of ultrahigh intensity lasers: spatial contrast and gratings deformation

by

VINCENT LEROUX

A Thesis Submitted to the Faculty of

Mathematics, Informatics and Natural Sciences

Department of Physics

for the Degree of

DOCTOR RERUM NATURALIUM

UNIVERSITÄT HAMBURG

October 2018

Clarification of Work

Hiermit erkläre ich an Eides statt, dass ich die vorliegende Dissertationsschrift selbst verfasst und keine anderen als die angegebenen Quellen und Hilfsmittel benutzt habe.

I hereby declare, on oath, that I have written the present dissertation by my own and have not used other than the acknowledged resources and aids.

Hamburg, 09/10/2018

city and date   *signature, Vincent Leroux*

Acknowledgments and Remerciements

Summarizing experimental research in a publication or a thesis is quite often only the tip of the iceberg. A month or more of painstaking work can be resumed in a few lines. While it is fair to say that only scientific results matter and should be written down, I believe it equally fair to use a few pages to give some recognition to the submerged part of the iceberg and thank the people without which I would not have been able to write this thesis.

First and foremost, I have to thank my supervisor Andreas Maier who gave me the opportunity to work in Hamburg. Andi has managed to put together a team in a very friendly but efficient work environment, which, according to many current and former PhD students I met, is far from easy. I was also part of ELI-Beamlines and therefore I acknowledge the support from Dariusz Kocoń, Lukáš Přibyl, and Georg Korn.

Of course, I acknowledge the whole LUX team for all the help and the discussions, working with them these past years was truly a pleasure. But in particular, I would like to thank Matthias who was with me in the lab from the beginning, Spencer for his great help and the challenging discussions, Philipp and Paul for their unfaltering support, and Manuel and Sören who forced me to think again on what I thought I knew. I spent a lot of time— some might say too much—with these people in building 22, but apparently that was not enough so I also thank them for the great moments we spent away from work.

Enfin, ceux qui me connaissent et qui m'ont côtoyé durant ces dernières années savent que je ne peux pas ne pas laisser quelques mots en français. J'en profite donc pour remercier tout d'abord ma famille et en particulier mes parents Françoise et Marc qui ont toujours soutenu mes choix de carrière, aussi dubitables furent-ils, ainsi que mon frère Bastien avec qui j'ai arrêté de grandir il y a bien longtemps. Je remercie également mes amis de l'autre côté du Rhin qui sont toujours disponibles quand je reviens

en visite (même si parfois ils en ont gros de se faire utiliser bon gré mal gré pour arriver sur la fin), et ceux de ce côté qui me permettent de garder un pied chez moi même à l'étranger.

The years I spent in Hamburg have been filled with new professional and personal experiences, and I am grateful to all those with whom I have been able to share them.

Abstract

The implications of the high repetition rate of the ANGUS 200 TW laser system operated by the University of Hamburg and DESY are studied within the framework of the laser wakefield accelerator LUX. Combined with a non ideal spatial contrast in the focal plane, the repetition rate leads to a fast degradation of the capillary target. We investigate the profile of the far field distribution with a high dynamic range, as well as the source of the discrepancies between the camera measurement and the expected profile derived from the laser wavefront measurement. Furthermore, combined with the high energy of the laser pulses, the repetition rate also leads to a high average power absorbed by the in-vacuum gold coated diffraction gratings used to compress the pulses after amplification. The increase of the substrate temperature then deforms the surface and results in a drastic degradation of the laser divergence and wavefront quality. A broad range parameter scan allows us to define a power threshold above which the deformations of the optics are no longer negligible. Different gratings are finally compared in terms of surface deformation and coating damage threshold.

Zusammenfassung

Die Auswirkungen der hohen Wiederholrate des ANGUS 200 TW Lasersystems bei die Hamburg Universität und DESY werden im Kontext des LUX Laser-Plasma Beschleunigers untersucht. Kombiniert mit einem nicht idealen räumlichen Kontrast in der Brennebene, führt die Wiederholungsrate zu einer schnellen Degradation der Kapillar-Targets. Wir untersuchen das Strahlprofil im Fernfeld mit einem hohen Dynamikbereich, sowie die Quelle der Abweichungen zwischen der Kameramessung und dem erwarteten Profil, das von der Laserwellenfrontmessung abgeleitet wurde. Darüber hinaus führt die Wiederholrate in Kombination mit der hohen Energie der Laserimpulse zu einer hohen absorbierten mittleren Leistung in den goldbeschichteten Beugungsgittern, die verwendet werden um die Impulse nach der Verstärkung im Vakuum zu komprimieren. Die Erhöhung der Substrattemperatur verformt dann die Oberfläche und führt zu einer drastischen Verschlechterung der Laserdivergenz und der Wellenfrontqualität. Parameterscans über einem breiten Bereich ermöglichen es uns, eine Leistungsschwelle zu definieren, über der die Verformungen der Optik nicht mehr vernachlässigbar sind. Unterschiedliche Gitter werden schließlich hinsichtlich der Oberflächenverformung und der Zerstörschwelle der Beschichtung verglichen.

Table of Contents

List of Figures

Chapter 1

Introduction

Since the development of the chirped pulse amplification technique in 1985 [1], the energy contained in ultrashort laser pulses has been steadily increasing. Nowadays, within tens of femtoseconds, laser systems can contain up to 100 J per pulse for large scale facilities such as the European Extreme Light Infrastructure [2], or 1 J and above for projects at a more "reasonable" scale [3]. Such beams can be focused down to reach intensities well above $10^{18}\,\mathrm{W\,cm^{-2}}$, which corresponds to the regime where electrons accelerated by the laser electric field can reach relativistic energies [4], which are interesting for relativistic electron acceleration [5] or high harmonic generation [6], to name only a few. In parallel to the increase of peak power, constant effort has been undertaken to increase the repetition rate, for example by using diode-based pump lasers [7] or thin disks as amplifier medium instead of rods [8]. The increase of repetition rate allows laboratories to move from single-shot proof-of-principle experiments to systematic studies and parameter scans backed up by statistical data, which enable a deeper and more consistent analysis. Furthermore, with the development of high-power laser systems as drivers for secondary sources such as laser-plasma accelerators for instance, increasing the repetition rate is necessary to obtain performances required for applications. Additionally, increasing the repetition rate of laser systems allows for active feedback and therefore a better control of the pulse properties [9].

However, the increase of pulse energy and repetition rate both lead to an increase of average power, which results in a higher thermal expansion of all optics absorbing a fraction of the laser energy. In particular, the gold coated in-vacuum gratings typically used with such laser systems based on titanium-sapphire technology absorb a few percents of the incident pulse energy. Therefore, a few watts of power heats the grating substrate and can only be evacuated by radiative cooling. Through thermal expansion,

1

the surface of the optic will then be deformed, which acts back on the laser pulses as it degrades the reflected wavefront. The deformation of the laser wavefront itself has a direct negative impact on the focusability of the beam, which heavily decreases the available peak intensity as well as the energy contained within the central part of the focal spot. This fraction of the pulse energy is typically a crucial parameter which determines the efficiency of a process [10]. Furthermore, increasing the repetition rate of secondary sources also means that this source should be able to resist against an increasing number of focused high power laser shots. Such a requirement becomes critical for capillary targets where the source characteristics are defined by its geometry. Indeed, the energy of the laser that is not contained within the main peak of its far field distribution would ablate material from the target structure until it becomes unusable. Therefore, the spatial contrast of the laser focused through such target has to be high enough to ensure a reliable long term operation of these secondary sources.

The LUX beamline operated by the University of Hamburg and DESY is such an experiment [11]. Driven by the 200 TW ANGUS laser system, the gas-filled capillary target generates relativistic electron beam in a few millimeters, which can then be sent to an undulator where their wiggling motion generates soft X-rays as a tertiary source. The ANGUS laser is a double CPA titanium-sapphire laser delivering up to 6 J pulses with a repetition rate of 5 Hz. Because the laser has a maximum average power of 30 W, and the beam is being focused in a sub-mm size capillary target, assessing the degradation of the wavefront and the spatial contrast of the focus becomes critical in order to ensure a stable operation of the LUX beamline over several hours. Indeed, to improve the performance of the laser wakefield accelerator, it is necessary to scan a large range of parameters due to the highly non linear nature of this process. Therefore, a high repetition rate is both a blessing and a curse as it allows for fast scans with enough statistics to extract meaningful correlations, but a bad spatial contrast and a large transient deformation of the wavefront drastically limit the lifetime of the experiment. We therefore aim to quantify these two aspects, which is the first step to keep the laser—and thus the electron beam—properties under control.

First, we detail some key concepts of chirped pulse amplification and titanium-sapphire lasers (chapter 2), in order to understand the typical compressor geometry and the necessity of using gold coated gratings. We also explain how to characterize, diagnose, and control the laser wavefront as it is the main diagnostic used in this thesis. Then, we give an overview of

the ANGUS laser and the LUX beamline (chapter 3). The ANGUS system because it is the laser used throughout this work, and the LUX beamline because it is the framework within which all the measurements reported here took place. In fact, our results are not an end in themselves, but a mean to optimize the electron production and the overall performances and stability of the laser wakefield acceleration. We also detail the laser diagnostics which have been extensively used, and use this opportunity to emphasize the necessity of always referencing the measurements to the actual laser beam used for experiments. Keeping this last point in mind, we proceed to measure the intensity distribution of the laser beam in focus, as well as its spatial contrast (chapter 4). We aim to understand the discrepancies between the predictions based on the wavefront measurement and the direct focal spot measurement, and the critical impact of the spatial contrast on the usability of our high repetition rate system for the LUX experiment. Finally, we investigate the transient wavefront degradation of the laser beam due to the heat absorbed by the in-vacuum gold coated gratings (chapter 5). We monitor and model the temperature increase of the substrate itself before studying the effects on the beam divergence and focusability. Nevertheless, our results on grating substrates and coatings give hopes that high power ultrashort laser systems at high repetition rates could use their full potential for the development of stable and reliable secondary sources such as LUX.

Chapter 2

Background

Since the first experimental demonstration of laser radiation in 1960 [12], extensive research has allowed the pulse duration to decrease thanks to the development of Q-switching in 1961 [13] shortly followed by mode locking schemes in 1964 [14]. The first titanium-sapphire (Ti:sapphire) based laser was reported in 1982 [15]. Its large emission bandwidth makes it especially suitable to generate sub-100 fs pulses [16]. Three years later, the chirped pulse amplification (CPA) technique [1] was a major breakthrough in the field of short pulse high power lasers as it allowed femtosecond pulses to be amplified without damaging the optical components by reducing the peak intensity through temporal stretching. This technique is a critical and essential part implemented in all short pulse high energy lasers. Ti:sapphire CPA lasers are now widely used to generate several 100 TW and up to PW pulses with duration below 50 fs at a few Hz repetition rate [3].

As this work is entirely based on a high-power Ti:sapphire system—namely ANGUS—it seems appropriate to review a few key concepts necessary to understand some design decisions. Therefore, after a description of the CPA technique, we focus on the Ti:sapphire specifics. Then a quick overview of the grating technologies gives an comparison between the different processes used to manufacture these critical components. Finally, the laser wavefront measurement and control is described as it is the focus of this work, both in itself to improve the laser beam quality, and as a diagnostic to study dynamic processes.

2.1 Chirped pulse amplification

First described and used to improve radar transmission [17], the chirped pulse amplification (CPA) technique has been successfully applied to optical radiation to overcome the damage threshold of optics in the femtosecond regime. Due to the short pulse duration, light pulses reach intensities high enough to start self-focusing processes when propagating through material like the laser gain medium. Eventually, the intensity is sufficient to permanently damage the optics.

2.1.1 Principle

To avoid the aforementioned effect, the short pulses generated in an oscillator are first stretched: they enter a dispersive device (stretcher) which sends each wavelength on a path with different length before recombining them in a single beam. It imprints on the pulses a linear chirp, meaning the instantaneous frequency depends linearly with time (see figure 2.1). This chirp increases the overall pulse duration, which in turn decreases the peak intensity. For Ti:sapphire systems, the pulses are typically stretched from tens of fs to a few 100 ps, which corresponds to a group delay dispersion (GDD) of roughly $1\,\mathrm{ps}^2$. They are then amplified and finally re-compressed in a compressor. The compressor is analogous to the stretcher and imprints the opposite chirp to overlap all the wavelengths in time. We finally obtain amplified short pulses while avoiding damage to optics and change to the pulse properties through self-focusing. Figure 2.2 is a simplified schematic of a typical CPA system.

The stretcher and compressor are both composed of dispersive optics which are typically diffraction gratings. Prisms are also widely used as well as chirped mirrors, but gratings are usually preferred for high-power system as the high-intensity can lead to nonlinear effects when propagating through a medium for instance. As the ANGUS laser uses a grating compressor and stretcher, this section only focuses on their characteristics. Due to practical considerations, the stretcher imprints a positive chirp (the lower frequencies/longer wavelengths are in front of the higher frequencies/shorter wavelengths), and the compressor a negative chirp. For high power systems, the peak power of the pulse after amplification and compression is so high that self-focusing processes would start simply by propagating the beam through air, leading eventually to air breakdown which would spoil both the temporal and spatial quality of the laser beam. Therefore, after amplification, the final compression is done in a vacuum environment.

6
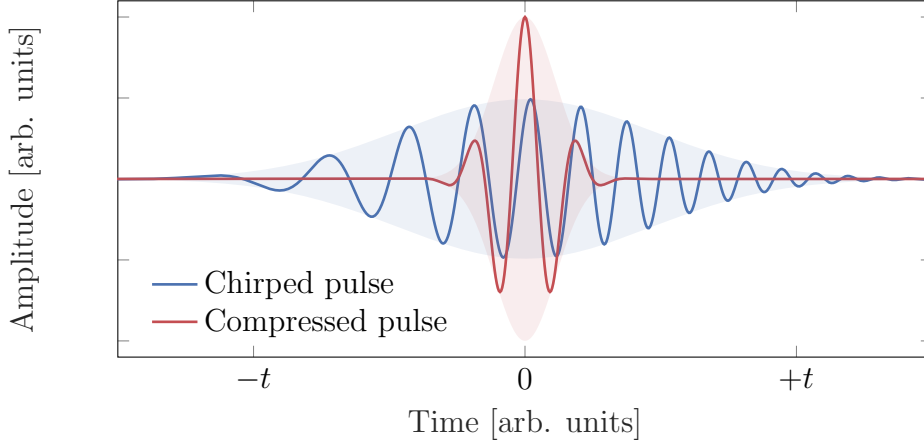
Figure 2.1: Electric field of an arbitrary positively chirped pulse (blue line). The field oscillates more slowly at the front of the pulse (left) than at the back (right). The compressed pulse (red line) has the same spectral content and energy as the chirped pulse. The field amplitude is overlaid as a shaded area.

2.1.2 Grating diffraction theory

For a single grating, the angle of propagation of the diffracted orders can be predicted using the grating equation:

$$\sin \theta_m = \frac{m\lambda}{d} + \sin \theta_i, \tag{2.1}$$

with θ_m the angle between the direction of the diffracted order m and the normal to the surface, θ_i the angle between the direction of the incident wave and the normal to the surface, λ the wavelength and d the grating period. The grating period is usually specified by its inverse, the groove density in lines/mm. Obviously, this equation is only valid if

$$\left| \frac{m\lambda}{d} + \sin \theta_i \right| \leq 1. \tag{2.2}$$

If m is such that this condition is not respected, then the associated diffracted order cannot propagate and corresponds to an evanescent wave. Indeed, one can derive the expression of the wave vector of an incident plane wave using the periodic structure of the grating and extract its component along the normal of the grating surface k_y (see [18] for the complete derivation). For a reflection grating in vacuum, we obtain:

$$k_y = \sqrt{\left(\frac{2\pi}{\lambda} \right)^2 - k_m^2}, \tag{2.3}$$

7
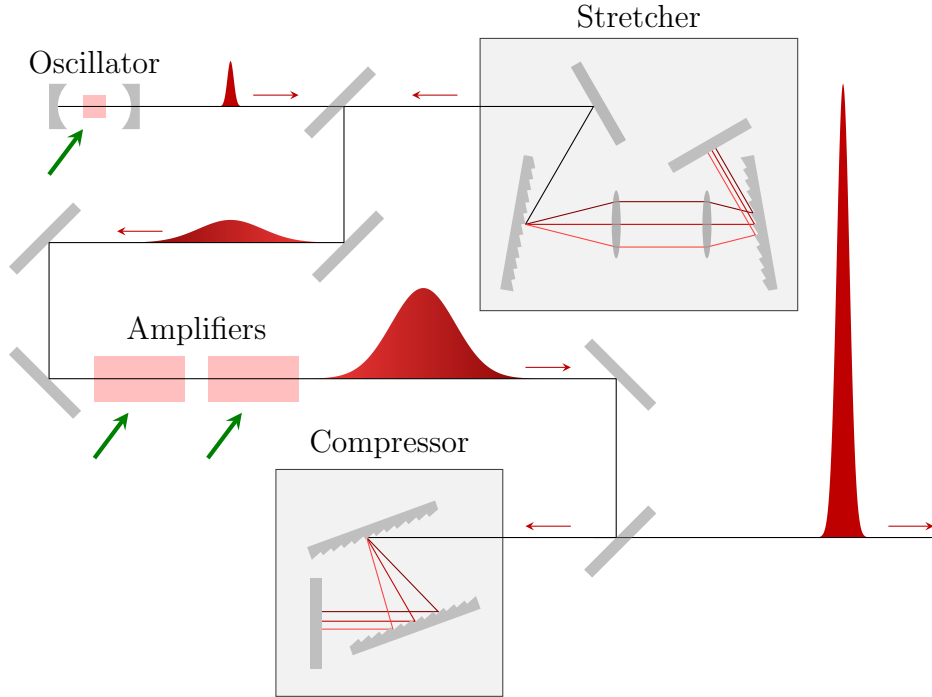
Figure 2.2: Schematic of chirped pulse amplification. The initial short pulse coming from an oscillator is first stretched, then amplified and finally re-compressed. We then obtain a high energy short pulse. To produce a positive chirp in the stretcher (the long wavelengths travel a shorter distance than the short wavelengths), it is necessary to use curved optics. Here the first grating is in the object focal plane of two-lenses telescope and the second grating is placed before the image focal plane. By placing it after the focal plane, a negative chirp would have been added to the pulse.

with $k_m = \frac{2\pi}{\lambda} \sin \theta_m$ the wave vector amplitude of the diffracted order m. If the condition 2.2 is not met, k_y is imaginary and therefore, the wave is evanescent.

For $m = 0$, this condition is always met. This corresponds to the specular or Fresnel reflection which is always propagating and where the beam is not diffracted as it does not depends on the grooves density or the wavelength at all. If the grating is such that $d \ll \lambda$, only the specular propagates. On the other hand, if $d \gg \lambda$ many orders will propagate. Figure 2.3a shows a configuration where four orders are propagating, namely from the -2nd up to the 1st order. Two incidence angle ($5°$ and $7°$) are shown. From the condition 2.2, we can give an lower bound on the value of

λ/d for a given order m to be evanescent. In fact if

$$\frac{\lambda}{d} > \frac{2}{|m|},\tag{2.4}$$

then the diffracted order m is evanescent. This condition is sufficient but not necessary. For instance with a Ti:sapphire compressor, $\lambda/d = 1.2$. Therefore only the 1st and -1st orders could propagate. However, at least one of them is evanescent as the condition 2.2 cannot be satisfied for both orders.

An interesting configuration is such that the diffracted order (typically the -1st) back propagates in the same direction as the incident beam $\theta_m = -\theta_i = \arcsin(m\lambda/2d)$. This angle is called Littrow angle. Therefore, for the -1st order, we obtain:

$$-\theta_i = \theta_{-1} = \arcsin\left(\frac{\lambda}{2d}\right).\tag{2.5}$$

Close to this incidence, the angular deviation between the incident beam and the diffracted beam is small so it allows one to build compact systems. Furthermore, to have the highest compressor efficiencies for high power systems, the gratings are designed to only have two propagating orders: the specular which is always present, and the -1st. Using the condition 2.2 and the equation 2.5, we find that this configuration can be reached when $2/3 < \lambda/d < 2$ in Littrow configuration.

2.1.3 Grating compressor

The first diffracted order imprints an angular chirp on the beam as the wavelength depends on the angle of propagation of the beam. Using a second grating parallel to the first transforms this angular chirp into a spatial chirp: the wavelength depends on the transverse position. Finally, using a roof mirror to back reflect the beam on itself (typically at a different height) removes the spatial chirp. One can then tune the distance between the gratings to adjust the amount of negative temporal chirp added to the beam.

As explained earlier, a pulse with linear temporal chirp has its instantaneous frequency that depends linearly with time. It analogous to say that the group delay of the pulse depends linearly with the frequency. Furthermore, by writing the Taylor series of the spectral phase,

$$\phi(\omega - \omega_0) = \phi_0 + \phi_1 \cdot (\omega - \omega_0) + \frac{1}{2}\phi_2 \cdot (\omega - \omega_0)^2 + \cdots,\tag{2.6}$$

9
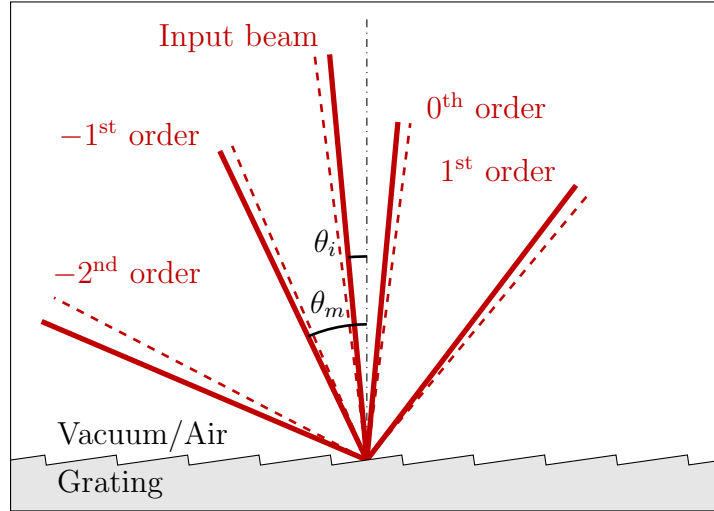
(a) Diffracted orders with $\lambda/d = 0.5$ and $\theta_i = 5°$ (solid line) or $\theta_i = 7°$ (dashed line)
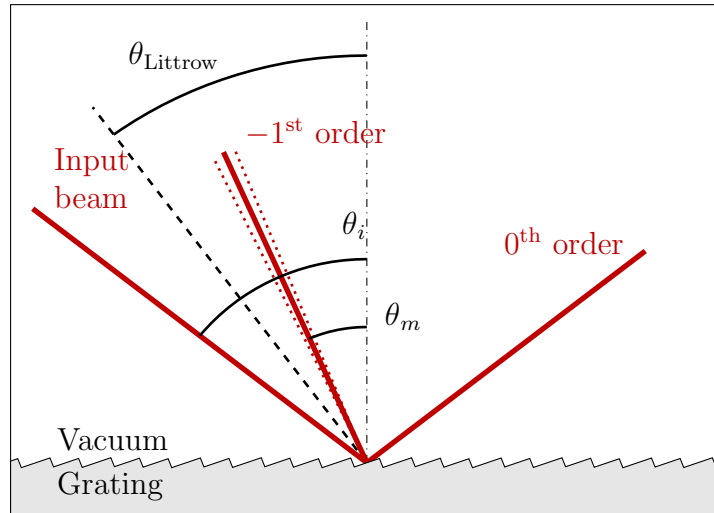
(b) Configuration of a Ti:sapphire compressor, $\lambda/d = 1.2$ and $\theta_i = 51.4°$; The dotted lines represent a 40 nm bandwidth

Figure 2.3: Schematics of the diffracted orders with different gratings and incidence angle. In (a), 3 orders are propagating due to a low groove density and thus a small diffraction power. In (b), the typical configuration for a Ti:sapphire compressor is represented. The incidence angle is 51.4° with a groove density of 1480 lines/mm. Only the -1st order propagates, and the incidence angle is larger than the Littrow angle.

with ω_0 the central angular frequency, and ϕ_n the nth derivative of the spectral phase at $\omega = \omega_0$. Therefore, as the group delay is the first derivative of the spectral phase, we obtain to the first order $t_{\text{GD}} = \phi_1 + \phi_2 \cdot (\omega - \omega_0)$. Thus, the group delay dispersion (GDD) ϕ_2 naturally characterizes the linear chirp of a pulse.

The GDD induced by a compressor composed of two parallel gratings separated by a distance L (normal to the gratings surfaces) used in double pass can be calculated according to the equation [19]:

$$\phi_2 = -\frac{\lambda_0^3 L}{\pi c^2 d^2 \cos^3(\theta_{-1})}, \tag{2.7}$$

with λ_0 the center wavelength, c the speed of light, and θ_{-1} the angle of the reflected first order calculated according to the equation 2.1. Furthermore, assuming a Gaussian temporal envelope of the pulse, the pulse duration of the chirped pulse τ_c can be calculated from the GDD and the Fourier-limited pulse duration τ_0:

$$\tau_c = \tau_0 \sqrt{1 + \left(\frac{4 \ln 2 \, \phi_2}{\tau_0^2}\right)^2}, \tag{2.8}$$

which simplifies if $\phi_2 \gg \tau_0^2$ into

$$\tau_c = \frac{4 \ln 2 \, \phi_2}{\tau_0} = \Delta\omega \, \phi_2, \tag{2.9}$$

using the Time Bandwidth Product (TBP) $\tau_0 \Delta\omega = 4 \ln 2$ for a Gaussian envelope, with $\Delta\omega$ the angular frequency bandwidth.

A typical Ti:sapphire compressor operates at an incidence angle larger than the Littrow angle (see figure 2.3b). For a wavelength of 800 nm and a grating with 1480 lines/mm, the Littrow angle is 36.3° according to equation 2.5. A usual operating incidence angle is close to 51° as it is large enough to reduce significantly the fluence ($< 65\%$ of the beam normal fluence) and provides enough dispersion in a reasonable distance to compensate for the pulse chirp [20]. This results in a diffracted angle of 23.7° (see equation 2.1). Using the equations 2.7 and 2.9, we can calculate for these parameters the separation needed to compensate a given chirp assuming a Fourier-limited pulse duration of 30 fs. We find out that τ_c [ps] $= 0.48 \cdot L$ [mm].
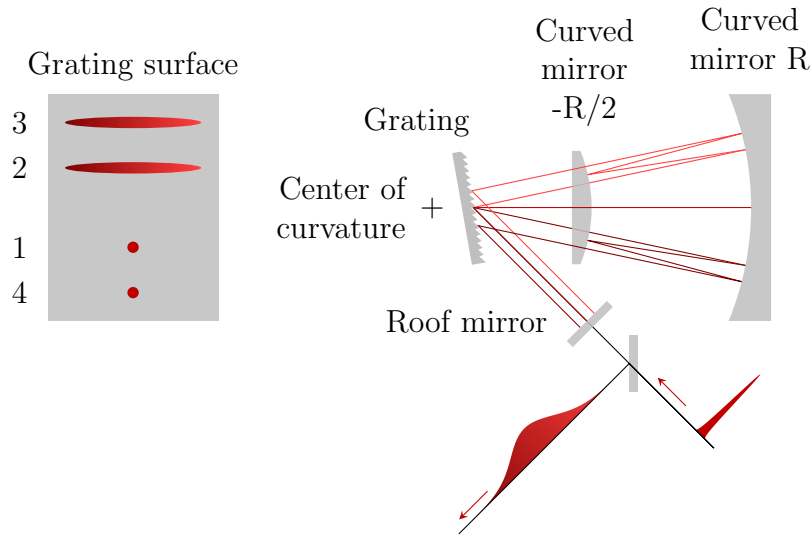
Figure 2.4: Schematic of an Öffner stretcher. The position of the four passes on the grating are indicated on the left. This configuration allows to stretch a pulse with no chromatic and little geometric aberrations. The chirp can be adjusted by changing the distance between the compressor and the center of curvature.

Concerning the stretcher, It is necessary to use curved optics in order to obtain a positive GDD. The schematic in figure 2.2 features a lens telescope for this purpose. However, for very short pulses which have a large bandwidth, transmissive optics can introduce chromatic aberrations as well as adding additional uncontrolled dispersion to the beam. Thus the telescope is usually built from reflective optics in a configuration called Öffner triplet using two concentric spherical mirror with a radius of curvature ratio of -2 (as shown in figure 2.2), a single grating used four times and a roof mirror to decouple the input and output beams [21]. The grating is placed before the center of curvature of the two mirrors to obtain a positive chirp (see figure 2.4). This configuration has the advantage of being free of chromatic and geometric aberrations (except spherical aberration as the grating is not placed at the center of curvature of the spherical mirrors, which increases the fourth order dispersion). As the beam is spatially chirped inside the stretcher, any geometric aberration would directly translate into spectral phase distortions.

2.2   Titanium-sapphire lasers

The first titanium-sapphire laser was built in 1982 by P. Moulton [15]. It was first used as a tunable CW laser thanks to its broad emission bandwidth (see figure 2.6). After the development of mode-locking [14], and especially the Kerr-lens self-mode-locking [16], it became one of the most used sources for femtosecond lasers. Most of the high energy femtosecond lasers systems are nowadays based on this technology. We review here a few properties which explain the interest of the laser community for this material. We also introduce a few concepts of general laser amplification, using Ti:sapphire as a practical example.

2.2.1   Ti:sapphire properties

A titanium-sapphire crystal ($Ti^{3+}:Al_2O_3$) contains Ti^{3+} ions ([Ar] $3d^1$) replacing the Al^{3+} ions in a sapphire (Al_2O_3) lattice. In the excited state resulting from a photon absorption, the Ti^{3+} ion displaces itself with respect to the lattice and excites vibrations which lowers the energy of the system. The coupling of electronic energy levels of the titanium ion to the vibrational energy levels of the surrounding lattice is the reason why the Ti:sapphire laser is called a vibronic laser. Once in this lower excited state, the emission of a photon brings the energy level of the system close to the ground state, which is finally reached by another fast vibrational relaxation to bring the titanium ion back to its original position in the lattice. The broadband nature of Ti:sapphire laser comes from the broadening of the ground and excited energy levels through the coupling to the vibrational levels of the lattice. Furthermore, as this relaxation is much faster (in the order of $0.1\,\mathrm{ps}$) compared to the spontaneous lifetime of the upper laser level ($3.2\,\mathrm{\mu s}$ at room temperature), the system is usually approximated as a four-level laser. Figure 2.5 shows a simplified schematic of the energy levels in a Ti:sapphire laser. For more details on the spectroscopic properties of Ti:sapphire, we refer to [22, 23].

The emission bandwidth spans from $650\,\mathrm{nm}$ to $1100\,\mathrm{nm}$ (see figure 2.6), and the bandwidth that is usually amplified through the chain goes from $750\,\mathrm{nm}$ to $850\,\mathrm{nm}$. Therefore such crystals inherently have the bandwidth necessary to support very short pulses. In fact, we can estimate the pulse duration through the Time Bandwidth Product:

$$\tau_0 = K \frac{\lambda_0^2}{\Delta\lambda \, c}, \tag{2.10}$$
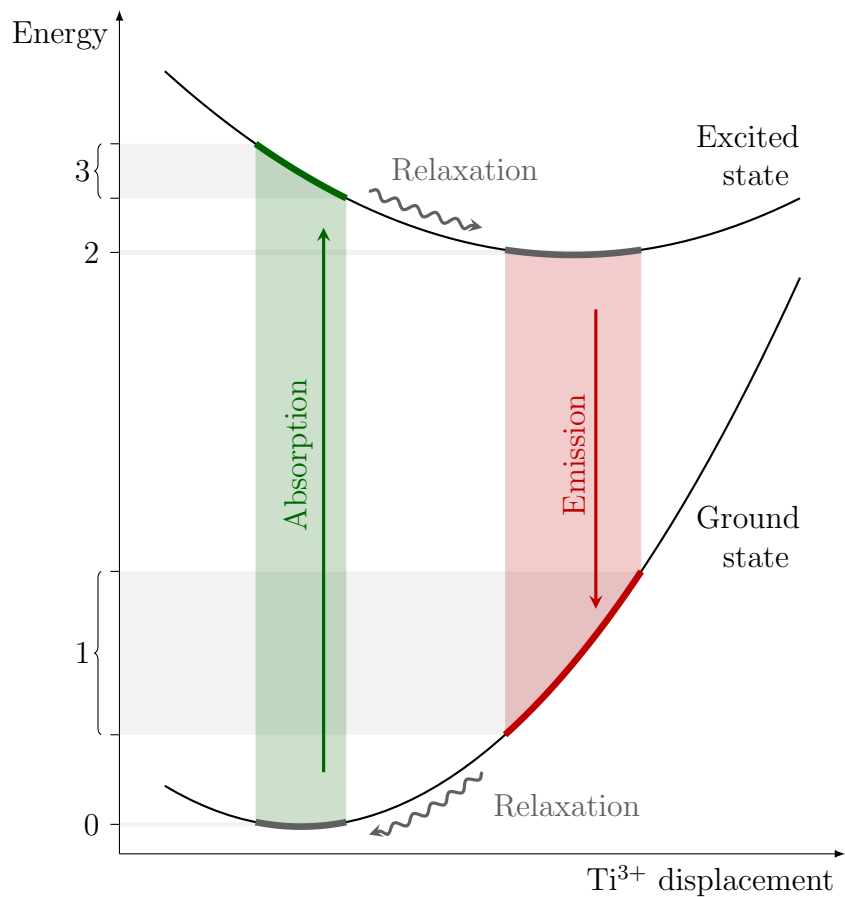
Figure 2.5: Diagram of Ti:sapphire energy levels, inspired from [22]. The absorption and emission transitions both have a large bandwidth due to the strong interaction of the electronic transitions with phonons. An electron excited in the upper level relaxes to a lower energy when the Ti^{3+} ion displaces itself and excites vibrations of the surrounding lattice. After stimulated emission, another relaxation brings the ion back to its initial position in the ground level. The relaxation time is very fast (on the order of $0.1\,ps$) compared to the upper state lifetime of $3.2\,\mu s$. The numbers on the energy scale correspond to an equivalent four-levels system for simplicity. In this approximation, the pump level (3) and lower laser level (1) have a broad energy distribution while the upper laser level (2) and the ground level (0) are sharp.

14
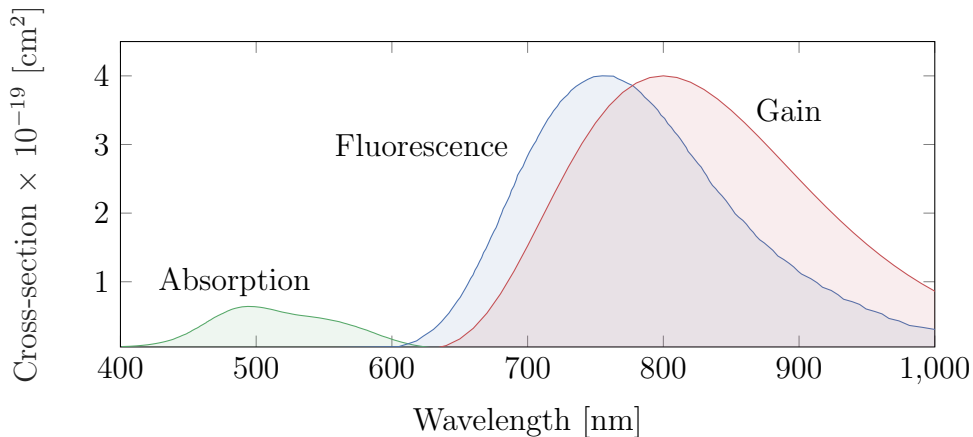
Figure 2.6: Absorption, fluorescence and gain (or emission) cross-section of Ti:sapphire for a π-polarization, reproduced from [26, 27]. The gain cross-section follows the fluorescence cross-section according to $\sigma_{\text{gain}} \propto \lambda^5 \sigma_{\text{fluorescence}}$, which explains the shift towards the longer wavelengths and the broadening of the gain cross-section.

with λ_0 the center wavelength, $\Delta\lambda$ the full width at half maximum (FWHM) bandwidth, c the speed of light, τ_0 the FWHM pulse duration, and K a coefficient which depends on the spectral envelope. For a bandwidth of 40 nm centered around 800 nm, and a assuming Gaussian envelope for simplicity ($K = 2\ln 2/\pi = 0.441$), we obtain a minimal pulse duration of 24 fs.

The absorption bandwidth is also quite broad and centered around 500 nm. Several methods can then be used to pump efficiently this crystal. Due to the short lifetime of the upper state, flash lamps are usually avoided. A common pump scheme uses a flash-pumped frequency-doubled Nd:YAG or Nd:YLF laser which lies at 532 nm or 527 nm respectively. The well-established Nd-based lasers helps to have access to commercially available high quality pumps but limits the repetition rate of high energy Ti:sapphire lasers. In fact, above 1 J output energy, the repetition rate hardly goes above 10 Hz due to the heating of the Nd:YAG rods by the unused flash lamp spectrum. However, thanks to the development of diode lasers, direct diode pumping of Ti:sapphire oscillators and amplifiers have been demonstrated [24, 25] with μJ energies at several 100 kHz repetition rates.

2.2.2 Amplifier gain

The emission cross-section σ is a key parameter to calculate the amplification of a laser beam going through a gain medium with a population inversion. For a small thickness of the crystal dz, one can write the lossless variation of the laser fluence F:

$$\frac{dF}{dz} = \sigma \Delta n \, F(z), \tag{2.11}$$

with Δn the population density difference between the two lasing energy levels. We can easily integrate this equation if the gain is small enough such that the variation of the inversion population can be ignored, meaning $dF/dz \ll h\nu \, \Delta n$ with ν the laser frequency and h the Planck constant. Using equation 2.11, we find a requirement on the laser fluence that satisfies this condition:

$$F \ll \frac{h\nu}{\sigma} = F_{\text{sat}}, \tag{2.12}$$

with F_{sat} the saturation fluence which depends only on the crystal properties. If this condition is satisfied, we then calculate the output fluence of a crystal of length L by integrating equation 2.11:

$$F_{\text{out}} = F_{\text{in}} \cdot \exp\left(\sigma \Delta n \, L\right) = F_{\text{in}} \cdot \exp\left(g_0 \, L\right), \tag{2.13}$$

with $g_0 = \sigma \Delta n$ the small signal gain. This so-called linear regime, which is only valid if the fluence is small (hence the name small signal gain), is quite interesting as one can efficiently extract energy from the gain medium in a single pass. For instance, with $g_0 \, L = 1.4$, one can increase the output energy by more than 1000 in five passes through the crystal.

On the other hand, if the fluence is high enough to extract all the energy stored in the crystal, the amplification saturates and we have:

$$F_{\text{out}} = F_{\text{in}} + h\nu \, \Delta n \, L = F_{\text{in}} + g_0 \, L \cdot F_{\text{sat}}. \tag{2.14}$$

Using the same small signal gain as before $g_0 \, L = 1.4$ with the same number of passes but an input fluence of twice the saturation fluence, the increase of the output fluence is then only by a factor of 4.5. In general, the change of the population inversion should be considered. Then, the full behavior of the amplifier is described by the Frantz-Nodvik formalism [28]:

$$\begin{aligned}
\exp(F_{\text{out}}/F_{\text{sat}}) - 1 &= \exp(g_0 \, L) \cdot \left(\exp(F_{\text{in}}/F_{\text{sat}}) - 1\right), \\
g_{\text{left}} \, L &= g_0 \, L - (F_{\text{out}} - F_{\text{in}})/F_{\text{sat}},
\end{aligned} \tag{2.15}$$

with $g_{\text{left}} L$ the gain left in the crystal after the laser has propagated through it. The two asymptotic behaviors can be retrieved from these equations using the assumptions described earlier on the input fluence. Figure 2.7 gives a representation of these two formulas.
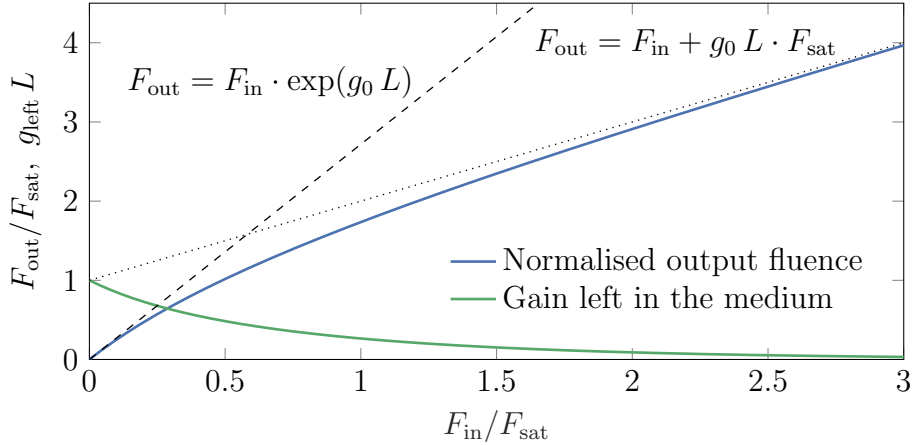
Figure 2.7: Normalized fluence and gain after one pass through a gain medium depending on the normalized input fluence with a small signal gain of $g_0 L = 1$. The output fluence can be approximated in two different regimes: the linear regime (dashed line) if $F_{\text{in}} \ll F_{\text{sat}}$ where the output fluence depends linearly on the input, and the saturated regime (dotted line) if $F_{\text{in}} \gg F_{\text{sat}}$, practically if $F_{\text{in}} \geq 2F_{\text{sat}}$. The curves are calculated according to the Frantz-Nodvik equations which describe the amplification process of a pulse propagation in a laser amplifier [28].

It is interesting for a laser crystal to have a high saturation fluence in order to operate more easily in the linear regime. However, the higher the saturation fluence the smaller the small signal gain is for a given pump fluence, so one has to find a compromise. Finally, when thinking of the last amplifiers of a high power system, a lot of energy is stored within the crystals, up to a few joules or tens of joules. It is therefore important to extract as much energy from the crystal as possible to have an efficient amplification. Moreover, as the beam size is large to stay below the damage threshold of optics, only a few passes through the crystal are possible within a reasonable footprint. Thus, the last amplifiers operate typically close to the saturation fluence in order to extract all the available gain in a few passes. This is practically possible only if the saturation fluence is below the damage threshold of the optics used. For this purpose, Ti:sapphire is especially well suited. Its saturation fluence is around $0.62\,\text{J}\,\text{cm}^{-2}$, which

means that the output fluence of the amplifiers can be close to this value as the damage threshold of high reflectivity mirrors and anti-reflective coatings at $800\,\text{nm}$ is typically around $1\,\text{J cm}^{-2}$. A second advantage of operating the last amplifiers of a high power laser system in the saturation regime is that it improves the relative energy stability as the output is no longer linearly dependent on the input.

From figure 2.7, one can see that the gain can be significantly reduced after one pass if the input fluence gets close to the saturation fluence. This effect has a strong implication for chirped pulse amplifiers. In fact, as the pulse is positively chirped in the amplifiers, the red part of the spectrum which propagates earlier sees the largest gain in the crystal while the blue part which lags behind sees an already depleted gain. Therefore, through the amplification chain the spectrum is more amplified in the red, which skews it and reduces the bandwidth. This effect enhances the gain narrowing inherent to broadband lasers. In fact, as the emission bandwidth is finite (see figure 2.6), the wavelengths close to the peak of the cross-section will be more amplified than the other wavelengths of the seed spectrum. The amplified spectrum will then be more peaked and the bandwidth reduced. For the ANGUS laser, gain narrowing and amplification of chirped spectrum have a relatively similar amplitude and both should be considered to quantify the spectral narrowing.

Figure 2.8 illustrates these two effects using ANGUS parameters. The spectrum of the multipass amplifiers is simulated with and without compensation scheme. The simulation is written in Matlab and based on the Frantz-Nodvik equations to calculate the spatial and spectral profiles through the chirped pulse amplifiers. The spectral FWHM of the fully amplified beam without compensation is then $34.4\,\text{nm}$ instead of $46.3\,\text{nm}$ using a narrowing compensation device. Such a device therefore decreases the Fourier limited pulse duration from $27.4\,\text{fs}$ to $20.4\,\text{fs}$ FWHM, which corresponds to a decrease of $26\,\%$.

The ANGUS system uses a device called Dazzler in order to compensate for the spectral narrowing. It is an acousto-optic modulator which can shape the spectral amplitude and phase of a chirped pulse [29]. Effectively, it removes a part of the spectrum around $810\,\text{nm}$ such that the spectrum is skewed towards the short wavelengths before the multipass amplifiers (see figure 2.8 middle plot). As the red part of the spectrum is more amplified, the skew will be compensated and the output spectrum will be close to a flat-top like profile with a large bandwidth.
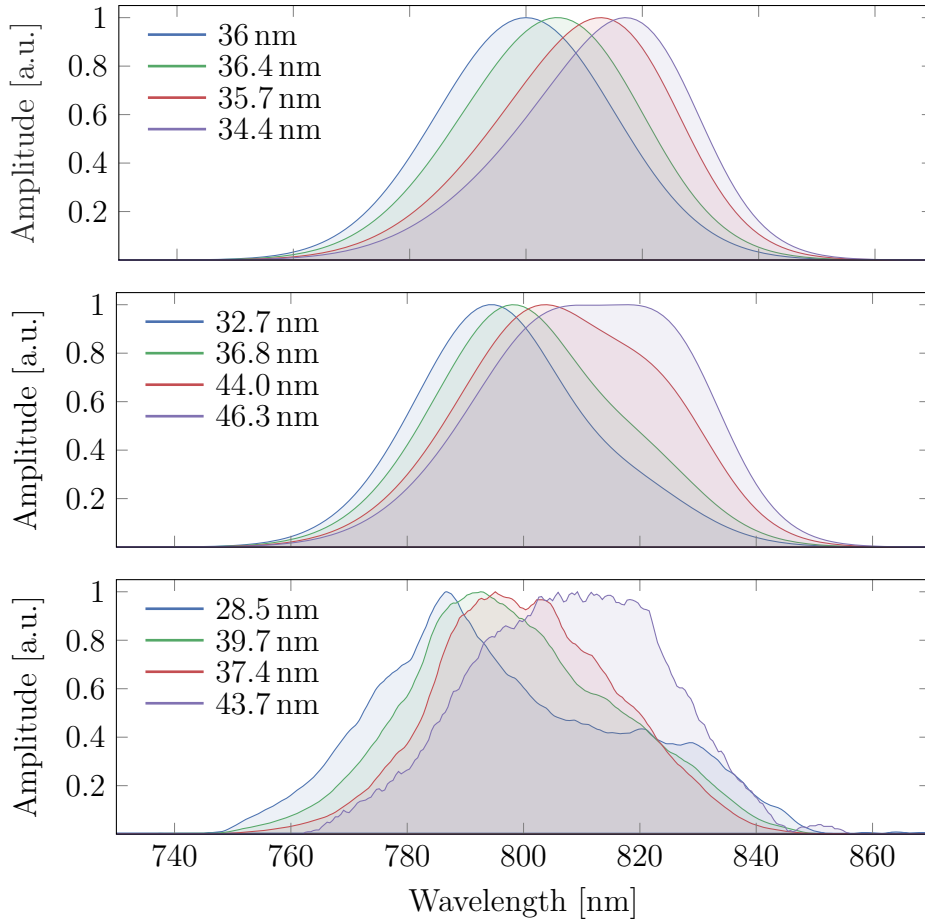
Figure 2.8: Simulation of the ANGUS laser spectrum through the last four amplifiers (blue → green → red → purple) without gain narrowing compensation (top), with compensation (middle), and the measured corresponding spectra (bottom). The FWHM bandwidth is indicated in the legend. We can see that the spectrum gets skewed towards the longer wavelengths and the FWHM decreases without compensation. By decreasing the long wavelengths part of the initial spectrum (blue, middle plot), the narrowing is pre-compensated and a much broader spectrum is obtained at the end of the amplification chain (purple). The simulations are done with a code based on the Frantz-Nodvik formalism (see equations 2.15), and using an input Gaussian spectrum.

2.3 Overview of different grating technology

This section aims to give an overview of the different techniques used to produce diffraction gratings for high-power laser systems. We first look into the processes used to manufacture the grating shape, before comparing metallic and dielectric coatings while keeping in mind that such gratings are used with broadband lasers. We also try to understand the difficulties of specifying damage threshold values. The goal is not to review in detail all aspects of this topic, for instance we do not assess volume or transmission gratings here. For such purpose we refer to appropriate handbooks and reviews such as [18, 30].

2.3.1 Grating pattern production

The two key parameters of the grating pattern are the groove density, which will define the diffracted angles based on the laser wavelength and the incidence angle as explained in section 2.1, and the groove shape which mainly defines the efficiency of the diffracted order. Typically, blazed gratings are such that the specular reflection from a single groove has the same angle as the diffracted order. Sinusoidal or trapezoidal groove shapes are also typical as they are quite easy to produce with interference lithography coupled with ion etching.

Ruled gratings

Ruled gratings are classically produced by coating the substrate with a metal, typically gold. Then, the grooves are engraved using a precision diamond tool. The shape of the grooves can be controlled by selecting the proper shape of the tool. The groove density accessible with such a technique ranges from less than 100 lines/mm up to over 10 000 lines/mm. While very versatile, this process must be extremely controlled. The diamond carriage has to follow an exact path on each pass over the grating. Any lateral displacement would change the groove spacing and thus the local diffraction process. Therefore, the lateral displacements are monitored via interferometric measurements and corrected through feedback loops. Furthermore, environment fluctuations such as air temperature and pressure also have to be extremely well controlled as they could affect this interferometric measurement and introduce errors in the process. As the grooves are ruled one at a time, the wear of the ruling tool must be measured and compensated as well, for example with an atomic force microscope.

Finally, such gratings can take several weeks to rule. For example, for a square grating of $100\,\mathrm{mm} \times 100\,\mathrm{mm}$ dimensions with $1000\,\mathrm{lines/mm}$, the diamond tool has to travel $10\,\mathrm{km}$.

Holomorphic gratings

Holographic gratings were first produced in the late 1960s [31, 32] thanks to the development of laser technology. Using the interference pattern produced by properly overlapping spatially two coherent beams (typically coming from the same laser split in two), a sinusoidal grating pattern can be recorded in a photoresist. The intermolecular bonds of such a material is altered by exposure to light. After exposure, the photoresist is chemically developed and the exposed material is removed (for a positive photoresist). The leftover material forms sinusoidal or pseudo-sinusoidal grooves which can be coated. Additionally, the grooves can be shaped using ion etching, for instance to produce a sawtooth profile to enhance the diffraction efficiency. The grooves can also be etched directly in the substrate itself to improve the robustness of the optic. The range of accessible groove densities is smaller than ruled gratings, typically above $100\,\mathrm{lines/mm}$ up to a few $1000\,\mathrm{lines/mm}$. The production time of a holographic grating is much shorter than ruled gratings as all the grooves are created simultaneously and the exposition takes less than an hour. However, the optics and laser used to produce the interference pattern have to be extremely stable, thus environment also has to be clean and well controlled. In fact, every defect, dust or scratch on the optics would create a diffraction pattern imprinted on the photoresist. Furthermore, the laser beams have to be exactly collimated as a curvature of the wavefront would result in aperiodic grooves. For the production of large gratings, the high-quality optics used to collimate the laser are usually the limitation. Scanning beam interference lithography can overcome this issue to some extent [33].

Replicated gratings

As producing a grating is expensive and time-consuming, replicas of a master grating which was manufactured following the previously described methods can also be produced. The replica substrate is coated with a layer of epoxy and pressed against the master grating. After curing and separation, the epoxy layer attached to the replica is an exact copy of the master grooves. The replica can then be coated and have the same diffraction properties as the master grating. However, the epoxy layer is typically not well suited for high power laser systems.

2.3.2 Coating

The first reflective diffraction gratings used metal layers to reflect the light due to their naturally high reflectivity for a broad range of wavelengths and acceptance angles. However, for applications with high-power lasers, the damage threshold of metal coated optics is typically lower than dielectric mirrors. Therefore, extensive research developed the field of dielectric gratings in the past 30 years in parallel to the development of said laser systems [18]. We compared here a few key features of these different coatings:

- The diffraction efficiency is a critical parameter as a typical compressor needs four passes on diffraction gratings. Therefore to obtain an overall compressor efficiency above 80 % for instance, the single grating efficiency should be close to 95 %. Furthermore, this efficiency depends on the laser polarization as first reported in 1902 [34].

- The spectral bandwidth will define whether the grating can be used for ultra-short pulses (see equation 2.10). As the pulse duration is typically in the order of tens of fs, the gratings need to reflect a bandwidth as large as 100 nm, usually centered around 800 nm for Ti:sapphire or 1053 nm for Nd:glass or Nd:YAG based lasers.

- The laser induced damage threshold (LIDT) has to be high for the grating to hold under intense incident light. The laser beam size and the incidence angle can be increased to reduce the fluence but the grating has to be large enough. Large gratings up to metre-scale can be manufactured but it is difficult to keep a high quality at the groove scale which is then 6 orders of magnitude lower than the optic dimensions [35].

Damage threshold measurement

Before looking into the different types of coatings and their properties, it seems appropriate to review the damage threshold measurement procedures. This value usually defines the laser design parameters such as beam size which has a major impact on the overall design of the rest of the facility. It is therefore crucial that the LIDT is well characterized. However, its measurement is typically a difficult task, and might not always reflect the actual operating conditions.

To reproduce the extreme conditions reached with high power systems, a small beam is usually focused on a small portion of the optic in order to

reach the same level of fluence with a more affordable laser. These tests are done either on air or in vacuum, but the influence of the environment is not clear. Some report an improvement in vacuum [36], while others see little to no effects [37]. The resulting threshold also depends on the type of exposition to the laser light. The 1-on-1 (one shot at a given fluence per location) and the S-on-1 protocols (S shots at a given fluence per location) are described by the ISO11254-1, the latter test provides insight into potential fatigue effects. The R-on-1 protocol, when the fluence is ramped up on a location until damage occurs, is also a common procedure showing some conditioning effects. However, these three techniques do not asses the overall coating quality as they are done only on a few spots. Thus, raster scanning is also a common testing procedure, which typically results in lower damage threshold, sometimes lower than 50 % compared to the 1-on-1 test for instance (see [38] for a comparison of these different techniques on multilayer coatings).

The LIDT is specified in the literature in terms of fluence in the beam normal. Therefore, the incidence angle is often specified in order to calculate the actual fluence hitting the optic. Furthermore, other parameters such as the polarization or the pulse duration need to be considered. The damage process can be completely different between a ns or a fs pulse, and depends heavily on the structure of the coating [39].

Other aspects such as the damage detection method need to be considered. In fact, is a damage considered as such when there is an actual degradation of the optic like ablation of the coating, or when the reflected laser properties are changed? Is a LIDT specified for 1000 shots still valid for 10 000 or 100 000 shots? Such questions are difficult to answer and often depend on the specific usage of said optics, whether they are used for single shot experiments or with a higher repetition rate, etc.

For this work, we will define the fluences related to damage threshold considerations in the plane of the optic used (if not specified otherwise) in order to account for the geometry of the setup. Furthermore, we consider that an optic is damaged when the properties of the laser are permanently altered afterwards. This includes for instance degradation of the beam profile due to a damage to a coating or an overall efficiency decrease.

Metallic gratings

Typical metals used for coatings are gold and silver due to their good reflectivity, typically above 95 % over a large bandwidth (from 700 nm up to

more than 3 µm) [40]. However, as silver tends to tarnish when exposed to air, gold is usually preferred. In order to help fix the gold to the substrate, an adhesion layer of chrome is sometimes additionally used [41]. It is interesting to note that for metallic gratings, both S- and P-polarization can lead to high diffracted efficiency, with very different groove profiles in each case [42]. For P-polarization (also called transverse magnetic (TM) in the literature as the magnetic field is normal to the incidence plane), shallow groove depth leads to high efficiencies, while for S-polarization (or transverse electric, TE), deeper grooves are necessary. Therefore, metallic gratings are typically used in P-polarization for high power systems as shallow grooves are easier to manufacture.

The damage threshold for single-shot femtosecond pulses is on the order of $100\,\mathrm{mJ\,cm^{-2}}$ but depends heavily on the coating shape. In fact, Poole *et al.* reports in [43] that if the coating is not flat between the ridges of the grating (for instance, if the gold accumulates more in the middle of the valley), there is a magnetic field enhancement at the bottom of the ridge on the opposite side of the incident beam. This field enhancement would increase the absorbed energy, increase the Joule heating of the grating and therefore decrease the LIDT by 15 % and the efficiency of the diffracted order by 7 %.

The presence of photoresist also affects the LIDT. For completely etched gratings, Poole obtains a value above $300\,\mathrm{mJ\,cm^{-2}}$ in the grating plane, while Neauport *et al.* [44] reports $200\,\mathrm{mJ\,cm^{-2}}$ using a more standard grating with photoresist. Furthermore, Wang *et al.* [45] shows that the gold deposition technique can decrease the LIDT by more than 25 %. Indeed, by comparing magnetron sputtering and electron beam evaporation, they observed two distinct damage morphologies. While magnetron sputtering gold deposition presents the typical damage from thermal ablation of the gold film, the e-beam evaporation deposited gold layer is peeling off from the photoresist. Their numerical simulations show that the increased Joule heating from the field enhancement induces a thermal stress concentrated on the interface of the gold layer and the photoresist, which is sufficient to overcome the adhesion strength with the latter deposition method.

Dielectric gratings

As dielectric materials feature higher damage thresholds than metals (up to a few $\mathrm{J\,cm^{-2}}$) [46], they are of particular interest for diffraction gratings. The typical geometry consists of a multilayer stack of alternating low and

high refractive index material deposited on a substrate. The grating pattern is then etched into the top layer. Contrary to metallic gratings, the diffracted efficiency is only high in S-polarization [47].

The improvement of the bandwidth and damage threshold of dielectric gratings has been growing over the last 20 years. We highlight here a few important results. Martz *et al.* [48] produced a $229\,\text{mm} \times 114\,\text{mm}$ large dielectric grating, with a diffracted efficiency above $96\,\%$ for a $40\,\text{nm}$ bandwidth centered around $800\,\text{nm}$. They measured a damage threshold of the grating of $180\,\text{mJ}\,\text{cm}^{-2}$ at $120\,\text{fs}$, which is $55\,\%$ lower than the simple dielectric stack. It is unclear if the LIDT is specified in the grating plane or in the beam normal. This grating was used to compress a Ti:sapphire pulse to the ps level. Another promising result is reported by Kong *et al.* [49]. They produced a $50\,\text{mm} \times 50\,\text{mm}$ large dielectric mirror with a reflectivity above $99\,\%$ over a bandwidth of $160\,\text{nm}$ around $800\,\text{nm}$. The damage threshold was measured to be higher than $400\,\text{mJ}\,\text{cm}^{-2}$ in the optic plane at $40\,\text{fs}$. While this optic is a mirror and not a grating, it is still an important step to improve the characteristic of multilayer coatings.

The damage processes of dielectric gratings has been studied and simulated as well [44, 50, 51]. The field enhancement at the edge of the ridge opposite from the incident light is the cause of damage in such optics. The damage threshold has been shown to scale with $1/|E|^2$, so the stronger the field enhancement (which can be as high as a factor of 2), the lower the damage threshold.

Hybrid designs

One of the inconveniences of dielectric coatings is that for a large number of layers, mechanical stress builds up between the layers which forms a weak point [52]. A way to mitigate this effect is to limit the number of stack and compensate the loss of reflectivity by placing a metallic layer between the substrate and the dielectric stacks [41]. Such coatings have a damage threshold which is between metallic and dielectric coatings, but the bandwidth is larger than just a dielectric coating. Therefore, this technique seems to be an interesting compromise between the two conventional processes described above.

2.4   On the laser wavefront

The wavefront of the laser beam corresponds to its spatial phase φ such that the spatial dependencies of electric field can be written as (assuming no spatio-temporal coupling) $E(\vec{r}) = \sqrt{I_0(\vec{r})} \cdot \exp\left(i\,\varphi(\vec{r})\right)$, with I_0 the intensity profile and $\vec{r}$ the spatial coordinates. If we have access to both the intensity and the wavefront profiles at a given position, we can reconstruct the spatial electric field and therefore reproduce numerically its evolution during propagation, especially the intensity profile of the beam through the focus. Indeed, thanks to the Huygens-Fresnel principle, we can calculate the electric field distribution in any plane from the knowledge of this field in a single source plane under some conditions on the propagation medium properties. In particular, to calculate the far field distribution, the computation simplifies into a single Fourier transform of the source plane. For further details on field propagation, we refer to [53] and references therein, which also give practical examples in MATLAB language.

In order to describe the wavefront, it is customary to use a set of orthogonal polynomials on which the wavefront can be projected. It is in fact easier to deal with a list of coefficients rather than the full 2D description of the wavefront. For circular beam, the set of Zernike polynomials [54] is especially well-suited, as explained below. For square or rectangular beams, the Legendre polynomials are preferred as the horizontal and vertical axes are decoupled.

2.4.1   Zernike polynomials

The Zernike polynomials are a set of polynomials that are orthogonal on the unit disk. They can therefore be used to describe a circular (and by extension elliptical) distribution using the coefficients of the projection of the distribution on the polynomials. Furthermore, this set is particularly suited to the description of wavefronts because the low-order polynomials are close to standard geometric aberrations, namely defocus, astigmatism, coma, spherical aberration, etc.

They are described by even and odd functions, respectively:

$$Z_n^m(\rho, \theta) = \begin{cases} \alpha(n,m) \cdot R_n^m(\rho) \cdot \cos(m\theta), & \text{if } m \geq 0, \\ \alpha(n,m) \cdot R_n^{|m|}(\rho) \cdot \sin(|m|\theta), & \text{if } m < 0, \end{cases} \qquad (2.16)$$

with ρ and θ the polar coordinates, n a positive integer is the radial order, m an integer with the same parity as n such that $-n \leq m \leq n$ is the azimuthal

order, α a normalization constant such that $\alpha(n, m) = \sqrt{n+1}$ if $m = 0$, $\sqrt{2(n+1)}$ otherwise, and R_m^n the radial polynomial defined as:

$$R_n^m(\rho) = \sum_{k=0}^{(n-m)/2} \frac{(-1)^k (n-k)!}{k! \, ((n+m)/2 - k)! \, ((n-m)/2 - k)!} \rho^{n-2k}. \qquad (2.17)$$

The two orders n and m define the "shape" of the polynomial: the azimuthal order m present in the sine and cosine functions tells how many axes of symmetry the polynomial has (2 for astigmatism, 1 for coma and so on), and the radial order n gives the maximal order of the radial polynomial function. The normalization constant α is such that each polynomial has an RMS amplitude of 1 over the unit disk.

This description seems rather complex but has a simple expression for low-order polynomials, which are useful to represent geometric aberrations as explained above. Table 2.1 gives the expression of the polynomials up to the first spherical aberration (commonly associated with spherical lenses). The sequential index given in the table is one way to map the two indices n and m to a single index (typically j). The rules are the following: j is increasing with n; at identical n, j is increasing with $|m|$; and at identical $|m|$ the positive m has a lower index than the negative. Other indexing such as defined by Noll [54] ensure that an even polynomial has an even index, or orders the polynomials with ascending $n + m$ order. Finally, the normalization constant α is sometimes ignored. Due to the diversity of the conventions, we will only use the one described by table 2.1. Figure 2.9 shows the wavefront map of these first polynomials.

Even though they are well-suited to describe low order aberrations, the Zernike polynomials have a drawback at high radial order: the oscillations described by the radial polynomials (equation 2.17) get faster and with a larger amplitude near the edge of the unit disk. For example, figure 2.10 shows a lineout of a high radial order tetrafoil 0°. One can see the increasing radial frequency close to a radius of 1. Therefore, it is difficult to decompose a wavefront with a high spatial frequency which is not at the edge of the profile with a reasonable number of polynomials.

(a) Piston

(b) Tilt 0°

(c) Tilt 90°

(d) Defocus

(e) Astigmatism 0°

(f) Astigmatism 45°

(g) Coma 0°

(h) Coma 90°

(i) Trefoil 0°

(j) Trefoil 30°

(k) First spherical aberration
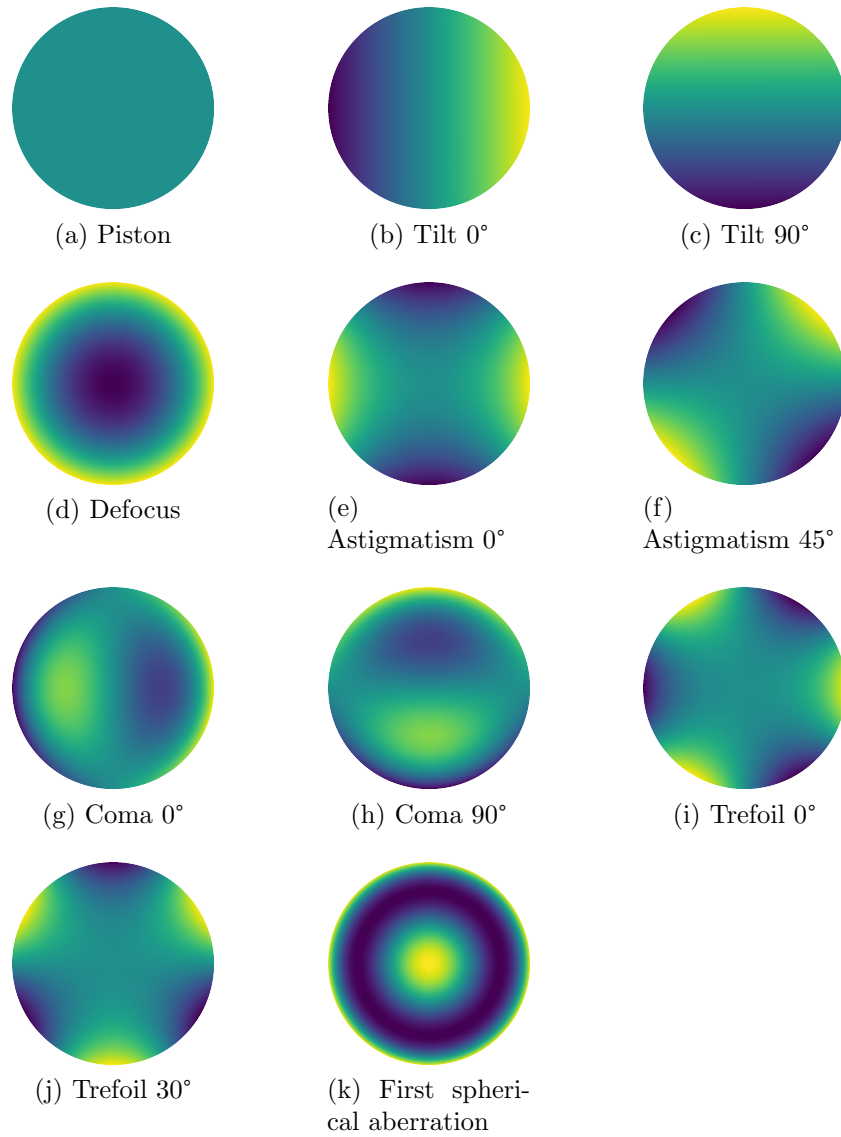
Figure 2.9: First eleven Zernike polynomials map. The first three (a-c) are not so to say optical aberrations as they do not model a curvature of the wavefront. They are nevertheless useful for completeness of the orthogonal polynomial set for the correction loop, and to measure the angular jitter.

Table 2.1: Mathematical expression of the first Zernike polynomials in polar coordinates.

Index j	Name	n	m	Expression
1	Piston	0	0	1
2	Tilt 0°	1	1	$2\rho \cos \theta$
3	Tilt 90°	1	-1	$2\rho \sin \theta$
4	Defocus	2	0	$\sqrt{3}(2\rho^2 - 1)$
5	Astigmatism 0°	2	2	$\sqrt{6}\rho^2 \cos 2\theta$
6	Astigmatism 45°	2	-2	$\sqrt{6}\rho^2 \sin 2\theta$
7	Coma 0°	3	1	$\sqrt{8}(3\rho^3 - 2\rho) \cos \theta$
8	Coma 90°	3	-1	$\sqrt{8}(3\rho^3 - 2\rho) \sin \theta$
9	Trefoil 0°	3	3	$\sqrt{8}\rho^3 \cos 3\theta$
10	Trefoil 30°	3	-3	$\sqrt{8}\rho^3 \sin 3\theta$
11	1$^{\text{st}}$ spherical aberration	4	0	$\sqrt{5}(6\rho^4 - 6\rho^2 + 1)$
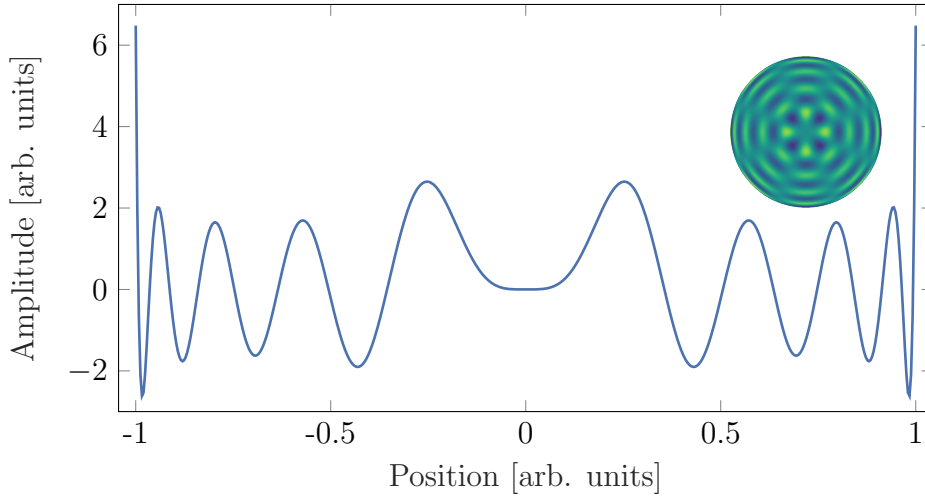
Figure 2.10: Lineout of a high radial order tetrafoil 0° (Z_{20}^4). The inset shows the complete map of the polynomial. We can see that the radial frequency increases as the position gets close to the edge of the unit disk.

2.4.2 Wavefront measurement devices

Before using the Zernike polynomials, one has to first measure the wavefront. We review in this section the two main techniques commercially used for this purpose: The Shack-Hartmann mask and the four-wave lateral shearing interferometry.

Shack-Hartmann mask
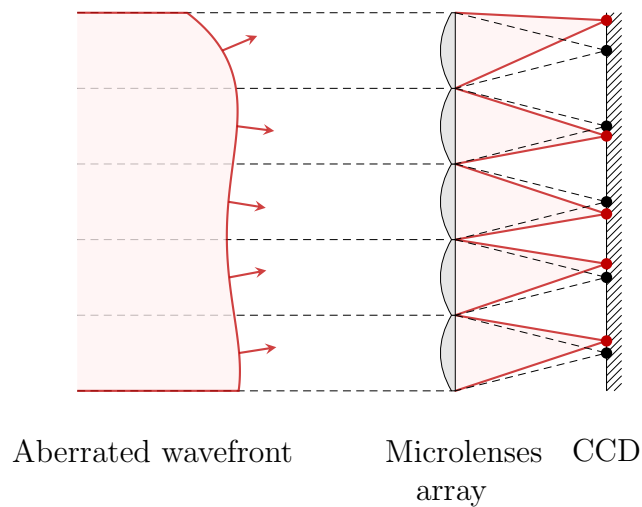
Figure 2.11: Schematic of the Shack-Hartmann principle. The red foci are displaced due to the local curvature over the area of the microlenses.

The Shack-Hartmann mask is an improvement of the Hartmann mask technique developed in 1900 for astronomical applications [55]. By using a mask with several holes in front of a telescope, one could measure the local curvature of the wavefront over the area of a hole by measuring the difference between the position of the spots on the image and the position of the holes on the mask. However, most of the signal is lost in the mask. This drawback is overcome in 1971 by Shack with the introduction of an array of microlenses instead of the mask [56]. Therefore, all the light is collected by the device and the position of the focal spot of one microlens depends on the local curvature over the area of this microlens (see figure 2.11). By placing a CCD sensor in the focal plane of the microlenses, one can record the position of the whole array and reconstruct the wavefront of the beam. This technique is now widely used and commercial products can be bought from several companies. The ANGUS lab owns such a device

from Imagine Optics[1]. However, the spatial resolution is limited by the number of microlenses covered by the laser beam. A typical microlens has a diameter of about 115 µm and the array has 30 by 40 microlenses. We note that recent work [57] proposes modifications of the device and/or focal spot detection software to measure the local tilt and curvature of the wavefront over the sub-apertures of the microlenses, which increases the largest resolvable spatial frequency.

Four-wave lateral shearing interferometer
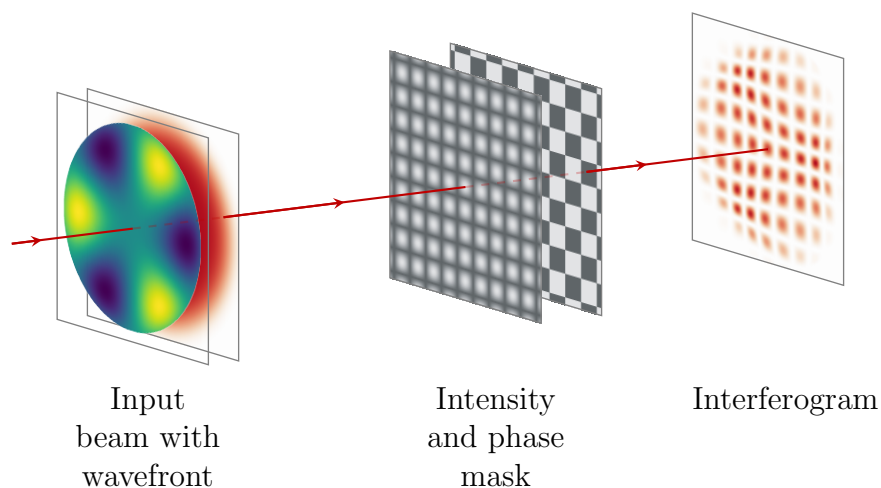
Figure 2.12: Schematic of the four-wave lateral shearing interferometer with an ideal mask. Actual devices use an approximated intensity mask, identical to a Hartmann mask.

In order to improve the spatial resolution of wavefront sensors, Primot proposed and implemented in 1993 [58] an interferometric technique using three laterally sheared replicas of the beam to form a regular hexagonal array of bright spots, similar to images produced by a (Shack-)Hartmann mask. It was later improved [59, 60] by using a bidirectional diffraction grating to generate several replicas of the beam. It consists of a intensity mask similar to a Hartmann mask and chessboard phase mask. As explained in [61], the Hartmann intensity mask can be described as a 2D diffraction grating. The generated diffracted orders then interfere to produce the intensity pattern from which the derivatives of the wavefront can be measured. By using a chessboard phase mask, and carefully designing the duty cycle of the

---

[1]www.imagine-optic.com

31

intensity mask, the 0th order can be suppressed and therefore improve the resolution of the device [62]. The commercial device from Phasics[2] uses four replicas as it proves to be more compact and simple to implement than three replicas even though there is a slight loss of transverse resolution. Such a standard device has a spatial resolution four times higher than a typical Shack-Hartmann based wavefront sensor for a similar accuracy. The LUX team at ELI-Beamlines owns such a device and was generously lent to the ANGUS lab. It has been extensively used for the work presented in this thesis.

2.4.3 Wavefront control

Once the wavefront is measured, the next natural step is to act on it and control the optical aberrations of the laser beam. It was first proposed in 1953 [63] to improve astronomical observations and especially to compensate the aberrations coming from the Earth atmosphere. It was first applied to a high power laser in 1998 [64]. From then, it became a necessary device to reach high quality focal spots by correcting the aberrations of the laser system and the transport beamline. It typically consists of a thin reflective membrane, on which several actuators are attached on the back. The actuators are pushing and pulling the membrane and therefore deforming the reflective surface. For the ANGUS lab, the membrane is a 3 mm thick fused silica plate with a high reflectivity coating and a clear aperture of 90 mm. The 52 mechanical actuators are positioned in four rings (not including the single center actuator) such that there are about nine actuators over the diameter. Having mechanical actuator instead of piezo-based actuator means that the mirror shape stays the same even when no electrical power is applied.

To operate it, the first step is to know how each actuator affects the wavefront. Therefore, they are moved independently and the relative wavefront change is measured (see figure 2.13 for an example with the ANGUS deformable mirror). Each wavefront is then decomposed on the Zernike polynomial basis to obtain a $n \times m$ matrix, n being the number of Zernike polynomials used to describe the wavefront and m the number of actuators. From this matrix, we can know the wavefront resulting from a linear combination of the actuators. We therefore need to invert this matrix to know what combination of actuator settings is necessary to obtain a given wavefront.

---

[2]www.phasicscorp.com
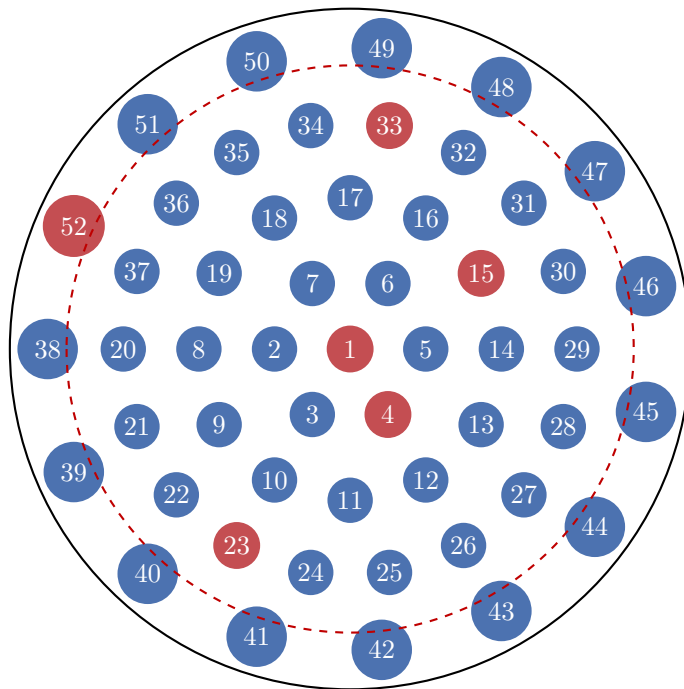
(a) Position of the actuators
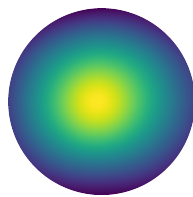
(b) Actuator 01
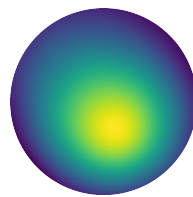
(c) Actuator 04
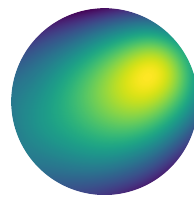
(d) Actuator 15
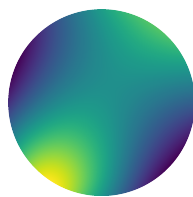
(e) Actuator 23
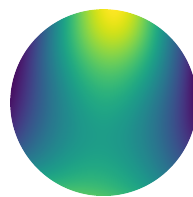
(f) Actuator 33
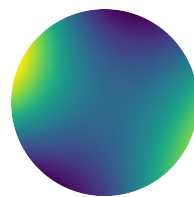
(g) Actuator 52

Figure 2.13: Actuator positions for the ANGUS deformable mirror (a). The blue and red dots show the position of the actuators over the 90 mm aperture (black line). The dashed red line shows the 75 mm typical extension of the laser FWHM. The size of the dots is only an indication and does not represent the actual size of the actuators. The wavefront response from the movement of a single actuators (red) are shown below (b-g). The outer ring of actuators induces a larger wavefront deformation (g) than the other actuators by about 50 %.

As the matrix is not square, it is not invertible (and in the case it were square, we have no knowledge *a priori* whether it is invertible or not). To circumvent this, the pseudo-inversion (or generalized inversion) can be used, which is based on the singular value decomposition (generalizing the eigenvalue decomposition).

Before actually doing the pseudo-inversion, decomposing the calibration matrix into singular values allows us to filter the "weakest" modes (smallest singular values). In fact, these modes typically correspond to very weak aberrations with high spatial frequencies. They often require strong deformations of the mirror with high order modulations which tend to increase the risk of over-correcting the wavefront. Therefore, by filtering the singular values, we restrict ourselves to a smaller range of correction but increase its efficiency and stability on this range.

Once we obtain the filtered pseudo-inverse matrix, we know the actuator settings required to obtain a specific wavefront. We can then measure the current wavefront and with the Zernike decomposition, compute the mirror shape that would generate this wavefront relative to a target wavefront (typically a flat wavefront). By subtracting this shape to the actual mirror shape we then add the opposite wavefront to the beam which results theoretically in the target wavefront. Practically, it is common to implement a safety factor in order to reduce the amplitude of the actuator movement. Therefore, several iterations are needed in order to converge to the target. However, it ensures a safer operation if the corrected wavefront starts to diverge from the target.

2.4.4   Point spread function and Strehl ratio

The measurement of a laser beam wavefront is often associated with the calculation of the point spread function and the Strehl ratio, which give an idea of the focusability of the beam. Originally defined to quantify the quality of an optical system, the point spread function (PSF) is the image of a point source through the studied optical system. The image is no longer a point due to both diffraction by the aperture of the system and by the wavefront aberrations of the optics. By comparing the peak intensity of this PSF to the peak intensity of the diffraction limited image, we obtain a simple metric for the quality of the system. This ratio is the so-called Strehl ratio and ranges from 0 to 1 for a diffraction limited image.

For laser systems, the same concept applies to quantify how close to the diffraction limit one can focus a beam. There, by measuring the wavefront

φ and the near field intensity distribution I_0, the best focal spot obtainable $I_{f,\text{best}}$ and the ideal focal spot $I_{f,\text{ideal}}$ can be calculated using a Fourier transform (which corresponds to Fraunhofer diffraction approximation):

$$I_{f,\,\text{best}} = \left| \mathcal{F} \left(\sqrt{I_0} \cdot \exp\left(i\,\varphi\right) \right) \right|^2 , \qquad (2.18)$$

$$I_{f,\,\text{ideal}} = \left| \mathcal{F} \left(\sqrt{I_0} \right) \right|^2 . \qquad (2.19)$$

The intensity distribution $I_{f,\text{best}}$ corresponds to the focus of the laser beam using an aberration-free optical system and therefore the best focus one can hope for with the measured wavefront. The ideal intensity distribution corresponds to the diffraction limited focal spot, where the optical system is perfect and the laser wavefront is flat. The ratio of the maximum intensity of these two distributions is again the Strehl ratio. It is a good indicator of the quality of the laser wavefront, and can be approximated from the RMS amplitude σ_φ by [65]:

$$S \simeq \exp\left(-\sigma_\varphi^2\right) \qquad (2.20)$$

with S the Strehl ratio and σ_φ in wavelength units. However, this approximation is mainly valid for low order aberrations such as astigmatism or coma, but fails to capture the shape and therefore the intensity of the focal spot for beams with high order wavefront aberrations. The figure 2.14 shows different Strehl ratio for a given wavefront RMS amplitude by using up to the 10th order Zernike polynomials, and one can see that this approximation typically underestimates the actual Strehl ratio.
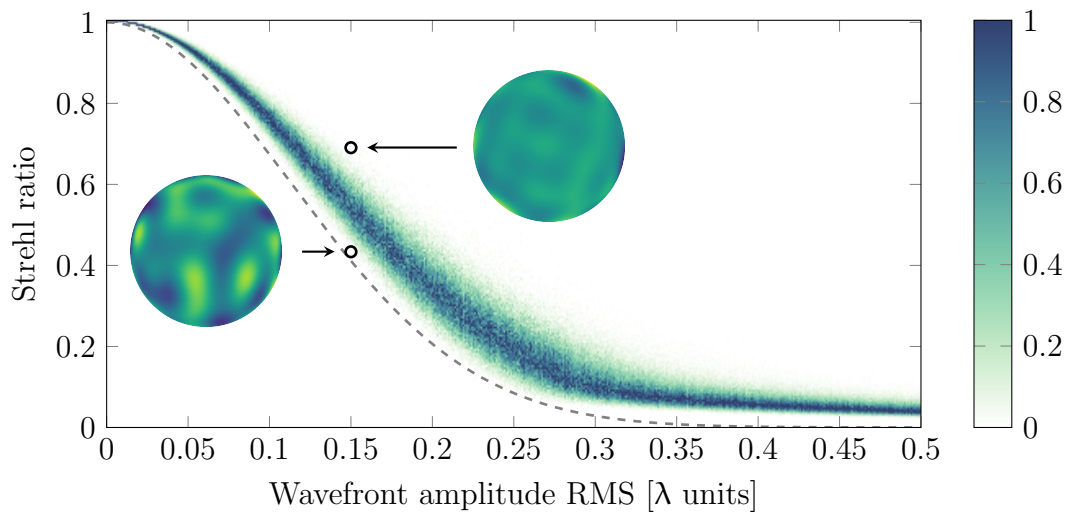
Figure 2.14: Strehl ratio in function of the wavefront RMS amplitude. For each wavefront amplitude, 1000 wavefronts are generated randomly using Zernike polynomials up to the 10th radial order n. The Strehl ratio is then calculated from the PSF. The histogram distribution is represented here for each wavefront amplitude. The approximation given by equation 2.20 is overlaid (dashed gray). For an amplitude of $0.15\,\lambda$, the wavefront maps leading to the smallest ($S = 0.43$) and the largest Strehl ratio ($S = 0.69$) are shown. One can see that the higher Strehl ratio are reached when the high amplitude modulations are constrained to the edge of the profile, while the lower Strehl ratio is due to high amplitude modulations of the center of the wavefront profile. They correspond to lower aberration orders.

Chapter 3

ANGUS system and LUX beamline

The ANGUS laser system is a titanium-sapphire based laser designed to deliver ultrashort high energy pulses reaching peak powers of 200 TW in 25 fs at repetition rate of 5 Hz. Designed and built by THALES Optronique S.A.[1], and commissioned on DESY campus in 2013, significant changes to the diagnostic and control systems have been undertaken in the following years in order to improve its stability and availability for the LUX experiment. We present here an overview of the laser system and its key parameters, followed by its integration in the control system and the advantages it provides. Finally, we quickly introduce the LUX experiment before describing the laser beam spatial diagnostics used for the rest of this work.

3.1 Overview and parameters of the ANGUS laser

The ANGUS laser is based on the CPA technique as most of high-power ultrashort laser systems. Figure 3.1 shows a diagram of its different components. The laser is seeded by a Venteon[2] oscillator pumped by a Laser Quantum[3] Finesse, which delivers a continuous 532 nm beam with 4.6 W of power. The oscillator generates a pulse train at 83 MHz with an energy of 6 nJ and a duration below 15 fs per pulse. They are then stretched to more than 100 ps in order to be amplified. The stretcher also crops the spectrum from 760 nm to 850 nm, simply by limiting the aperture of the dispersed beam. This bandwidth is more than enough to seed the following regenerative amplifier. The stretched pulses are coupled into the amplifier

---

[1] www.thales-laser.com

[2] www.venteon.com

[3] www.laserquantum.com
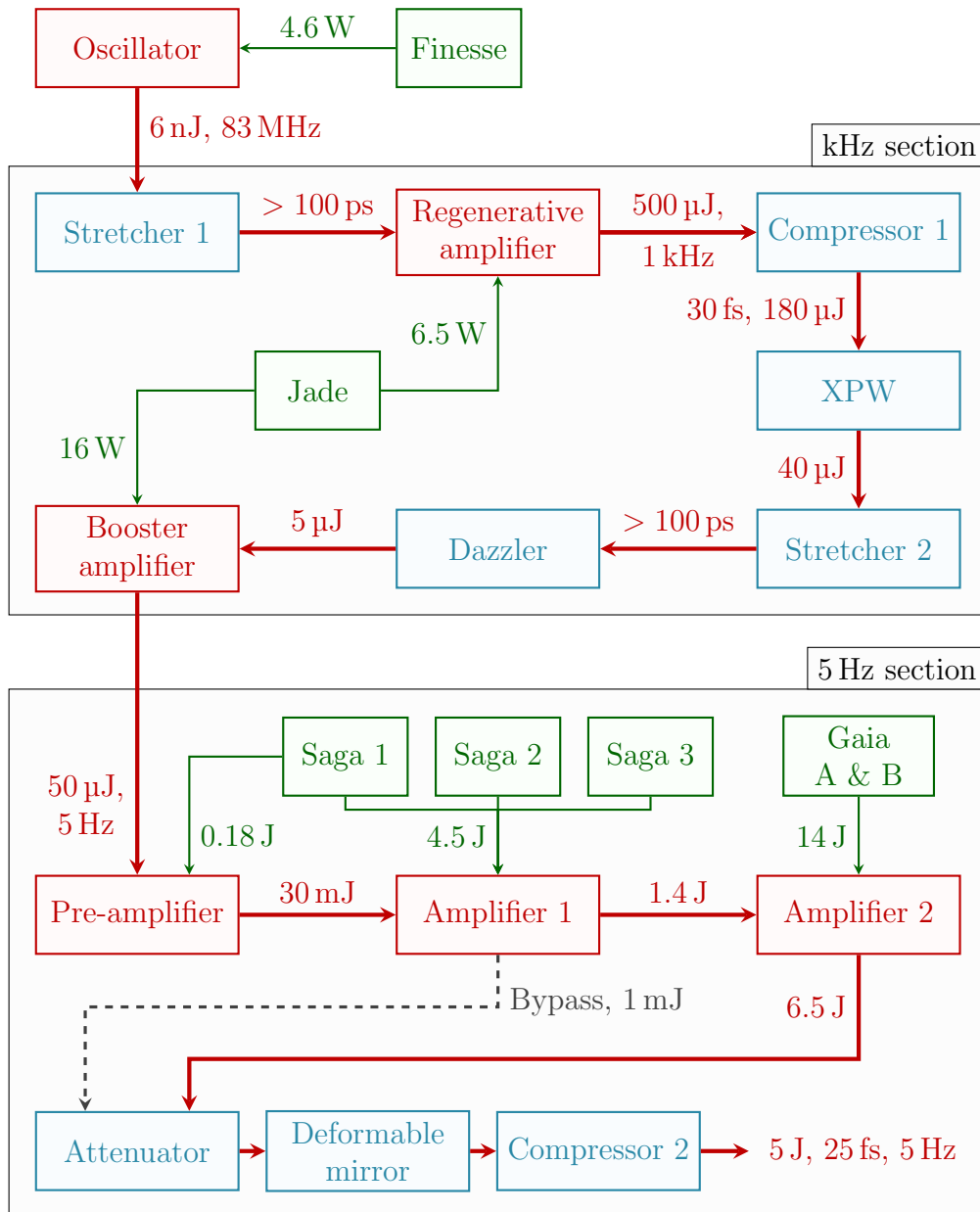
Figure 3.1: Schematic of the ANGUS system. The laser oscillator and amplifiers are indicated in red, the pump lasers in green and the pulse shaping components in blue. The characteristic parameters of the pulses are indicated between the different components

cavity via a Pockels cell at a repetition rate of 1 kHz and they are amplified in ~ 20 passes through the crystal up to 500 µJ. The crystal itself is pumped by a diode-pumped frequency doubled Nd:YLF called Jade which sends ns pulses of 6.5 mJ at 1 kHz. It corresponds to 30 % of the Jade energy, the rest is sent to the next amplifier. After the regenerative amplifier, the pulses are compressed back to 30 fs in order to improve the contrast with an XPW stage.

Indeed, while the regenerative amplifier provides a high gain in excess of 80 000, it also generates a significant amount of parasitic amplified spontaneous emission (ASE) which worsens the temporal contrast [66]. Therefore, in order to improve this contrast, the pulses are sent to a filter based on cross-polarized wave generation (XPW) [67]. This 3$^{\text{rd}}$ order nonlinear process generates a crossed polarized beam with an efficiency proportional to the incident pulse intensity. Thus, only the main pulse will efficiently generate the crossed polarization and the pre-pulses and pedestal will be greatly reduced. As the efficiency depends on the intensity, the pulses need to be compressed. The input energy is controlled by tuning the polarization by means of a half-waveplate, coupled with a polarizing beamsplitter cube, in order to generate enough output while staying below the damage threshold of the XPW crystals.

Afterwards, the now 40 µJ pulses are stretched a second time and the spectral properties are controlled with a Dazzler^4 [29], which imprints a hole in the red part of the spectrum to pre-compensate gain narrowing of the later amplifiers, and allows to finely tune the spectral phase for a compression close to the Fourier limit at the end of the amplification chain (see section 2.2.2 and figure 2.8). A two-pass Booster amplifier pumped by a 16 mJ beam coming from Jade brings the energy up to 50 µJ. Then, the repetition rate of the laser is decreased from 1 kHz to 5 Hz with a Pockels cell. In fact, as the following pump lasers are based on frequency doubled flash-pumped Nd:YAG rods, the repetition rate is limited by the heat extraction of the unused flash lamp spectrum stored in the rods. A Pre-amplifier brings the pulse energy up to 30 mJ in five passes. A fraction of a Saga pump laser is used for this purpose. The rest of this pump laser as well as two additional Sagas send about 4.5 J of pump energy into the Amplifier 1 which increases the pulse energy to 1.4 J in three passes. There, the output beam profile becomes close to a flat-top-like profile. It is common to describe such profiles as super-Gaussian, defined as

---

^{4}www.fastlite.com

$$I(r) = I_0 \exp\left[-\ln(2) \cdot \left(\frac{2\,r}{w_{\mathrm{FWHM}}}\right)^{2N}\right], \qquad (3.1)$$

with I_0 the on-axis intensity, w_{FWHM} the full width at half maximum (FWHM) and N the order of the super-Gaussian. The final amplifier stage, Amplifier 2, is also a three-pass amplifier, pumped by the 14 J of two Gaia pump lasers and brings the seed beam to its final energy of 6.5 J. It is followed by an attenuator based on a half-waveplate and thin film polarizers which can tune the energy down to 2 to 3 %. After a magnifying telescope which sets the final beam size to 75 mm FWHM, a deformable mirror (see section 2.4.3) allows to correct the wavefront RMS amplitude below $\lambda/20$ which corresponds to a Strehl ratio above 0.95. Finally, the beam is sent to the in-vacuum compressor where the bandwidth of 45 nm allows a compression down to 25 fs and the overall efficiency leads to an output pulse energy of 5 J with a relative standard deviation below 1 % over a few minutes. The pointing jitter out of the amplifier chain is below 2 μrad. The temporal contrast measured by a third order autocorrelator after full amplification and compression is $< 10^{-6}$ and $< 10^{-9}$ at 5 ps and 20 ps respectively in front of the main pulse.

Additionally, the Amplifier 2 can be bypassed and the beam attenuated in order to send 1 mJ into the compressor. Such an operation mode is set to allow work in the experimental area with a laser beam close to the design parameters in terms of pulse duration and beam profile but not intense enough to generate harmful radiation when focused. The output of Amplifier 1 can also be send to a different area of the laser lab for experiments with the joule-level chirped beam, and the output of the Pre-amplifier can be compressed with an on-air compressor to reach peak power close to 1 TW. These last two outputs are not represented in figure 3.1.

3.2   Control system

In order to ensure the good performances of the laser system and an operation close to the design parameters, several diagnostics are implemented between the different amplifiers. The output of each amplifiers is characterized by measuring the average power or the energy, the spectrum (see figure 2.8), the near field and far field profiles from which are extracted the position and pointing of the pulses. Furthermore, to prevent any damage to the amplifier crystals, the temperature of the holder is monitored to detect any over-heating, and cameras are observing the fluorescence of the

Booster, Amp. 1 and Amp. 2 to quickly identify if a damage occurs or if the pump profile is changing. The energy levels of the pumps are also measured to identify the source of an eventual change of an amplifier output parameters. All diagnostics are implemented as online measurements using the leakthroughs of mirrors, or beamsplitters.

By using the near field and far field data, coupled to motorized mirror mounts, the output position and pointing of the amplifiers are corrected for any long-term drift and fix the alignment while the laser starts and thermalization settles down. Most of the laser diagnostics can be included in the data acquisition system (DAQ) during an experiment in order to have access to the laser parameters at every amplification stage for every shot to track down the source of an eventual change. Some diagnostics like the crystals temperature are saved at a lower repetition rate. Therefore, all measurements (excluding the camera images but including the laser position and diameter) are archived at a low acquisition rate and can be called back to analyze *a posteriori* the whole status of the system.

The data measured is furthermore broadcast on the control system network and accessible live from any work station. The diagnostics of every laser sub-system are therefore constantly displayed in the laser lab, allowing the users to immediately know the status of the system while keeping it enclosed to limit perturbations of the environment and improve personal safety. The display of the laser parameters and the automatic alignment of the laser drastically reduce the necessity of any direct action by the operators and allow the system to reach full amplification in less than an hour. The full thermalization of the system typically needs another hour but no external action is required.

In order to emphasize the importance of monitoring and archiving the laser sub-systems, we report here a few studies on some key parameters.

3.2.1 Seed pointing into the multipass amplifier

To characterize the integration of the diagnostics in the control system and to identify potential troubles, the laser system was run during the summer 2015 for at least two hours every day. The resulting data set was furthermore analyzed to identify key correlations within the system. One of such correlation is related to the energy extracted from the Amplifier 1 while the pointing out of the Pre-amplifier was not yet stabilized. Therefore, the influence of the laser pointing on the amplification process could be
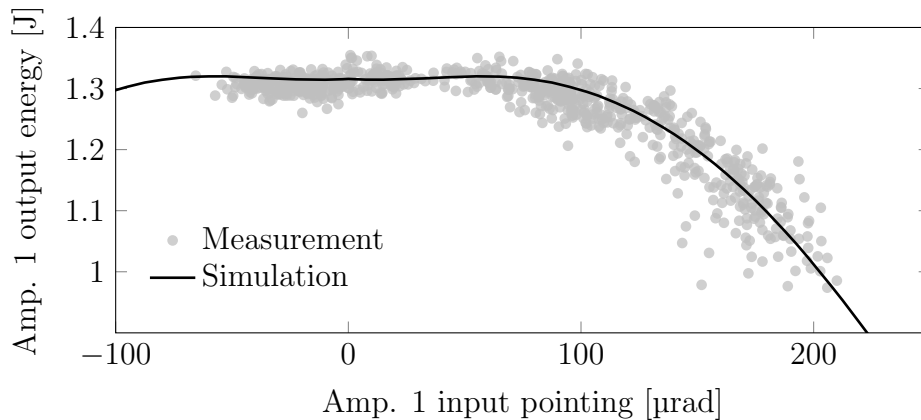
Figure 3.2: Measurement (gray dots) and simulation (solid black line) of the Amp. 1 output energy in function of the input horizontal pointing. The pointing was measured on the 04/08/2015, using the Pre-amp. far field camera. The data is scaled by the magnification of 4.2 of the telescope between the amplifiers. The simulation is done using the code mentioned in the text and shows a good agreement with the measurement.

measured.

Knowing the focal length of the lens used to produce the Pre-amp. far field, the pixel size, and considering the magnifying telescope between the two amplifiers, one can calculate from the position of the focal spot on the camera the angular pointing of the laser beam into the next amplifier. Over the day, the Amp. 1 input pointing drifted by roughly 200 µrad and the output energy decreased by more than 20 %. The figure 3.2 shows the measured output energy against the input horizontal pointing. We can observe that if the pointing stays below 100 µrad, the output energy stays constant.

Using the simulation code based on the Frantz-Nodvik equations to simulate the laser gain (see section 2.2.2), one can include a tilt of the laser beam with respect to the crystal if the system is represented in 3-D. By using the Amp. 1 parameters and setting the source of the tilt within the Pre-amplifier, we simulate the decrease of the output energy as the pointing is increased. The resulting curve is plotted on figure 3.2 and is in very good agreement with the measurement. We note from this simulation that the energy is not maximum when the beam is perfectly aligned. It is due to a simplification of the pumping profile of the crystal which is assumed to be a cylinder with a super-Gaussian profile transversely and uniform profile

42

longitudinally. Therefore, it does not account for the fact that the actual crystal is pumped by three beams which are incident with a slight angle.

This measurement helps to understand the acceptable range of the Pre-amplifier pointing, which is useful to properly set the drift compensation loop correctly. Furthermore, it helps to cross-check the accuracy of the simulation code.

3.2.2   Long-term behaviour

The slow data collector can detect if a saved variable is changing or not and automatically adjust the acquisition rate. For instance, if a measured power stays rather constant over several hours, it will not be saved for every shot. However, if there is a faster drift, it will adjust itself and save data at its fastest rate. Therefore, it limits the amount of data saved but is still able to keep track of the minute-scale variations. Using this data reduction process, the long-term laser parameters are saved and can be analyzed.

To illustrate this capability, we display on figure 3.3 the daily average power of the oscillator output since the installation of the control system in 2015. Over this time span of almost three years, about 15 million data points have been saved, which corresponds to an average acquisition rate of a data point every 9.5 minutes. It means that the oscillator fluctuations are slow enough and the data can safely be collected every 10 minutes.

One can see that the performances of the oscillator was rather good in 2016: the output power was typically well above $400\,\mathrm{mW}$, and it had to be tuned every 80 days on average. In 2015, the output power was a bit more erratic and required more tuning. It seems that the oscillator is loosing the long-term stability it had in 2016 over the past year as, again, it needs to be tuned more often. This tuning can be simply cleaning the Ti:sapphire crystal or can involve a slight realignment of the cavity itself. We also notice that since 2016, the power is decreasing on average, at a rate of $0.11\,\mathrm{mW/day}$. One has to investigate if this very slow trend can be related to a decreasing pump power for instance or just a general degradation of the oscillator itself.

3.2.3   Spectral stability over 24 hours

In November 2017, the laser and the LUX beamline (see section 3.3) have been operated for 24 consecutive hours. While it is an outstanding achievement for a laser-plasma experiment and leads to numerous analyses, we
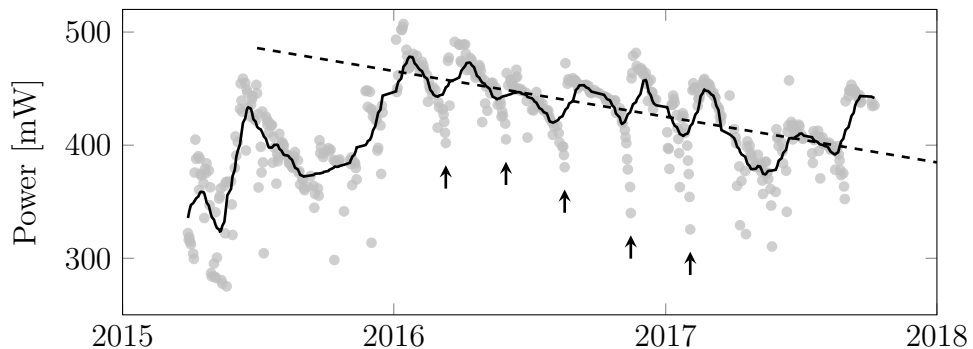
Figure 3.3: Daily average of the oscillator output power since April 2015 (gray dots). The running average over a month is overlaid (solid black line). A linear fit of the measurements since 2016 (dashed black line) shows that the oscillator output power decreases with a rate of 0.11 mW/day. The arrows indicate a few days when the oscillator was tuned to improve the performances, which was on average every 80 days in 2016. We can also notice that the oscillator was less stable in 2015 and operated at a lower output power.

focus here on the laser performances themselves and especially the fully amplified spectrum.

Figure 3.4 shows the evolution of the XPW and Amp. 2 output spectral bandwidth over the 24 hours of the experimental run. The most noticeable feature is that the spectral width decreases around midnight, at a rate of about 1 nm in 2 hours. We could observe a similar decrease of the spectral width back to the XPW output spectrum. Furthermore, we observed the presence of white light in the XPW crystal at least after 1 a.m. Indeed, as the XPW is a 3$^{\text{rd}}$ order nonlinear process, the crystals have to be operated at a high intensity in order to feature a significant efficiency. Such intensity can lead to undesirable side effects including self-phase modulation and continuum generation [68], which in turns decreases the output spectral bandwidth as the XPW efficiency is reduced.

From the change of the spectrum, we can estimate a lower limit for the change of the pulse duration, using the time bandwidth product (see equation 2.10). Over the 24 hours, the average Fourier limited temporal FWHM is (20.8 ± 0.9) fs, which corresponds to a 4 % relative standard deviation, mainly due to the drift of the spectral bandwidth in the second half of the experiment. In the first half, the relative standard deviation of the Fourier limited pulse duration is 1.5 %. As said, this uncertainty
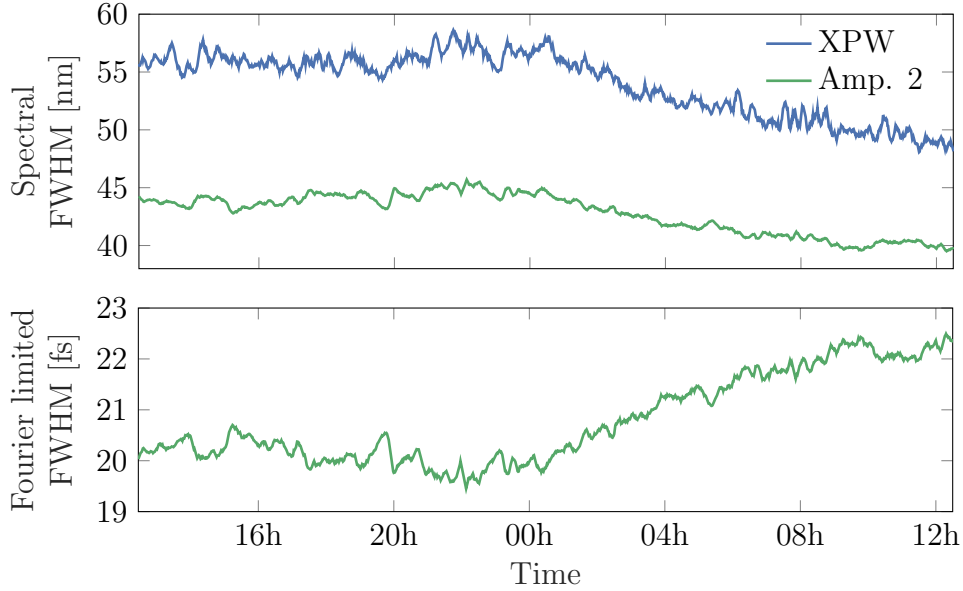
Figure 3.4: Full width at half-maximum (FWHM) of the XPW (top, blue) and Amp. 2 spectrum (top, green) during the 24 hours run (01/11/2017 – 02/11/2017). The data is averaged over 10 minutes. The bottom plot shows the width of the Fourier transform limited pulse duration for the Amp. 2 spectrum. We see that the laser bandwidth decreased around midnight. This decrease could be tracked down to the XPW.

corresponds to a lower limit based only on the spectral intensity bandwidth, and does not include the fluctuations of the spectral phase which were not measured online. In fact, according to [69], the temporal FWHM of such a laser system typically fluctuates by 5 %.

These examples show the benefits of implementing an online control system to monitor the key laser parameters. Insights can be gained on the very long term performances of the system—at the year scale—as well as over a day to identify drifts and find their origin while the output is used for experiments. It is additionally faster and easier for the operators to detect potential troubles within the system and solve them before a damage occurs. For instance, the observation of an increased temperature in the Amp. 1 crystal was later related to a blockage of the cooling circuit which could have been detrimental to the performances of the amplifier if it was not monitored. We refer to [70] for more details on this example and other case studies related to the temperature monitoring of the amplifiers crystals.

3.3   LUX beamline

While it is planned to couple the ANGUS laser to the REGAE accelerator[5] [71] in order to study external injection of laser plasma accelerators, the beam has been so far mainly used as the driver for the LUX experiment. The focus of the next chapter on the optimization of the laser wavefront and the focal spot is based on this framework. It is therefore important to understand the goals of the LUX beamline, as well as its requirements for the laser properties. After describing the goals and achieved milestones of the LUX beamline, we detail its general layout.

3.3.1   Goals and milestones

The main goal of the LUX experiment is to generate undulator-based X-ray radiation using an electron beam accelerated via laser-plasma interaction [72, 73]. In order to do so, the laser beam is focused in a gas-filled capillary target with a sub-mm diameter. The pressure within the capillary features a plateau of constant density with a length of a few millimeters which roughly corresponds to the acceleration length. Through the ponderomotive force of the laser pulse, the electrons are repelled away from the laser axis, creating a positively charged region behind the pulse. The Coulomb's force brings the electrons back on axis, which creates an oscillating electron density trailing the laser called a plasma wakefield. Within this wake, the longitudinal electric field can reach amplitudes of more than $10\,\mathrm{GV/m}$ which is several orders of magnitude higher than conventional accelerators. Electrons trapped in the high accelerating gradient region can be accelerated to more than $100\,\mathrm{MeV}$ in just a few millimeters.

Such electron beams are then steered and focused through an undulator. There, the periodic arrangement of magnets forces the beam to follow an oscillatory trajectory. The electron therefore emits radiation at every turn of the trajectory, at a wavelength defined by

$$\lambda = \frac{\lambda_u}{2\gamma^2}\left(1 + \frac{K^2}{2}\right),\tag{3.2}$$

with λ_u the period of the undulator structure, γ the Lorentz factor of the electron beam and K the undulator strength [74]. For instance with the BEAST II undulator used at LUX with a K parameter of 0.27 and a $5\,\mathrm{mm}$ period, with an electron energy of $400\,\mathrm{MeV}$ ($\gamma = 784$) one can produce

---

[5]regae.desy.de

undulator radiation at 4.2 nm which is within the water window, interesting to probe biologic samples [75].

The generation of relativistic electron beams has been demonstrated at a repetition rate of 5 Hz in June 2016 [76], the generation of undulator radiation in July 2017, water window radiation in November 2017 [77], and acceleration of electron beams up to 1 GeV in April 2018.

3.3.2 Beamline layout

After the laser compressor, the beam is transported in vacuum towards the experimental area which is represented in figure 3.5. This transport beamline is composed by ten high reflectivity mirrors. Five of them are motorized to be able to align the laser beam properly through the vacuum pipes. Then, the laser is reflected by an off-axis parabola with an offset angle of 15° and a focal length of 2.025 m, which corresponds to a F-number of roughly 25. Afterwards, two ceramic laser screens (LSD) which have a cross-shaped throughput can be inserted in order to define the laser axis. One is placed immediately after the parabola, and the second one after the focal spot and the first electron beam optics. Behind the first screen, a mirror can also be driven in the beam to deflect the laser towards the pre-target diagnostics (EVOC diagnostic) where the intensity profile through the focus, the wavefront and the pulse duration can be measured. This mirror can only be used in low power mode with a maximum pulse energy of 1 mJ. At the focal position, the target is inserted by a 5-axis manipulator. The alignment of the target on the electron axis is done automatically via a Python script, which uses the total throughput of the capillary measured on the second laser screen as a figure of merit. The target itself is a capillary milled in a sapphire plate, with an additional ceramic plate on the front to prevent laser damage. The capillary diameter is typically 300 μm to 500 μm wide with a plateau length of up to 6 mm and the gas supplied is hydrogen. A doping gas like nitrogen or argon can eventually be used to benefit from ionization injection schemes.

After the target, the electron beam co-propagates with the laser beam. As the electrons are divergent, the first element behind the target is an electromagnet quadrupole pair in order to capture and focus the beam, and a first pair of dipoles to steer it. Then, the second laser screen can be driven in as explained above, and it is followed by the laser outcoupling section. There, a holed wedge can be inserted which reflects around 1 % of the laser energy out of vacuum without disturbing the electron beam. The rest of
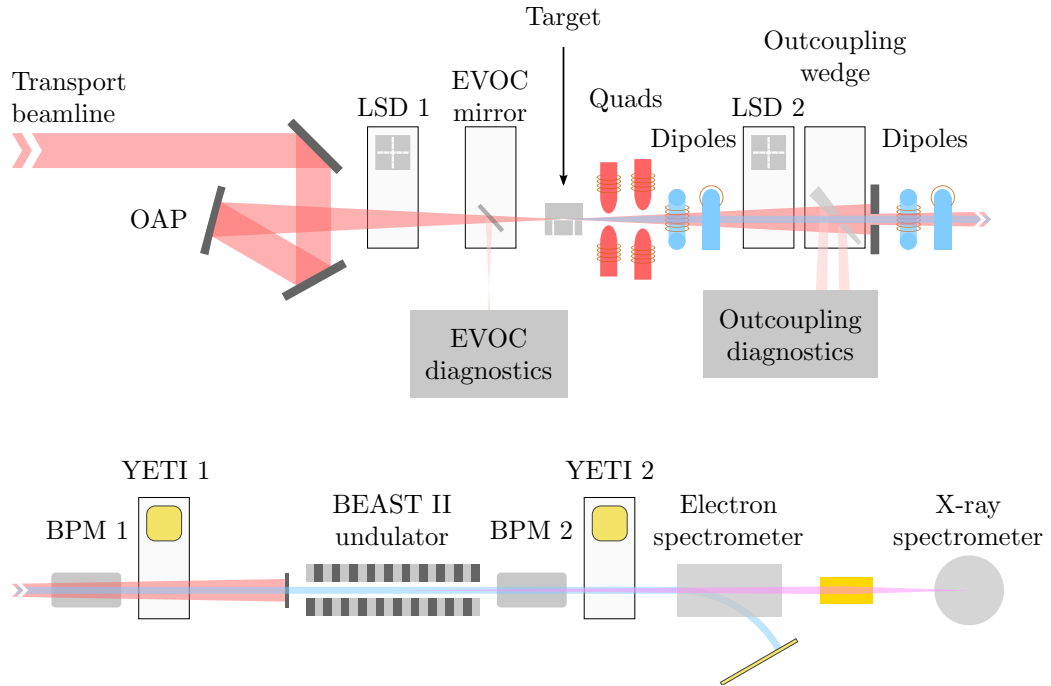
Figure 3.5: Schematic of the LUX beamline. The ANGUS laser beam is focused in the capillary target where electrons are generated and copropagate with the laser. After focusing and steering the electron beam, the laser is outcoupled for diagnostics and dumped. The on-axis laser beam is later blocked before the undulator by a thin metallic foil which lets the electron beam through with little scattering. Then, the electrons generate an X-ray beam in the undulator and are deflected by the electron spectrometer. The X-rays are focused in the X-ray spectrometer to record their spectrum. OAP, off-axis parabola; LSD, laser screen; EVOC, pre-target diagnostic section; Quads, quadrupoles; BPM, beam position monitor cavity; YETI, scintillator screen.

the laser energy is dumped in a glass plate designed to absorb the laser wavelength and attached to the flange of the chamber. After this section, the diameter of the vacuum pipe is no longer constrained by the divergence of the laser beam. A second pair of dipoles is used to adjust the electron pointing. Then the electron beam position and charge are monitored online by using a beam position monitor cavity (BPM), and a scintillator screen (YETI) positioned afterwards allows for an additional non-online position and profile measurement. They can also be used to do a quadrupole scan measurement in order to retrieve the electron beam emittance. They are followed by the BEAST II undulator chamber and another pair of BPM and scintillator screen. Afterwards, the electrons are dispersed downwards by

a permanent magnet dipole inside the electron spectrometer. The on-axis undulator radiation goes through the gap of the dipole and hits a cylindrical gold-coated mirror at grazing incidence to deflect and focus the X-rays towards the X-ray spectrometer where a transmission grating diffracts the beam to measure the spectrum.

The pre-target laser diagnostics (EVOC) has been heavily relied on for the measurements and analysis of the next chapter. Therefore, its design and implementation will be described below, as well as the other laser diagnostics available at ANGUS and LUX.

3.4   Laser beam spatial diagnostics

The accurate characterization of the laser properties is not always straight-forward. Indeed, one should keep in mind that a measurement device measures a property at the position where it is installed. Therefore, in order to gain knowledge on the direct beam itself rather than on a sampled beam, it is important to calibrate the measurement to the actual position of the laser. A calibration is however not always possible. For instance, the measurement of a near field profile using the leak through a high reflectivity mirror can be affected by the spectral transmission of the mirror coupled to the spatial dependencies of the laser spectrum. As such a diagnostic is heavily coupling several properties of both the laser beam and the optics, ensuring a calibration that stays valid over a long time and over a large parameter range is challenging. Thus, when a calibration is lacking, it is important to know how the diagnostic optics are affecting the measurement in order to provide a meaningful analysis.

As an example to this statement, figure 3.6 shows the transmission spectrum of a high reflectivity dielectric broadband mirror such as the ones used in the ANGUS laser and most of the Ti:sapphire systems. Because the reflectivity is very high (typically above 0.99), small variations of the reflectivity on the order of 0.1 % will not affect the reflected pulse significantly. However they correspond to a fluctuation of 10 % of the transmissivity which has a visible impact on the transmitted leakthrough.

To avoid using high reflectivity mirror leakthroughs, one can also sample the beam by inserting an optical element specifically for this purpose. Typically, a thin glass window is used, which can be wedged in order to avoid on-axis ghost reflections and post-pulses which can generate pre-pulses after compression [78]. However, as glass is a dispersive medium,
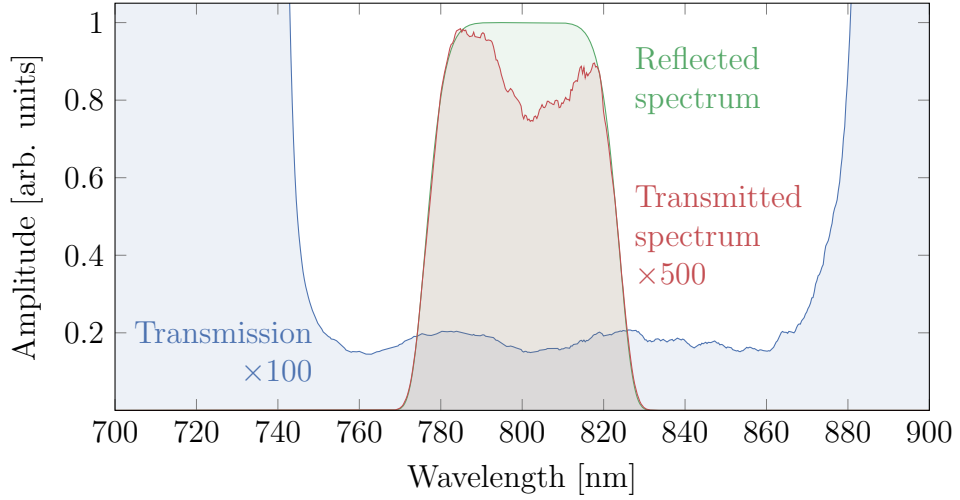
Figure 3.6: Spectral transmission of a high-reflectivity broadband dielectric mirror (blue), measured using the oscillator output beam. The effect on the spectrum of a transmitted beam (red) is simulated by assuming a flat-top-like incident spectrum with a FWHM of 46 nm (green). We see that the transmitted spectrum shows features that depend on the mirror itself (dip around 800 nm) rather than the laser spectrum.

the wedged window acts as a prism and induces an angular chirp and a pulse front tilt, which can be calculated by [79, 80]:

$$\tan \gamma = \lambda_0 \frac{d\theta}{d\lambda}, \tag{3.3}$$

with γ the angle between the pulse front tilt and the normal to the propagation direction, λ the wavelength and θ the refracted angle. Figure 3.7 represents the amount of pulse front tilt PFT $= \tan \gamma / c$ in fs/mm added to the pulse by going through a fused silica wedge at a varying incidence angle. While this amount stays acceptable with a small wedge angle (such as 0.5°, which is typical for beam samplers) at 45° and a small beam size, it can be significant for a high power laser where the beam diameter is larger than 1 cm. For instance, the Amp. 1 beam properties are sampled by such a 0.5° wedged window that adds 0.64 fs/mm, and the beam diameter is about 13 mm. Therefore, the pulse front tilt added would lengthen the pulse by $\varnothing \times$ PFT $= 13 \times 0.64 = 8.3$ fs which corresponds to 20 % of the pulse duration when the beam is loosely compressed at 40 fs. Therefore, one should be careful to not improve a diagnostic by spoiling the actual laser beam.
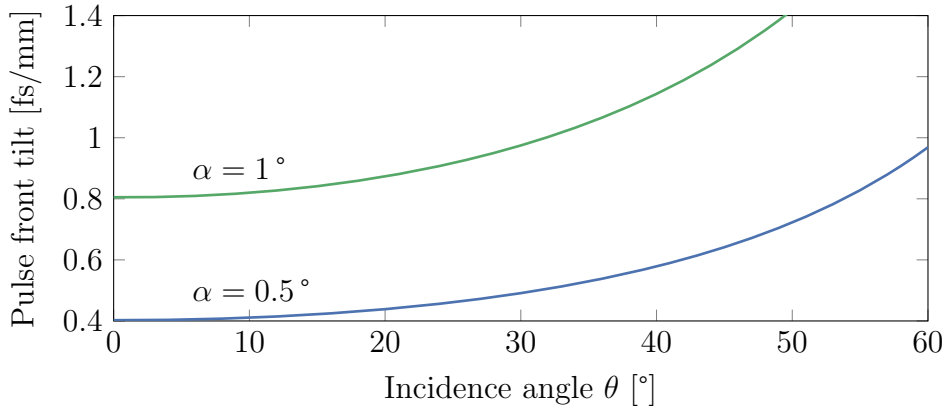
Figure 3.7: Calculation of the increase of pulse front tilt (PFT) due to the propagation of the beam through a fused silica wedge with a 0.5° (blue) or 1° (green) wedge angle α for varying incidence angle θ.

We review in this section the different laser diagnostics that have been used for this work, with a focus on the diagnostics measuring the spatial properties of the laser beam:

- The pre-compressor diagnostic which is used daily as the position and pointing reference of the laser into the compressor,

- The post-compressor diagnostic bench, delivered with the laser system in 2013 which can fully characterize the spatial and temporal properties of the beam after compression,

- The pre-target diagnostics (EVOC) which measures the beam quality through the focus,

- The post-target diagnostics which can be used online at full power to monitor changes of the laser properties after interaction with the plasma.

3.4.1 Pre-compressor diagnostics

The main purposes of the pre-compressor diagnostics are two-fold: establish a reference for the laser position and pointing into the compressor and measure the energy entering the compressor (i.e. including the attenuation). Therefore, the leak through the last mirror before the compressor is used for this purpose, in order to include as many optical components as possible. While it changes the spectrum of the sampled beam as explained before (see

figure [3.6]), the size of the optics ($100\,\mathrm{mm} \times 150\,\mathrm{mm}$), the space available and the constraint that it should be placed as late in the chain as possible forces us to use this sampling method.
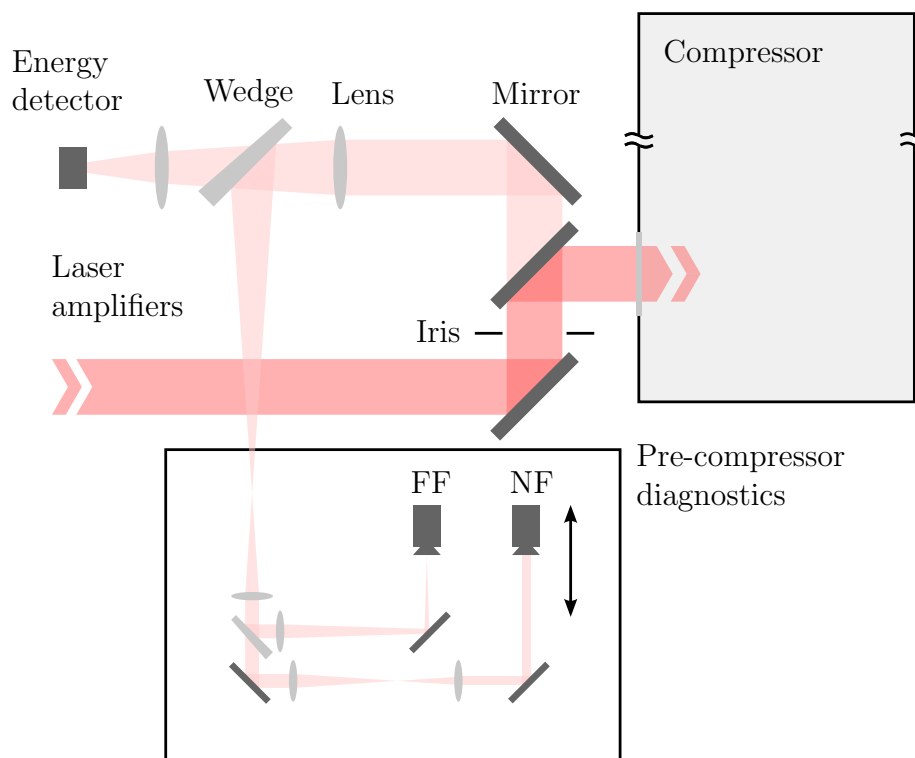
Figure 3.8: Schematic of the pre-compressor diagnostics. This setup is used in everyday operation to monitor online the compressor input pointing and position, and the energy, but it can also be used to virtually image the near field profile in the transport beamline, or monitor the wavefront. FF, far field camera; NF, near field camera.

The reference for the near field position is the iris positioned right before the last mirror (see figure 3.8) and the far field is defined such that the beam is centered for the four passes on the gratings and on the first motorized mirror in the transport beamline. The corresponding beam position and pointing on the near field—which images the plane of the iris— and far field cameras are then recorded and used during daily operation to ensure the proper alignment of the laser into the compressor and the transport beamline.

The two telescopes are designed such that the beam is demagnified by a factor $1/M = 30$ and that the near field camera can image a broad
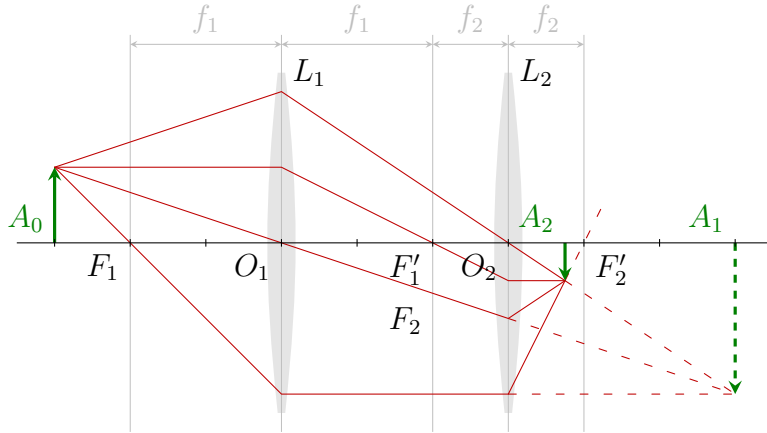
Figure 3.9: Imaging for an afocal telescope with a magnification of 2/3. The image A_1 from the 1$^{\text{st}}$ lens and the dashed rays are virtual. This ray construction allows to geometrically calculate the position of an image through an optical setup.

range of object planes which covers the deformable mirror and the off-axis parabola virtual plane (see figure 3.10). This magnification factor is chosen in order to fill a reasonable amount of the standard ANGUS CCD cameras[6] which have a sensor size of $4.9\,\text{mm} \times 3.6\,\text{mm}$ corresponding to a resolution of $0.11\,\text{mm/pixel}$. Then, a $80\,\text{mm}$ diameter beam demagnified to $2.67\,\text{mm}$ would fill $74\,\%$ of the image height, which leaves some margin for misalignment. Furthermore, as the beam is demagnified, the imaging is contracting the distances by $1/M^2 = 900$. Thus, the camera only needs to travel $50\,\text{mm}$ to cover the 40 to $45\,\text{m}$ necessary to image the whole transport beamline, which is well within the range of standard linear translation stages.

Using the Newtonian form of the thin lens formula, we can calculate the position of the image plane formed by an afocal telescope. For one lens L_1 placed at O_1, the image of the object at A_0 is positioned at A_1 defined by:

$$F_1'A_1 \cdot F_1A_0 = -f_1^2, \tag{3.4}$$

with $F_1'A_1$ the distance from the image focal plane to the image position, F_1A_0 the distance from the object focal plane to the object plane, and f_1 the focal length of the lens. The distances are signed such that $AB = -BA$ and positive distances are in the direction of the laser propagation. For

---

[6]Basler acA1300-30gm, www.baslerweb.com

53

an optical system with several lenses, the image position given by the first lens defines the object plane of the second lens, and so on. In particular for a two-lens afocal telescope such that the image focal plane of the first lens coincide with the object focal plane of the second lens ($F_1' = F_2$), the position of the image plane from the 2$^{\text{nd}}$ lens $O_2 A_2$ is found to be

$$O_2 A_2 = M \left(f_1 + f_2 \right) - M^2 \cdot A_0 O_1, \tag{3.5}$$

with $M = f_2/f_1$ the telescope magnification. Figure 3.9 shows the ray construction of such a telescope with a magnification of $2/3$ using the same naming convention, which can be used to geometrically calculate the image position. Practically, it is easier to measure distances from the center of the lenses.

For two consecutive afocal telescopes as used at the pre-compressor diagnostics, we can calculate the position of the image by using equation 3.5 twice:

$$O_4 A_4 = \left[M_2 \left(f_3 + f_4 \right) + \left(M_2 \right)^2 \cdot \left(M_1 \left(f_1 + f_2 \right) - O_2 O_3 \right) \right] - \left(M_2 M_1 \right)^2 A_0 O_1, \tag{3.6}$$

with f_i the focal lens of the i$^{\text{th}}$ lens, $M_1 = f_2/f_1$ and $M_2 = f_4/f_3$ the magnifications of the two telescopes, and $O_2 O_3$ the distance between the two telescopes, i.e. between the 2$^{\text{nd}}$ and 3$^{\text{rd}}$ lens. One only need to ensure that the imaged planes are not virtual or too close to the optics—as it would be for a single telescope in this specific case—by adjusting the distance $O_2 O_3$ for $O_4 A_4$ to be positive.

Moreover, a beamsplitter can be inserted after the telescopes to send the beam to a wavefront sensor (not shown in figure 3.8) which images the deformable mirror plane and can thus be used to optimize the wavefront.

Between the two telescopes, a thin 0.5° wedged AR coated beamsplitter sends less than 1 % of the beam towards the far field diagnostic. There, a 300 mm lens focuses the beam onto a CCD camera mounted with a ×10 microscope objective which leads to an angular resolution of 62.5 nrad/pixel for the beam into the compressor.

The energy is measured using the leak through the very first wedge of the diagnostic optics. This measurement is heavily correlated to the actual spectrum, as shown in figure 3.11. However, the fluctuations due to the spectral changes stays in the few percents level. Therefore, larger changes of the energy can be monitored to identify trends, but the absolute energy cannot be retrieved from this setup.
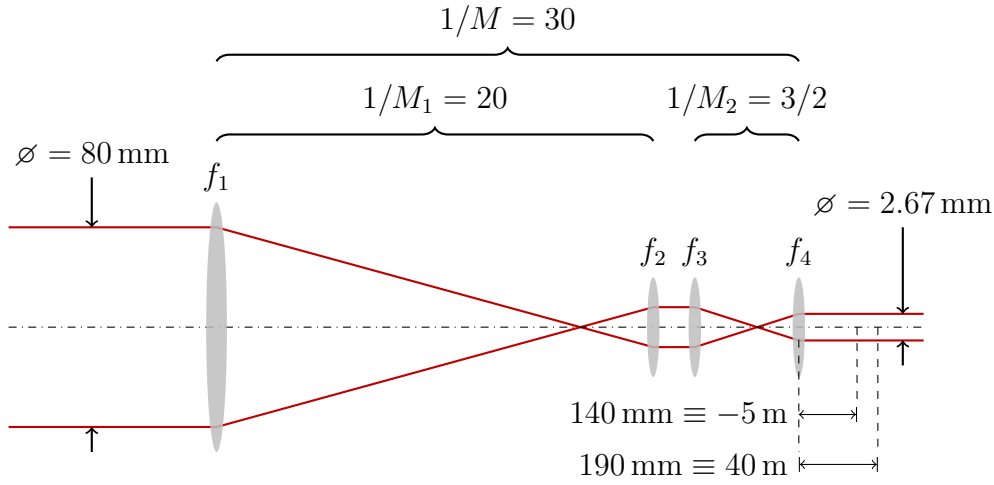
Figure 3.10: Optical layout of the pre-compressor diagnostics imaging telescopes. The first telescope ($f_1 = 1000$ mm and $f_2 = 50$ mm) does most of the demagnification and the main purpose of the second telescope ($f_3 = 150$ mm and $f_4 = 100$ mm) is to relay image the relevant image planes to a reasonable distance from the last lens. The object plane positions (indicated in meters) are referenced from the first lens, and positive distances correspond to virtual object planes.
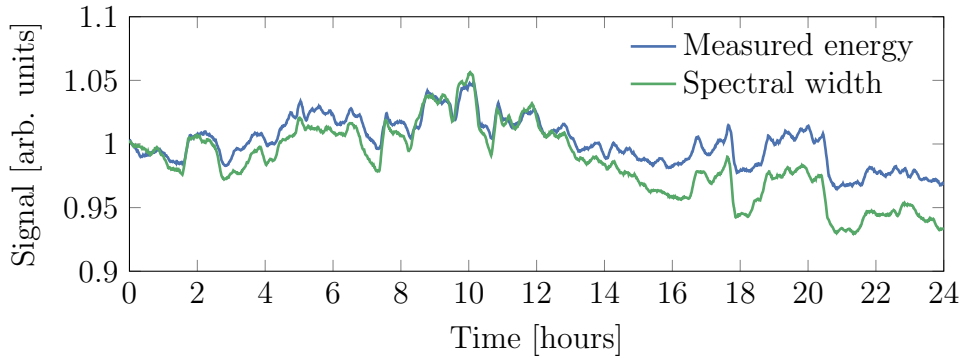
Figure 3.11: Comparison between the energy measured at the pre-compressor diagnostics (blue) and the spectral width (green) of the pulses during the 24 hours experiment averaged over 10 minutes. The spectral width is a reproduction of figure 3.4. There is clear correlation between the two measurements, which is due to the spectral transmission of the high reflectivity mirror as shown in figure 3.6. In fact, the energy of the beam was directly measured before and after the run at respectively 2.47 J and 2.48 J, so we can assume that the energy did not change significantly during the run.

3.4.2 Post-compressor diagnostics

After the compressor, the beam is sampled again using the leak through a mirror within the compressor vacuum chamber, as shown in figure 3.12. This leak is sent through a window on air and demagnified by 20 using two spherical mirrors. As the pulse compression can be measured here, it is important to limit the amount of material the pulse has to propagate through. Indeed, as explained in section 2.1, propagation through material introduces dispersion which stretches slightly the beam. Therefore the measured pulse duration would not correspond to the in-vacuum pulse duration. This effect happens already as the beam has to go through the vacuum window in order to be diagnosed on air, but additional dispersion should be kept to a minimum. It explains why the demagnifying telescope is an all-reflective design.

However, the mirrors used are spherical, and mounted in an off-axis configuration. Therefore, it adds $0.09\,\lambda$ of astigmatism and $0.03\,\lambda$ of coma to the laser beam, which amount to a total added wavefront aberration of $0.1\,\lambda$ RMS and $0.5\,\lambda$ peak-to-valley (PTV). Such a wavefront leads to a point spread function (PSF) with a Strehl ratio of 0.7. Cylindrical lenses are placed in the beam path to compensate the astigmatism for the spatial diagnostics but any absolute measurement from the wavefront sensor or the far field camera should not be fully relied on. Spherical lenses are focusing the beam for the far field camera, and imaging the entrance of the diagnostic setup for the near field camera and the deformable mirror plane for the wavefront sensor.

The temporal diagnostic of the beam is done thanks to several devices. The temporal profile and phase can be retrieved by either a Wizzler[7] [81] or a Grenouille[8] [82]. The Wizzler has the advantage of being able to feedback the measurement to the Dazzler and therefore actively correct the spectral phase to obtain an ideal compression, akin to the wavefront correction using a deformable mirror. Additionally, a 2nd order autocorrelator is available. As its software is not proprietary, it is integrated in the control system of the laser and can be included in the DAQ for an online pulse length measurement. Finally, a scanning 3rd order autocorrelator can measure the temporal contrast. The spectrum and the energy can also be measured at the post-compressor diagnostics. However, the spectrum can be modified compared to the laser beam due to the spectral transmission of the high reflectivity mirror as already reported by figure 3.6.

---

[7] relying on Self-Referenced Spectral Interferometry (SRSI), www.fastlite.com
[8] relying on Frequency-Resolved Optical Gating (FROG), www.swampoptics.com
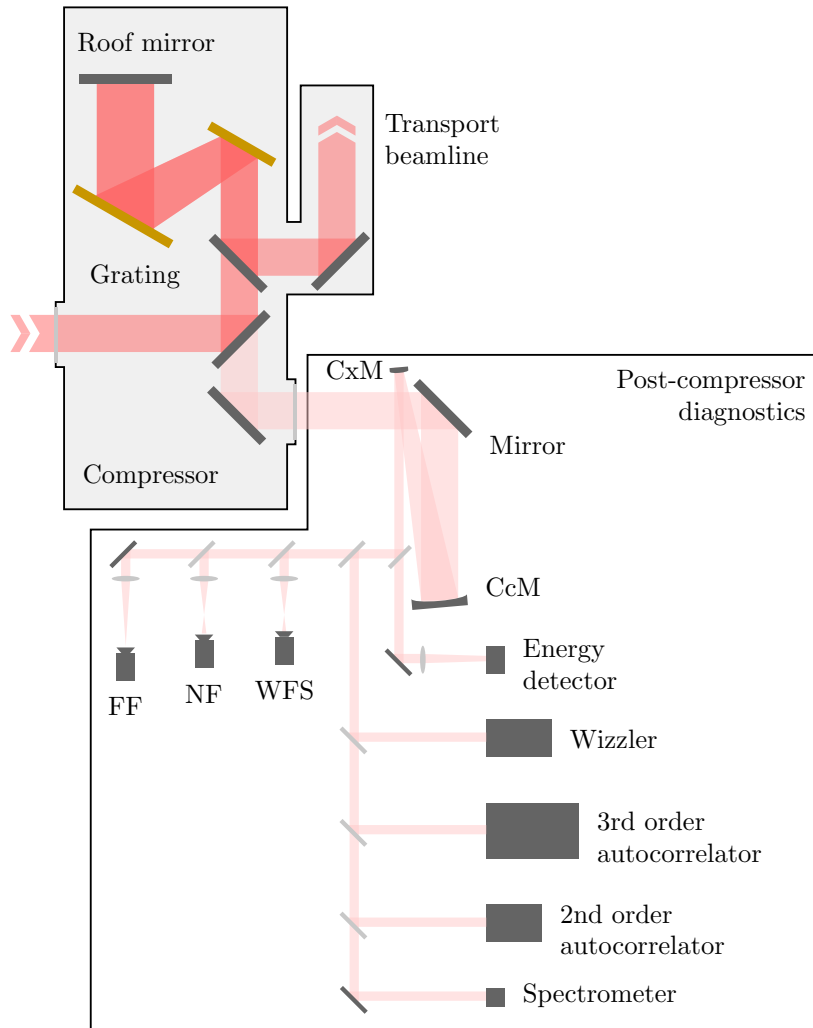
Figure 3.12: Schematic of the compressor and the post-compressor diagnostics. The leak from the in-vacuum mirror placed after the last pass on the gratings is sent on air and demagnified using two spherical mirrors. The beam is then split several times using beamsplitters, which are set in order to limit the amount of material the pulse has to go through before the temporal shape is retrieved. FF, far field; NF, near field; CxM, convex mirror; CcM, concave mirror.

3.4.3 Pre-target diagnostics

In order to monitor the beam properties as close to the target as possible, the last vacuum chamber before the target features a mirror mounted on a translation stage (see figure 3.13). It can be inserted in the low-power beam, which has an energy of 1 mJ. It corresponds to either the "bypass mode" when the Amp. 1 beam is attenuated and Amp. 2 is bypassed, or the "full-attenuation mode" when the laser is fully amplified and attenuated to 1 mJ before the compressor. With this operation mode, the laser has all the properties of the full power beam (i.e. the thermal lensing coming from the last amplifier is included, the beam size is the same, etc.) except the energy. It allows the pre-target diagnostics to be used and the laser to be aligned in the beamline before the experiment.

With 1 mJ, the B-integral of the laser going through the window is below 0.3. It represents the nonlinear phase shift accumulated by the pulse when passing through material and should typically stay below the unity to avoid changing the temporal properties of the laser. It is defined as:

$$B = \frac{2\pi}{\lambda} \int n_2 I(z) dz, \tag{3.7}$$

with λ the wavelength, n_2 the nonlinear index of refraction and $I(z)$ the peak intensity of the beam through the material, z being the propagation direction. Therefore, the pulse profile should be close to the in-vacuum profile, after accounting for the chromatic dispersion of the window and the lenses, which increases the GDD by about $500 \, \mathrm{fs}^2$.

After being outcoupled from the vacuum, the beam is collimated by a $f = 300 \, \mathrm{mm}$ lens, and refocused by an identical lens onto a CCD camera to measure the in-focus intensity profile. Furthermore, the camera is mounted on a translation stage and can be remotely controlled to perform an automatic z-scan measurement. Figure 3.14 shows an example of such a measurement. From the images, one can calculate the RMS radius of the beam (also called D4σ), which is the square root of the second centered moment of the intensity distribution, $w_x^2 \propto \iint (x - x_0)^2 \, I(x, y) \, dx \, dy$ for the horizontal plane. From its evolution through the focus, we can calculate the beam propagation factor M^2 such that [83]:

$$w^2(z) = w_0^2 + M^4 \left(\frac{\lambda}{\pi w_0} \right)^2 (z - z_0)^2, \tag{3.8}$$
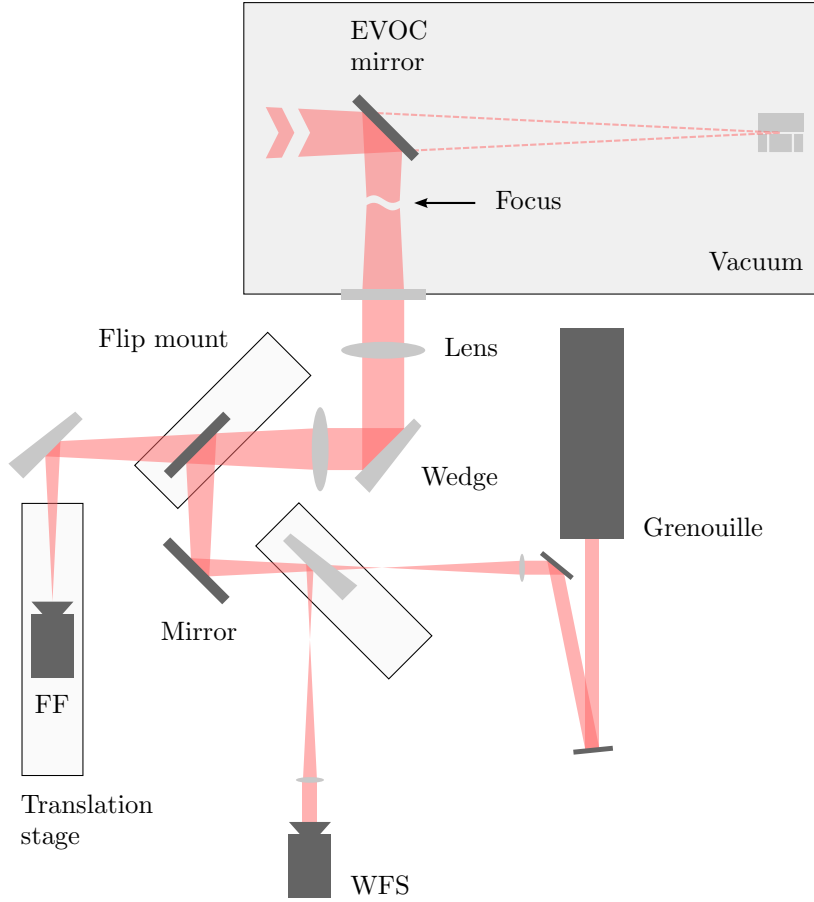
Figure 3.13: Schematic of the pre-target diagnostics (EVOC). The low-power beam (1 mJ) can be deflected out of vacuum before the target to be diagnosed. The focal spot is in vacuum and the beam is divergent through the window before being collimated, attenuated and re-imaged to be diagnosed. FF, far field camera; WFS, wavefront sensor.

with w_0 the beam waist and z_0 its longitudinal position. From this relation, we can calculate the Rayleigh length z_R, defined as the distance from the waist position where the intensity doubles. We obtain:

$$z_R = \frac{\pi w_0^2}{M^2 \lambda}. \tag{3.9}$$

We note that when $M^2 = 1$, we end up with the usual definitions of the waist and the Rayleigh length for a Gaussian beam as expected. Usual values of the M-squared and the Rayleigh length for the ANGUS beam are indicated in figure 3.14. We also remark on this figure that the FWHM stays rather constant over the Rayleigh length, which is typical of flat-top-like profiles.

Out of this range, the signal-to-noise ratio of the camera image decreases and therefore, the FWHM calculations fails to accurately reproduce the expected behavior (which explains the spikes below $-6\,$mm in the top plot). Moreover, as usual when calculating moments from measurements, one should be careful about the background and the noise level which artificially increase the measured beam radius and the resulting calculations. Therefore, the measurements presented here have been processed using an adaptive Wiener noise-removal filter [84]. The good agreement between the fit and the measured data at high and low signal-to-noise ratio is a good indicator that the filter does not modify significantly the relevant data and thus allows us to retrieve accurately the beam radius.

Apart from sending the beam to the far field camera, two optics can be flipped into the beam path to deflect the laser towards either a wavefront sensor or a Grenouille to measure the pulse duration. The wavefront sensor is placed in the image plane of the deformable mirror (thanks to the 2$^{\text{nd}}$ collimating lens with a focal length of $f = 100\,$mm) and is used before every experiment to ensure the quality of the focal spot.

It is critical that the measured wavefront is an accurate representation of the in-vacuum focal spot. The wavefront was then measured both right after the vacuum window in the divergent beam and at the usual wavefront sensor position with a 15 minutes interval between the two measurements in order to calibrate the quality of the optics. However, as the beam is too large to be entirely measured by the wavefront sensor at the entrance of the diagnostics setup, only the center part of the laser wavefront could be retrieved. It corresponds to a radius of $30\,$mm for the full scale beam. Nevertheless, the wavefront difference (shown in figure 3.15) has an amplitude as low as $\lambda/50$ RMS and 0.14λ PTV, which is in the order of the optical quality of the optics used. To assess the error due to the limited aperture of the measurement, the full aperture and the limited aperture wavefronts are compared using the EVOC wavefront sensor. The comparison shows that the most prominent modes (which are astigmatism, trefoil and coma) are identical and the amplitude of the full aperture wavefront is in slight excess of twice the amplitude of the limited aperture wavefront. However, the assumption that the amplitude doubles when comparing the reduced aperture and the full aperture is only valid if the wavefront does not contain high order modes. As represented in figure 2.10, their high frequency oscillations have a rather constant amplitude over most of the aperture and therefore do not drastically increase the RMS amplitude. For the wavefront difference measured here, we cannot affirm that no high order mode would
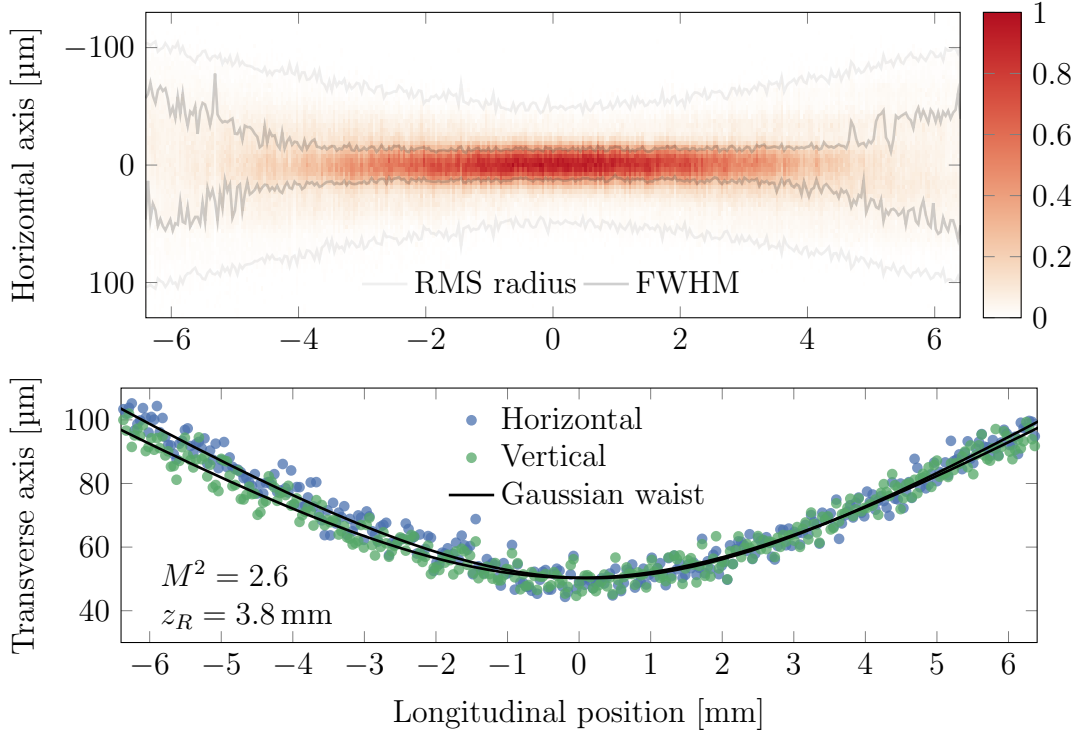
Figure 3.14: Example of a z-scan done at the pre-target diagnostics. A far field image is recorded at every position of the translation stage. Each image is then analyzed to retrieve the beam position, FWHM and RMS radius in both axes. The top plot shows the horizontal slice with the FWHM (gray) and RMS radius (light gray) overlaid. The bottom plot shows the horizontal (blue dots) and vertical (green dots) RMS radius calculated and fitted by a Gaussian waist (black lines). From this waist, the Rayleigh length, the waist and the M^2 are calculated.

be present within the non measured area of the laser beam. On the contrary, an amplitude as low as $0.02\,\lambda$ RMS, which is the order of magnitude of the laser wavefront fluctuations, typically features such modes. Thus, for lack of a more complete measurement, we consider the upper limit of the accuracy of the wavefront measured at the pre-target diagnostic to be $0.02\,\lambda$ RMS, which would decrease the Strehl ratio of a perfect beam to 0.98.

The only optics not included in this calibration of the wavefront are the in-vacuum mirror and the vacuum window. As they are both specified to have laser grade optical quality, they should not deform the wavefront significantly. The unknown is the deformation of the window due to the pressure difference. According to [85], the displacement of the vacuum
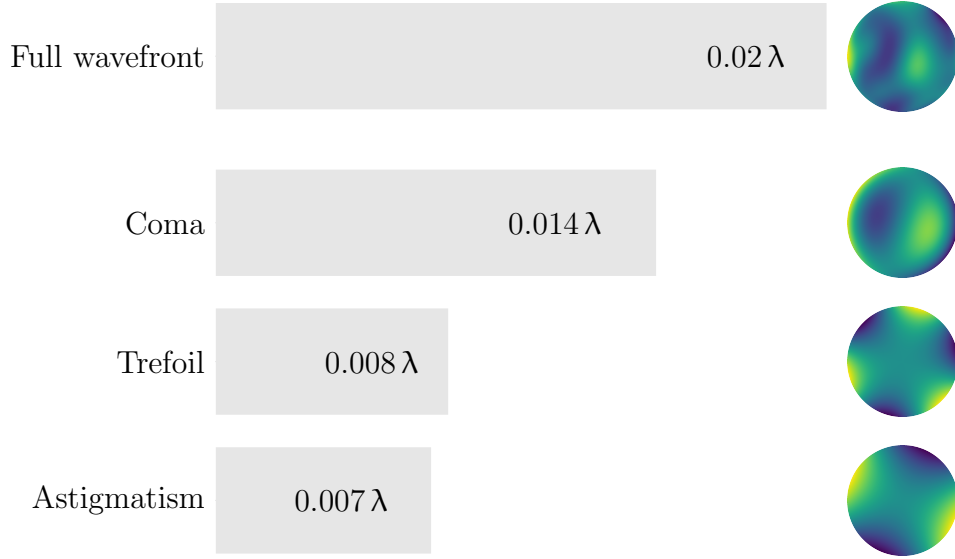
Figure 3.15: Wavefront difference between the entrance of the EVOC diagnostics and the position of the wavefront sensor. The amplitude indicated corresponds to the RMS amplitude. The first line is the measured difference, which amounts to $0.02\,\lambda$ RMS and $0.14\,\lambda$ PTV. The bottom lines show the amount of the most prominent Zernike mode and their wavefront map oriented at the corresponding angle.

window Δz can be calculated from the material constants, the window dimensions and the pressure difference:

$$\Delta z(r) = \frac{3}{16}\,\frac{P\,(1 - \nu^2)}{E\,h^3}\left(R^2 - r^2\right)^2 , \qquad (3.10)$$

with $P = 1\,\mathrm{atm}$ the pressure difference, $\nu = 0.17$ and $E = 71.7\,\mathrm{GPa}$ the Poisson's ratio and the Young's modulus of fused silica, and $h = 3\,\mathrm{mm}$ and $R = 8\,\mathrm{mm}$ the window thickness and radius, respectively. The maximum window displacement is then $\Delta z(0) = 39\,\mathrm{nm}$ and the radius of curvature of the window in the center is $410\,\mathrm{m}$. Using the lensmaker equation, we calculate the resulting focal lens of the now meniscus-like window to be $397\,000\,\mathrm{km}$. Therefore, the bending of the vacuum window can safely be ignored, and we can consider that the EVOC diagnostics are good enough for the purpose of measuring and optimizing the laser wavefront for the laser-plasma experiment at LUX.

3.4.4 Post-target diagnostics

In order to diagnose the laser interaction with the plasma, it is relevant to measure the laser properties after the interaction in the target. For this purpose, a wedge can be placed in the beam before it is dumped to reflect a small fraction of the laser energy out of vacuum (see figure 3.16). A 20 mm hole is drilled in the substrate to let the electron beam go through undisturbed, up to 6 mrad half-angle divergence. The electron beam divergence is typically less than 1 mrad which leaves additional margin to account for the pointing jitter of the beam and to steer it.

This wedge is placed at 80 % of the focal length while the full power beam will be in the beamline. It is therefore in a dangerous position. To estimate the risk, we calculate the B-integral using the maximum theoretical available power, 200 TW. We obtain a value of 450, which is higher than the typical limit set to avoid self-phase modulation, which is in the order of 1. However, we are interested here in self-focusing which would locally enhance the fluence and eventually lead to damage in the bulk of the optic that happens at higher intensity than self-phase modulation. Furthermore, the beam is divergent, against which self-focusing has to act. Finally, the collapse dynamics of high-power super-Gaussian beam are fundamentally different than Gaussian beams [86], which reduces the peak fluence of such a self-focused beam. Finally, based on past experiences from different labs using similar laser systems, it was estimated—and later on experimentally proven—that the wedge is indeed safe from laser induced damage.

Afterwards, the beam goes through a vacuum window, with a B-integral of 1.6 and hits a second holed wedge on air. The purpose of this hole is to allow for an on-axis demagnifying telescope design. As the temporal properties of the pulse have to be kept as close to the in-vacuum ones as possible, an all-transmissive telescope for a large diameter beam would add a significant amount of material and therefore change the laser dispersion. Therefore, the laser beam is back-reflected and focused through the 2nd wedge by a $f = 825$ mm spherical mirror. There, the largest beam size is 15 mm for a projected hole size of 20 mm. Behind the holed wedge, two more wedges (not shown in figure 3.16) steer the beam and further decrease the energy before the focus of the telescope to avoid air breakdown. They can be replaced by mirrors with identical dimensions to align a low power beam more easily. Finally a best-form lens collimates the beam at a 3 mm diameter, in order to decrease the spherical aberration. In fact, after the telescope, $+0.016\,\lambda$ RMS are added to the wavefront, mainly due to the spherical mirror. The point spread function (PSF) of such a system reaches
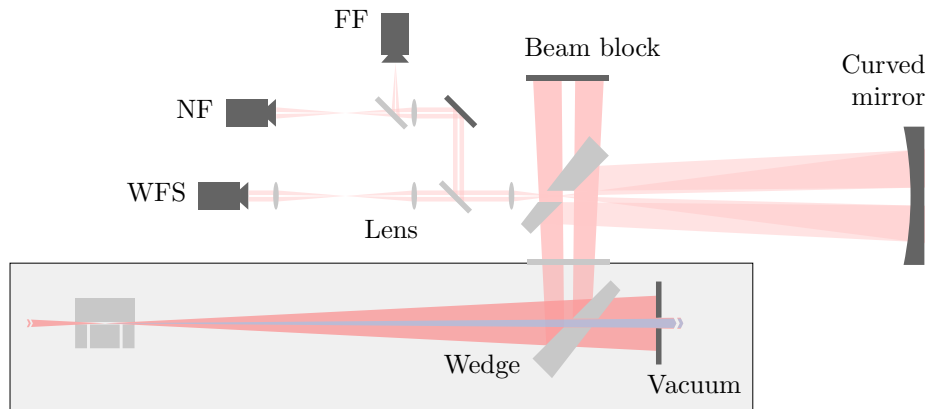
Figure 3.16: Schematic of the post-target diagnostics. A holed wedge in vacuum outcouples about 1 % of the laser intensity. A second holed wedge attenuates further the beam. An on-axis telescope composed of a spherical mirror and a best-form lens demagnifies and collimates the beam through the hole of the 2nd wedge. After collimation, the beam is split towards three diagnostics: a far field camera to measure the mode quality out of the target, a near field camera and a wavefront sensor which image the plane of the first wedge. Most of the laser energy is dumped in vacuum on stacked layers of tinted glass which absorb the laser wavelength. NF, near field camera; FF, far field camera; WFS, wavefront sensor.

a Strehl ratio of 0.99. Thus, most of the aberrations measured by the wavefront sensor will stem from either the laser beam itself or the interaction with the plasma.

Once the beam is collimated, it is split between several diagnostics. However, due to the hole in the beam profile, the near field measurements (intensity profile and wavefront) need to image the plane of the 1st wedge to avoid diffraction rings. The far field is also measured as it represents the output mode of the capillary target. The added diffraction due to the hole is changing the amplitude ratio between the main peak and the side lobes of the far field profile, as shown in figure 3.17, but the main features are similar to the in-vacuum focus.

Again, to ensure the accuracy of the measurements, the setup has to be calibrated to account for misalignment of the optics. However, due to the beam size at the entrance of the demagnifying telescope, such a calibration is not as straightforward as for the pre-target diagnostics. Moreover, a direct measurement after the target when the beamline is vented is difficult
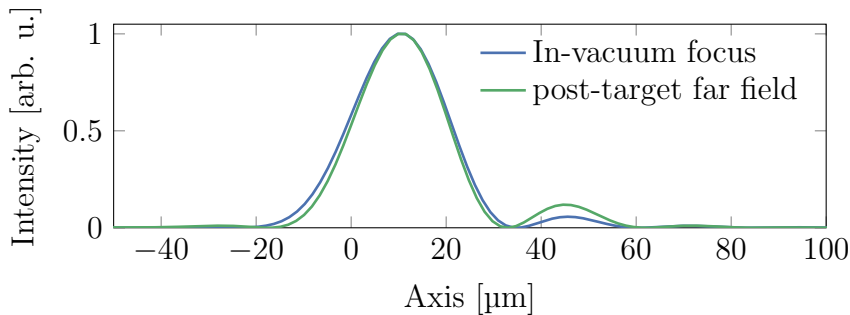
Figure 3.17: Influence of the holed wedge on the far field measurement. The lineout of the simulated post-target far field with $0.1\,\lambda$ RMS of coma (green) is compared to the focus in vacuum (blue). The main peak is slightly smaller (FWHM decreased by $6\,\%$), and the first side lobes are about twice stronger due to the hole in the wedge. Furthermore, the peak intensity of the far field is reduced by $22\,\%$ as the beam contains less energy and is more diffracted compared to the focus.

due to the small size of the vacuum chambers[9]. To circumvent this issue, a fiber tip can be placed in the target chamber to create a point source with a secondary fiber-coupled continuous laser. It would create a source with a close-to-perfect spherical wavefront at the actual ANGUS laser focus position. Measuring the wavefront of this laser at the post-target diagnostics would then be a direct measurement of the setup aberrations. Such a calibration is planned, but has not been implemented yet.

Apart from the spatial diagnostics mentioned above, a spectrometer and an energy sensor can also be installed using the leaks from the two additional wedges or using more beamsplitters in the collimated beam. In the current version of the setup, no time diagnostic is implemented due to strict constraints on the available space in the beamline tunnel. However, it is possible to upgrade it, using an off-axis parabola to collimate the beam instead of a lens. This would again ensure a more accurate measurement of the temporal profile. Furthermore, the collimated beam can also be used to synchronize the main laser to a pump and probe beam. Synchronization measurements done by S. W. Jolly, T. Eichner and M. Schnepp have shown a sub-10 fs jitter between the two beams in December 2017.

As it has been outlined through this chapter, the measurement of the wavefront is critical and carefully considered. In fact, a bad quality of the

---

[9]designed as such for an efficient pumping, see [76]

focal spot is not only detrimental to the electron acceleration because it decreases the available energy in the FWHM [87], but it heavily worsens the spatial contrast of the focus which increases the energy dumped in the capillary target and drastically reduces its lifetime. A careful determination of the focal spot quality and the spatial contrast is therefore necessary.

Chapter 4

Focal spot quality measurement and control

Throughout this chapter, we will investigate and quantify the focal spot quality, as well as the spatial contrast. As the target used for the LUX experiment is a sapphire capillary, we have to be sure that the intensity hitting the front side of the target is low enough to avoid fast damage to the sapphire. The typical full width at half maximum (FWHM) size of the focal spot is about 25 µm and the capillary dimensions used so far are 300 µm and 500 µm. Therefore, we are not only interested in the shape of the main peak, but also on the intensity of the wings at a scale 20 times larger than the FWHM. To study the spatial contrast, we first ensure the good quality of the laser beam wavefront and the influence of the residual aberrations on the focus. We then perform a high-dynamic-range focal spot measurement to characterize the wings of the intensity profile and compare the results to the wavefront measurement. Potential sources of discrepancy are investigated before looking into the target lifetime.

4.1   Wavefront quality of the ANGUS beam

As explained in the previous chapters, the wavefront of the ANGUS beam is controlled by a deformable mirror placed before the compressor. This deformable mirror can correct the aberrations of the beam coming from the amplifiers and compensate those coming from the compressor, the transport beamline and the focusing off-axis parabolic mirror. Therefore, it is not necessary to investigate the wavefront of the beam coming from the amplifiers in order to obtain a good focal spot on target. However, it is useful to ensure that the wavefront is not so degraded that it would modify the near field while propagating until the deformable mirror. Such a sanity check can easily be done by measuring the far field distribution.
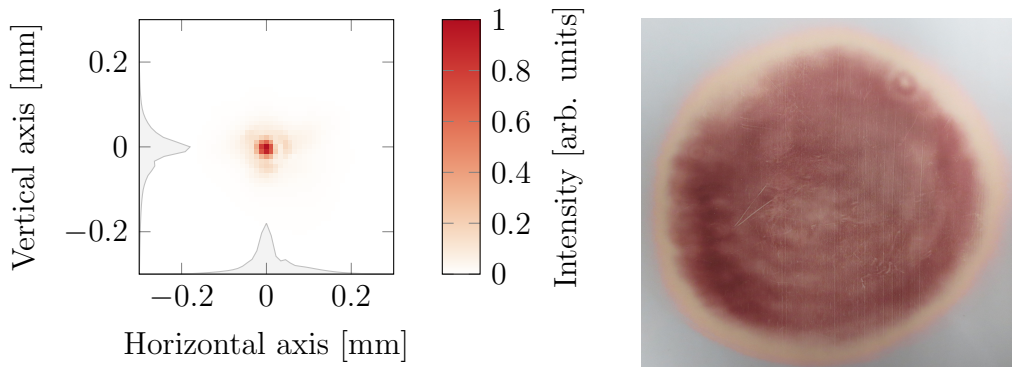
Figure 4.1: Far field measurement of the Amp. 2 beam (left) before the last magnification. The horizontal and vertical projections (shaded area) are shown next to their respective axes. Near field distribution (right) taken with a photosensitive paper in front of the deformable mirror on the 26$^{\text{th}}$ of July 2016.

4.1.1 After amplification

Figure 4.1 shows the far field at the output of the Amplifier 2 and the near field in front of the deformable mirror. The axes of the far field are scaled to match the f-number of the LUX focusing parabola ($f\# \simeq 25$), resulting in a FWHM of 34 μm. While it is not perfect, the main peak is clearly visible and the amplitude of the side lobes stays below 20 %. Therefore, we can consider that the residual aberrations are low enough to propagate safely the beam over a few meters in order to reach the deformable mirror without degrading the near field profile. The near field measurement using a photosensitive paper confirms our assumption. We now concentrate on the laser beam after amplification and magnification.

4.1.2 Wavefront quality after correction

Using the pre-target diagnostics (see section 3.4.3) and the deformable mirror, the wavefront is corrected to make it as flat as possible close to the target. The residual wavefront, shown in figure 4.2, has an RMS amplitude of 0.033 λ (or λ/30) with a PTV amplitude of 0.25 λ (or λ/4). Calculating the point spread function, we obtain a pattern close to the diffraction limit with a Strehl ratio of 0.96. Keeping in mind that the pre-target diagnostics are not perfect, we can estimate the actual in-vacuum Strehl ratio to be at most 0.94, which is still very close to the diffraction limit.

Full wavefront	0.033 λ
Coma	0.013 λ
Pentafoil	0.011 λ
Tetrafoil	0.011 λ
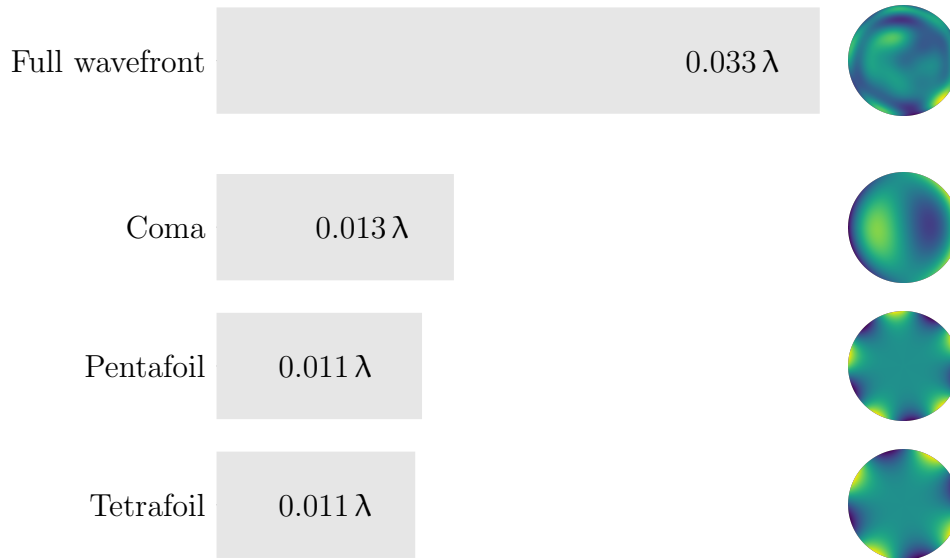
Figure 4.2: Wavefront measured at the pre-target diagnostics after optimization with the deformable mirror.

Using the pre-compressor diagnostics, we can furthermore observe the wavefront aberrations coming from the compressor, the transport beamline, and the off-axis parabola together in order to measure the magnitude that the deformable mirror compensates for. The measured wavefront and the main aberrations are reported in figure 4.3. A large amount of astigmatism is present, which heavily degrades the wavefront. The total RMS amplitude is $0.9\,\lambda$, and the calculated Strehl ratio is 0.03. The far field camera confirms the presence of such a strong astigmatism (see figure 4.4), as we observe a large cross-shaped far field pattern.

Even though this large wavefront aberration is compensated while propagating through the beamline, it does affect the propagation of the beam and thus alters the near field distribution. We therefore proceed to investigate the magnitude of the near field deformation, and its impact on the far field distribution.

4.2   Near field degradation through the transport beamline

Because the compressor, the transport beamline, and the LUX experiment all operate in a high-quality vacuum and the beam size is large compared to

Full wavefront   0.868 λ

Astigmatism   0.780 λ

Trefoil   0.132 λ

Coma   0.097 λ
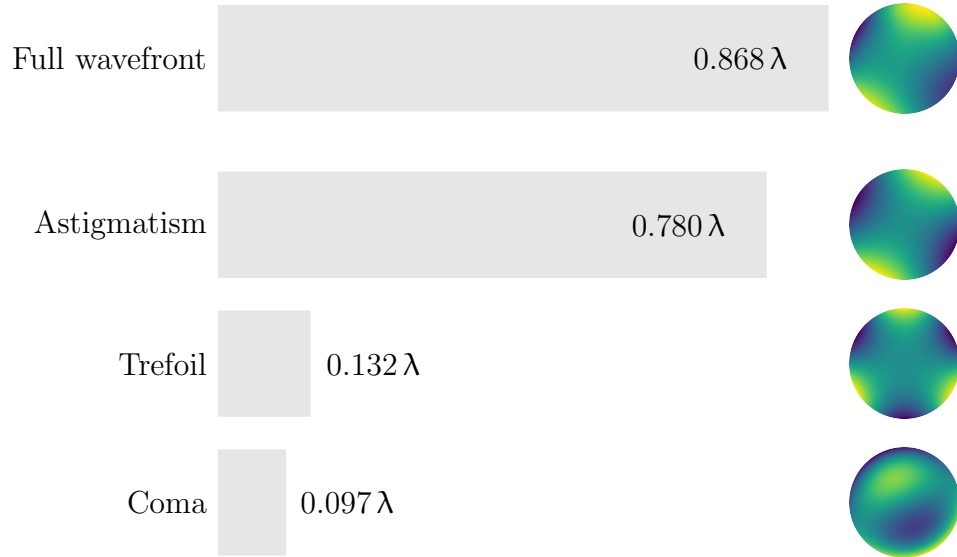
Figure 4.3: Wavefront measured at the pre-compressor diagnostics after optimization at the target with the deformable mirror. The Strehl ratio goes down to 0.03.
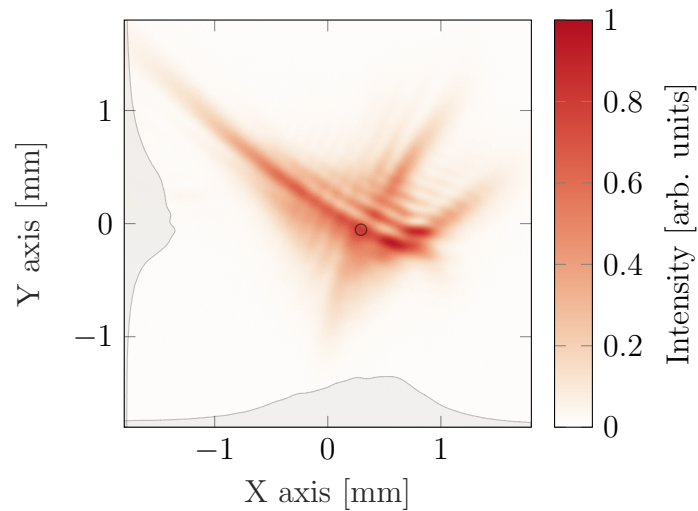
Figure 4.4: Far field at the compressor input after on-target wavefront optimization. The marginal distributions are overlaid (shaded areas). The cross-shape profile is typical of astigmatism. The black circle shows the expected FWHM of about 100 μm for an ideal far field.

the typical CCD chip size, it is very difficult to access directly the near field distribution of the laser beam once it is coupled into the vacuum system. Therefore, the imaging setup built at the entrance of the compressor (see section 3.4.1) allows us to monitor over several tens of meters of propagation within the transport beamline. We remind that this diagnostic uses the leaktrough of a high reflectivity mirror. Therefore some features present within the measured profile might not reflect exactly the actual laser beam itself.

4.2.1   Imaging into the beamline

Figure 4.5 shows the scaled near field distribution at the entrance plane of the compressor (real imaging), and after a propagation length equivalent to 35 m (virtual imaging). One can see that the intensity distribution differs within the overall profile, but the shape itself is rather similar as can be seen from the marginal distributions. The profile at 35 m does extend over a slightly larger area than the profile at the compressor entrance, especially in the horizontal direction. It can be directly related to the large astigmatism present in the wavefront, which tends to increase the ellipticity of the beam.

In order to further validate the imaging properties of the diagnostic setup, we numerically simulate the in-vacuum propagation of the electric field using the wavefront and near field measurements done by the wavefront sensor. The resulting intensity pattern after 35 m is reported in figure 4.5 as well. We can see a very good agreement between the simulation and the measurement. However, the very edges of the beam are not measured by the wavefront sensor and therefore not accounted for with this simulation. The limited measurement aperture also explains why diffraction rings appear in the propagated profile. Nevertheless, from this good agreement, we confirm that numerically propagating the electric field constructed from the wavefront measurement is accurate enough to capture the evolution of the laser beam.

As explained, the imaged beam profile corresponds to the intensity distribution of the beam, assuming it would propagate in vacuum for 35 m with no additional optics. However, thanks to the pre-target measurement, we know that the wavefront does improve through the beamline. The unknown parameter is at which position does it improve and therefore, for how long does the beam propagate with an imperfect wavefront. Thus, these imaged measurements give us an upper limit on the near field deformations we can expect. The actual laser beam near field would reach this limit if
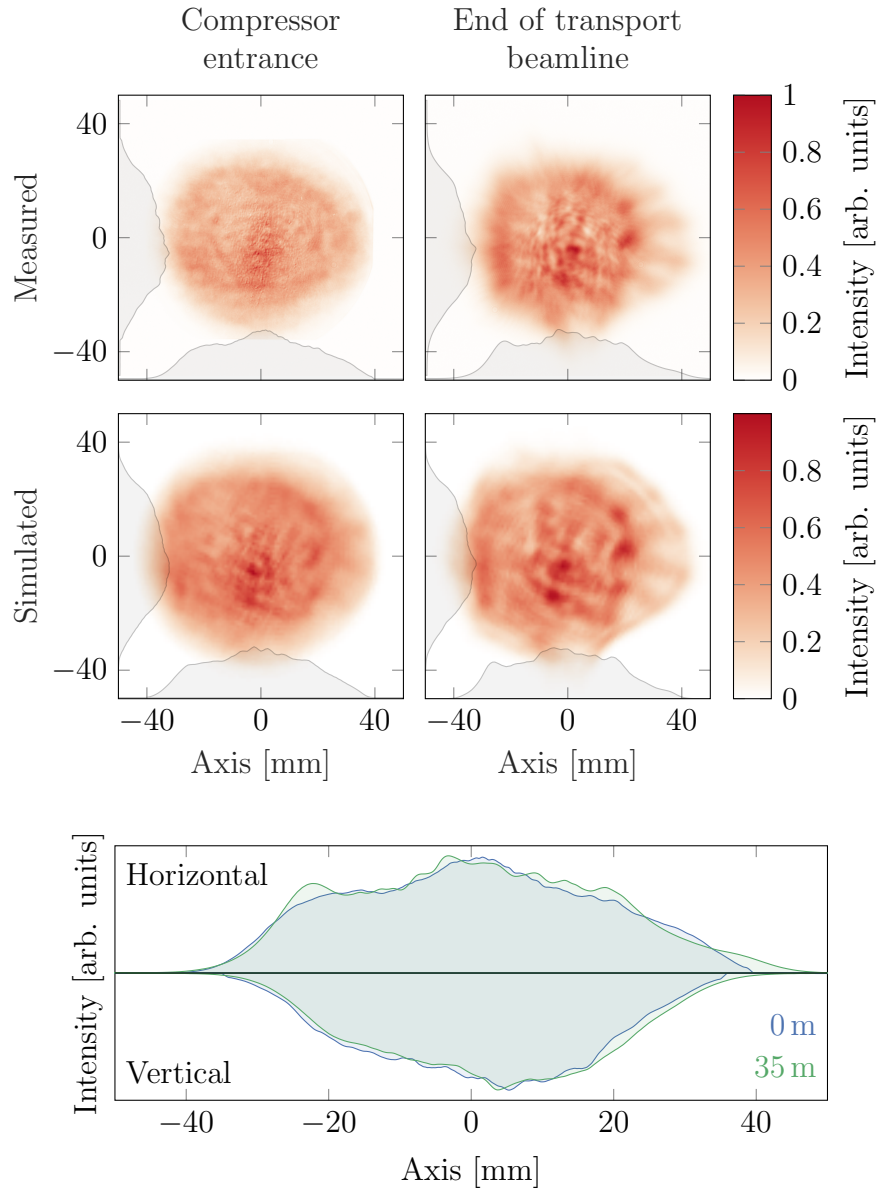
Figure 4.5: Near field distribution imaged at the entrance of the compressor (left) and after 35 m (right) which roughly corresponds to a plane at the end of the transport beamline. The marginal distributions are overlaid (shaded area). The top plots are measured directly using the compressor entrance near field camera, while the middle plots are numerical simulations based on the near field and wavefront measurements before the compressor. The bottom plot reports the marginal distribution for the first two measurements to highlight the similarity of the intensity distribution.

all the aberrations come from the last optic, namely the off-axis parabolic mirror.

4.2.2 Influence on the far field

Using the beam profile imaging the end of the transport beamline, we can however assess the degradation of the focus caused by such a distorted near field profile. For this purpose, we compare the PSF of the measured near field at the compressor entrance assuming a perfectly flat wavefront, and the imaged near field after 35 m of propagation in vacuum with the wavefront measured before the target (see figure 4.2). The calculations assume a wavelength of 800 nm and a focal length of 2 m as used at LUX. The resulting point spread functions are very similar to each other and to the diffraction limit. The FWHM of the propagated beam is 4 % smaller than the FWHM at the compressor entrance (from 23.8 µm to 22.8 µm). As explained above, the propagated profile is slightly larger, so the focalization of this beam would be comparatively smaller. A critical parameter for experiments such as laser-plasma acceleration is the fraction of the energy contained within the full width at half maximum. In fact, the energy in the wings of the focal spot distribution is wasted as it does not couple into the wakefield [10, 87]. Therefore, knowing this fraction of energy in the FWHM is an interesting metric for the LUX experiment and to assess the quality of the focal spot using an integrated quantity (opposite to the Strehl ratio). In this work, we refer to the fraction of the energy within the FWHM simply as an encircled energy percentage. When no value is specified, it shall refer to the actual function $\mathcal{E}_{\mathrm{circ}}(r) = \int_0^{2\pi} \int_0^r I(\rho, \theta)\rho d\rho d\theta$.

Figure 4.6 reports the encircled energy of the two PSF described above, and of a Gaussian beam with the same FWHM as the PSF from the compressor entrance near field for reference. For the compressor entrance, the encircled energy adds up to 52.8 % as the wavefront is ignored. After the 35 m of propagation, it is decreased to 50.9 %. We note that if we also ignore the wavefront after 35 m, the encircled energy is 52.2 % (not represented in figure 4.6), so most of the degradation comes from the residual wavefront measured before the target. We can see from the marginal distribution of the two PSF that the second profile features slightly higher wings, which explains the decrease in encircled energy. Therefore, the change of the near field profile does not have a significant impact on the focal spot.

We remark as well that an encircled energy of 53 % corresponds to an ideal super-Gaussian beam of the 4th order, as reported in figure 4.7. The
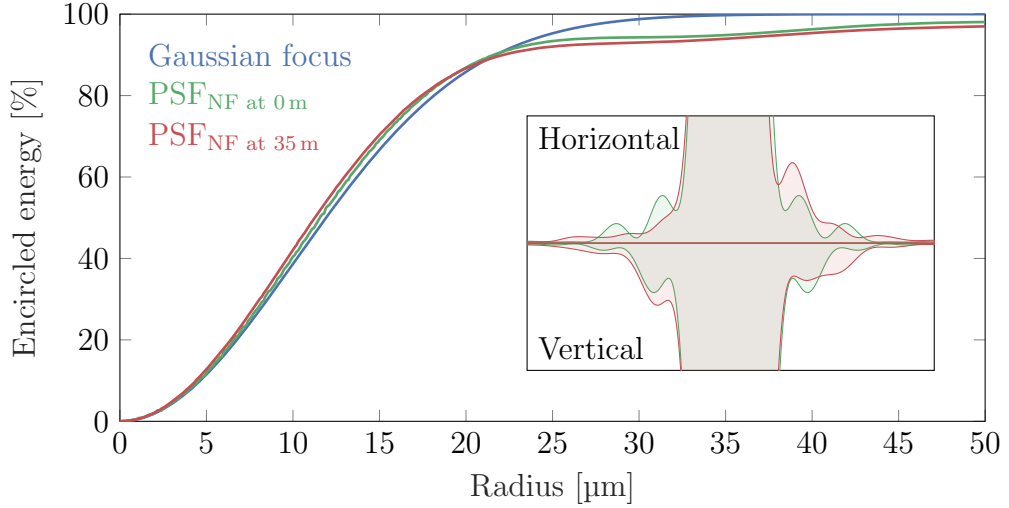
Figure 4.6: Encircled energy of the PSF for the compressor entrance near field with a flat wavefront (green), and the near field after 35 m of propagation with the wavefront measured before the target (red). The encircled energy of a Gaussian beam with the same FWHM is overlaid for reference (blue). The inset shows the zoomed horizontal (top) and vertical (bottom) marginal distributions of the two PSF.

best agreement between a lineout through the near field profile (figure 4.5) and a super-Gaussian fit corresponds to an order of 4 as well.

Considerations on encircled energy

For a Gaussian beam, exactly 50 % of the energy is contained within the FWHM, as the encircled energy of a Gaussian beam $\mathcal{E}_{\text{circ, Gauss}}$ can be calculated by:

$$\mathcal{E}_{\text{circ, Gauss}}(r) \propto \int_0^r \rho e^{-\ln(2)\left(\frac{\rho}{w_{1/2}}\right)^2} d\rho, \tag{4.1}$$

$$\mathcal{E}_{\text{circ, Gauss}}(r) = 1 - e^{-\ln(2)\left(\frac{r}{w_{1/2}}\right)^2}, \tag{4.2}$$

with $w_{1/2}$ the half width at half maximum of the intensity profile and r the radial coordinate. For an Airy disk intensity pattern I_{Airy}, the encircled energy $\mathcal{E}_{\text{circ, Airy}}$ can be calculated by [88]:

$$I_{\text{Airy}}(r) = \left(\frac{2J_1(r)}{r}\right)^2, \tag{4.3}$$

$$\mathcal{E}_{\text{circ, Airy}}(r) = 1 - J_0^2(r) - J_1^2(r), \tag{4.4}$$

74
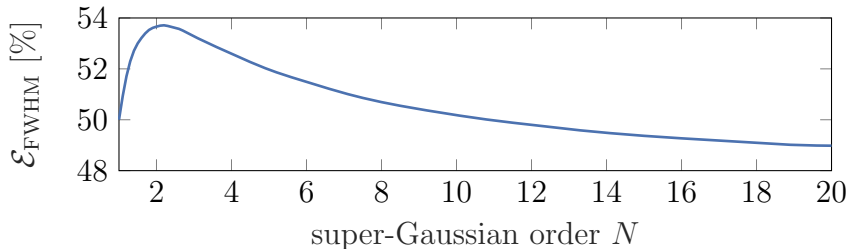
Figure 4.7: Encircled energy of a focused super-Gaussian beam $\mathcal{E}_{\text{FWHM}}$ in function of the super-Gaussian order N. For $N = 1$, the beam is a standard Gaussian and the encircled energy is 50 %.

with J_n the Bessel functions of the first kind. We find that 47.4 % of the energy is contained within the FWHM. For super-Gaussian beams, the analytical description of the focal spot is not straightforward. We can however numerically compute them through a Fourier transform of the near field profile. The fraction of the energy contained in the FWHM depends on the super-Gaussian order, as one would expect. Interestingly, it goes above 53 % for a super-Gaussian order of 2 before decreasing asymptotically towards the limit of 47 % for a flat-top beam (see figure 4.7).

From this analysis, we conclude that the degradation of the near field profile due to the aberrated wavefront present before the compressor and the residual wavefront aberrations—to the precision that we can measure— at the pre-target diagnostic should not have a significant impact on the focal spot quality (only a few percents decrease of the encircled energy). To directly asses its quality, we proceed to measure with a high dynamic range the far field distribution of the ANGUS beam right before the target.

4.3 High dynamic range far field measurement

In order to measure the wings of the focal spot, i.e. the area of the intensity distribution with a signal several orders of magnitude lower than the peak intensity, it is important to investigate first the capabilities of the hardware used at LUX.

4.3.1 High dynamic range intensity measurement

The camera used at the pre-target diagnostics to measure the focal spot intensity distribution has a typical background level of 17 counts, for a

peak signal of the focal spot that is usually around 1000 counts. Thanks to the triggering of the camera, the exposure time is set at the lowest setting of 16 µs, and the camera is isolated from the environment light by shielding walls. Therefore, the background level measured by the camera is the lowest possible with the current setup. One could take full advantage of the 12 bits depth of the camera (4096 counts) and increase the laser energy on the camera by four, in order to reach the highest dynamic range, allowing us to measure the wings above the 5×10^{-3} level (with the peak intensity level being 1). To improve this dynamic range, we first increase the laser signal in order to saturate the main peak. Thus, the signal of the wings will rise above the background level and can be analyzed. Then, by combining several images with different intensity level, the saturated areas can be replaced by non-saturated images and therefore the whole intensity profile can be reconstructed. It is similar to the HDR (High Dynamic Range) techniques used in photography which combine several images with different exposure time. The limit of this technique is reached when the laser intensity is so strong that the main peak generates too many electrons in the CCD, which then overflow in the neighboring pixels. In such a situation, the pixel value measured next to the saturated area would be incorrect.

In order to increase the laser signal on the camera, we installed a half-wave plate before the wedge placed right before the camera (see figure 3.13). As the reflectivity of the fused silica wedge depends on the light polarization as shown in figure 4.8, the reflected signal can be increased from 0.66 % up to 8.1 %, which is more than one order of magnitude. Furthermore, a couple of neutral density (ND) filters are mounted directly on the camera to reduce the laser intensity during everyday operation. One of them was removed to access another order of magnitude. At the highest signal (highest wedge reflectivity and ND filter removed), some of the saturated signal started to leak on the neighboring pixels. Therefore, no additional ND filter could be removed. For each setting, ten images were acquired and averaged in post-processing to mitigate the fluctuations of the intensity distribution and the pointing jitter.

While a ND filter with a bad surface quality could alter the beam, they are mounted close to the focal plane which limits the impact of this optic. Furthermore, even with the worst ND filter of the ANGUS lab with a measured transmitted wavefront error of $0.4\,\lambda$ RMS, the focal spot shape stays similar, especially the characteristic features of the main peak and the first side lobes. Significant discrepancies between the unaltered focal spot and the beam going through the ND filter appear at the 10^{-5} level
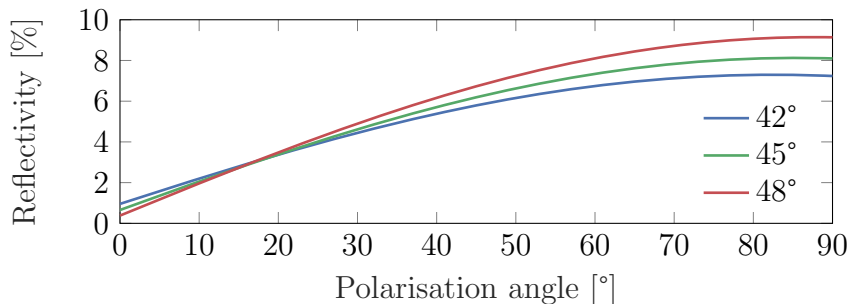
Figure 4.8: Polarization dependent reflectivity of a fused silica wedge for different angles of incidence.

according to simulation based on measured data. However, the ND filters are used to measure the main peak and not the side lobes. Therefore using such optics—which wavefront error is not always quantified—close to the focal plane should still results in accurate measurement of the focal spot.

To combine two images together, the signal level must be scaled such that the same part of the beam corresponds to the same intensity. Therefore, an area where the signal level is neither saturated nor too close to the background level for both images is selected. Then, the intensity within this area is compared between the two images and the ratio can be used to scale them accordingly. Doing this operation for all the images, and paying attention to an eventual position mismatch between the intensity patterns, the saturated area of the image can be replaced by a less saturated scaled image until the full focal spot is reconstructed. Figure 4.9 shows schematically the whole process.

4.3.2 Measurement of the focal spot before the target

At the pre-target diagnostics, five images were combined, up to the limit of the CCD camera. The combined image is shown in figure 4.10 in logarithmic scale to enhance the wings of the focal spot, and normalized to correspond to a 35 fs pulse with 5 J. The peak intensity is then $1.0 \times 10^{19}\,\mathrm{W\,cm^{-2}}$, which corresponds to a normalized vector potential a_0 of [72]:

$$a_0 = 0.85 \cdot \lambda\,[\mathrm{\mu m}]\,\sqrt{I_0\,[10^{18}\,\mathrm{W\,cm^{-2}}]} = 2.1, \tag{4.5}$$

with λ the wavelength and I_0 the peak intensity. For the single non-saturated image normalized to the peak intensity, the average background
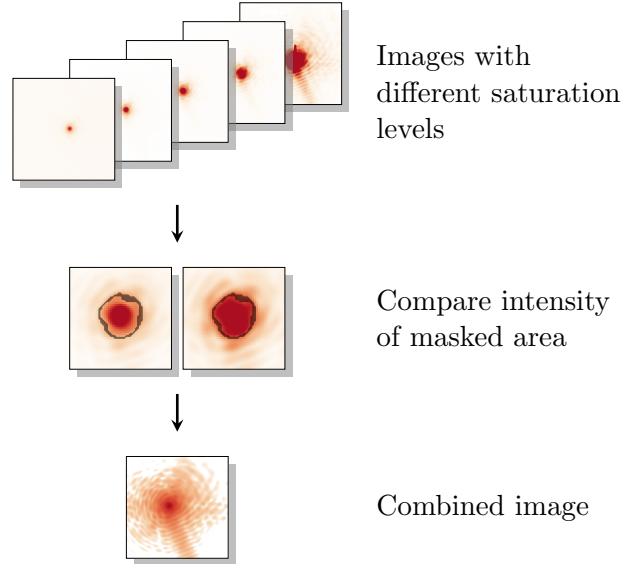
Figure 4.9: Schematic of the high dynamic range combination. Several images with different saturation levels are scaled accordingly and combined together to obtain a much larger dynamic range than with a single image.

level is at 2.0×10^{-2}. For the combined image, it is reduced to 2.9×10^{-5}, which is almost three orders of magnitude lower. The relative standard deviation of the background amounts to 9% for both images. It could eventually be further reduced by using noise-removal filtering schemes. Nevertheless, thanks to the high dynamic range measurement, the far field distribution of the ANGUS laser can be observed with a signal to noise ratio of $34\,000$. We note that the wings extend further than the typical dimensions of the capillary target, which can be troublesome if too much energy ends up in the front surface of the target and damages it. Furthermore, it limits the amount of energy contained in the FWHM, which then limits the available energy for the experiment. The measured FWHM is $26.8\,\mu m$, which is 15% larger than the ideal FWHM based on the measured near field profile. However, the D4σ diameter is equal to $195\,\mu m$. Indeed, as this quantity is an integrated quantity where the intensity is weighted by the square of the distance from the center of mass, the wings heavily influence the calculated diameter. From the lineouts, we can observe that the wings are about one order of magnitude higher than expected from the wavefront measurement. Furthermore, thanks to the high signal to noise ratio, the encircled energy can be accurately calculated.

On figure 4.11, the encircled energy of the measure focal spot, of an ideal super-Gaussian beam of the 4th order, and of the PSF from the
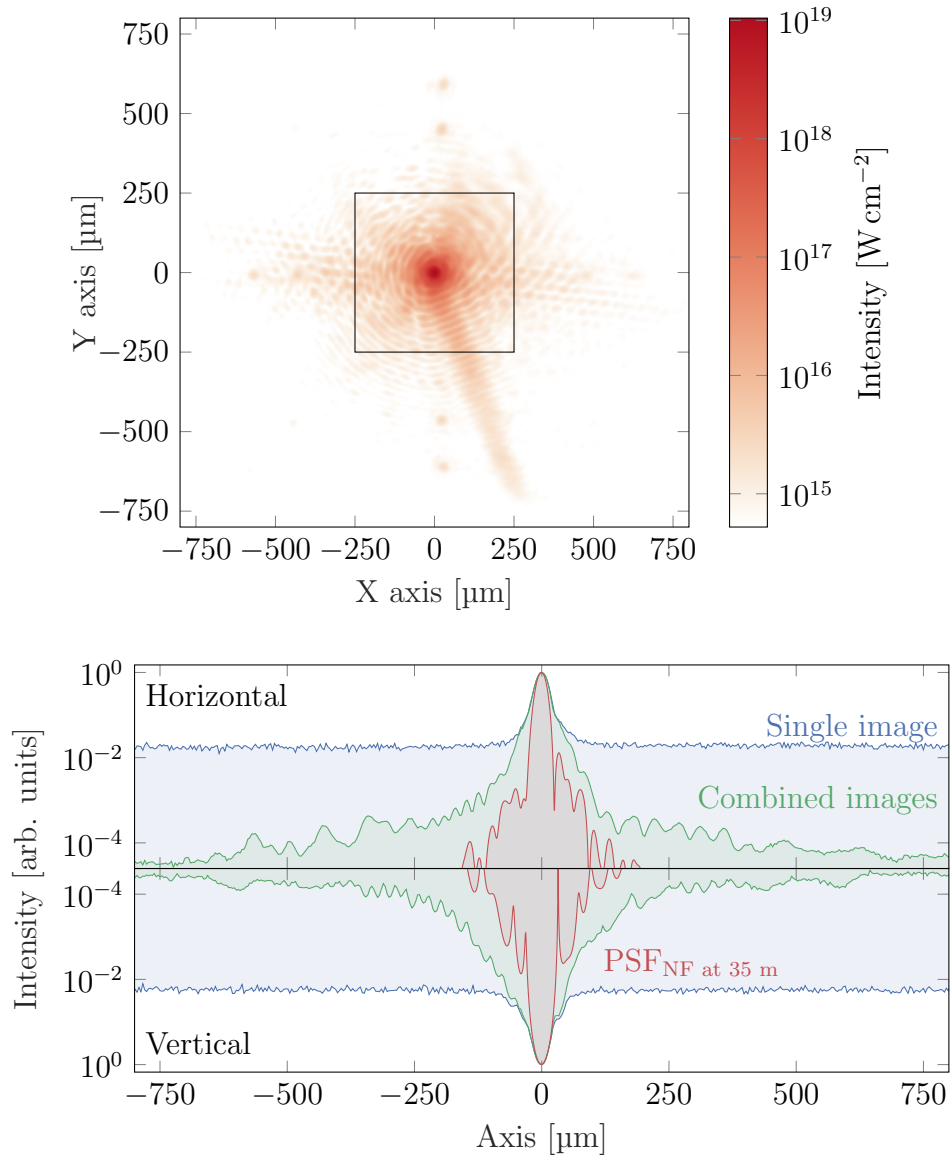
Figure 4.10: Focal spot in logarithmic scale (top) assuming a 5 J 35 fs pulse. The black rectangle represents a capillary target of $500\,\mu m$ typically used at LUX. The dots above and below the main peak correspond to ghost reflections, most likely coming from ND filters. The horizontal and vertical lineouts (bottom) are shown in logarithmic scale for a standard camera image (blue) and for the combined image using the process described earlier (green). The lineouts from the PSF of the near field propagated for 35 m is also shown (red). The background level is reduced by more than two orders of magnitude using the combined images, which unveils the features of the wings.

measured near field already reported previously (figure 4.6) are displayed. The measured focal spot is clearly worse than the ideal case. Within the FWHM, only 32.7 % of the energy is present, compared to the 51 % estimated from the near field and the measured wavefront. Only at a radius of 20.4 µm is half of the energy contained. At 80.3 µm, 90 % of the energy is encircled. It is more than three times larger than for the near field PSF. Finally, a relevant parameter for the experiment is how much energy hits the front surface of the target—assuming the focal spot is exactly centered and placed at the entrance. Due to the target geometry, the ensquared energy of the focal spot is more appropriate than the encircled energy, and the definition is analogous but uses Cartesian coordinates instead of polar coordinates. For a 500 µm target, 1.3 % of the energy is blocked. For a 300 µm target, it amounts to 3.8 %. These quantities correspond to an ideal case so they are lower limits on the amount of energy blocked by the target aperture. The usual position jitter of the focus is below 5 µm. Such a jitter would increase the energy dumped in the target to 1.34 % of the total energy. To reach 1.5 %, the focal spot has to be displaced by at least one time the FWHM. On the other hand, the longitudinal position of the focal spot in the target is more likely to increase significantly the amount of energy hitting the target as the wings of a super-Gaussian focus spread out faster than the main peak when moving away from the focal plane, as represented in the z-scan on figure 3.14.

From the observation of the wings of the focal spot using the high dynamic range measurement, we observe that the actual focal spot is much wider than the simulation based on the wavefront and near field measurement. Several reasons can be given to explain qualitatively why the direct far field measurement deviates from the expected pattern. We therefore try to quantify a few of these potential sources of discrepancies in order to assess their relative impact on the focal spot degradation.
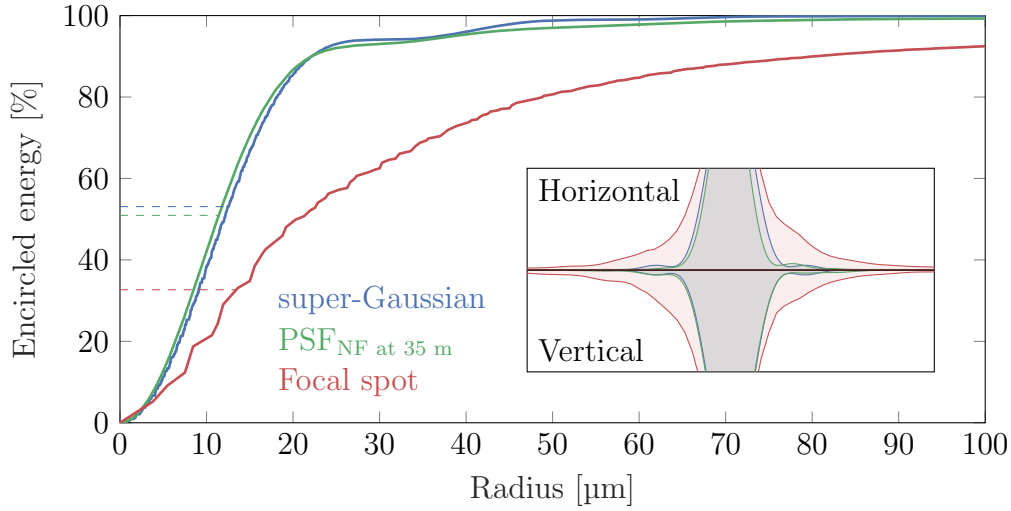
Figure 4.11: Encircled energy of the measured focal spot with a high dynamic range (red). An ideal super-Gaussian focus (blue) and the PSF of the propagated near field (green) are shown for comparison The dashed lines represent the fraction of the energy encircled in the FWHM. The inset represents the bottom half of their marginal distributions.

4.3.3   Potential reasons for discrepancies

Some assumptions have been made previously, on either the measurements themselves or on the laser beam properties. Thus, the chromatic aberrations of the pre-target diagnostics have been ignored. The setup is composed of two to three lenses (depending on the specific diagnostic) and a vacuum window placed in a divergent beam. Therefore, the refraction would slightly affect each wavelength differently. Furthermore, as mentioned above, the wavefront sensor does not measure the very edges of the near field profile due to its dynamic range. We will asses the importance of this outer edge for the far field distribution. Finally, the spatio-temporal couplings such as angular chirp or pulse front tilt have been ignored, mainly due to the lack of an accurate diagnostic to quantify these complex correlations.

Chromaticity of the pre-target diagnostics

The pre-target diagnostics has been reproduced using Zemax[1] and the lens models given by the manufacturer. Then, the point spread function of the setup is simulated for several wavelengths ranging from $750\,\text{nm}$ to $850\,\text{nm}$.

---

[1] www.zemax.com
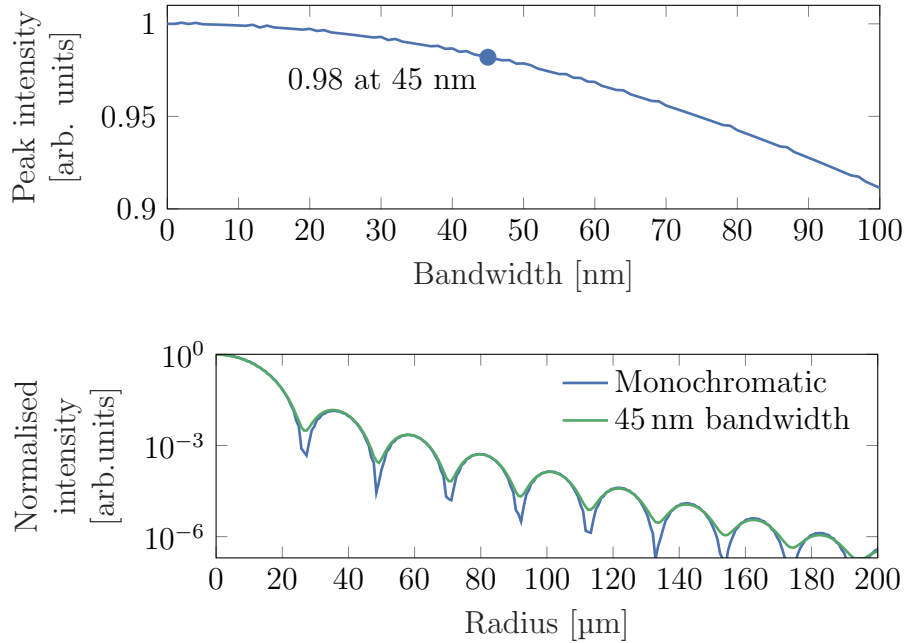
Figure 4.12: Decrease of the peak intensity in focus in function of the laser bandwidth (top), and lineout of the far field distribution (bottom) for a monochromatic beam (blue) or for a 45 nm bandwidth beam (green).

Using Parseval's theorem, we can obtain the time-integrated fluence profile $F(x,y)$ of the PSF from the simulated frequency decomposition $\widetilde{E}(x,y,\omega)$:

$$F(x,y) = \int |E(x,y,t)|^2 \, dt = \frac{1}{2\pi} \int \left| \widetilde{E}(x,y,\omega) \right|^2 d\omega, \qquad (4.6)$$

which corresponds to the image recorded by a camera. We compare the peak intensity of such a polychromatic image for several bandwidths to a monochromatic image at 800 nm. We can therefore estimate by how much the measured peak intensity is decreased compared to the in-vacuum focus due to the imperfect optics. Figure 4.12 shows this decrease with respect to the bandwidth. For a 45 nm bandwidth laser beam, the peak intensity is decreased by 2 %. Furthermore, the lineout of the intensity profile for a monochromatic beam and a 45 nm bandwidth beam are almost identical. As the position of the monochromatic side lobes is proportional to the wavelength, the polychromatic wings tend to average out these lobes. However, the overall intensity level of the wings is independent of the bandwidth. Therefore, the chromaticity of the diagnostics does not explain the mismatch of the measured far field.

Measurement mask of the wavefront sensor

To avoid measurement errors due to a bad signal to noise ratio, the wavefront sensor software usually limits the measurement aperture. Therefore, the wavefront at the edges of the beam profile are not measured. A standard setting considers only the signal at a level above 50% of the maximum signal. Similar settings are used for the wavefront correction. Thus, the wavefront is corrected only on the central area. After such a wavefront correction using a HASO sensor from Imagine Optics, the wavefront was measured by a SID4 from Phasics which allows more control on the dynamic range. Two settings were used to measure the wavefront:

- a signal filtering set at 50% of the range, which corresponds to a measured diameter of $67\,\mathrm{mm}$ and encloses 90% of the total energy,

- a filtering at 5%, which corresponds to a diameter of $79\,\mathrm{mm}$ and encloses 99.5% of the total energy.

In the first case, the wavefront RMS amplitude is 0.04λ with a Strehl of 0.94. The encircled energy (see figure 4.13) is close to ideal and amounts to 51%. In the second case however, we observe that higher amplitude modulations are present in the ring not measured in the first case. The wavefront RMS amplitude is then 0.16λ (4 times larger), and the Strehl ratio is 0.68. We observe a decrease of the encircled energy to 43%, and the lineouts of the PSF clearly show that the wings are several orders of magnitude higher compared to the small measurement aperture.

We note that approximately the same amount of energy is included in the main peak of the focal spot for both situations. The FWHM is larger by 3% for the full aperture. For the small aperture, the encircled energy is 51%, but only 90% of the total pulse energy is considered. Therefore, the main peak should contains about 45% of the total energy, which is similar to the full aperture measurement. Nevertheless, even considering the reduced energy, simulations based on the smaller aperture do not give a faithful representation of the full far field distribution.

Spatio-temporal couplings

So far, the temporal and spatial properties of the laser beam have been considered independently. However, couplings such as angular chirp can increase the focal spot size as each wavelength has a different propagation direction and therefore is focused at a different transverse position, which increases the dimension of the beam in the direction of the angular chirp.

Figure 4.13: Influence of the wavefront measurement mask on the PSF. The horizontal and vertical lineouts of the PSF (top) and the encircled energy (bottom left) are shown for the wavefront measured on a 79 mm aperture (blue) or a 67 mm aperture (green). The full aperture wavefront (bottom right) and the 67 mm aperture (white dashed circle) show how flat the wavefront is only within the corrected aperture. The outer ring features aberrations which degrade the PSF quality. Therefore, the wings are several orders of magnitude higher and the encircled energy is decreased by about 15 % (from 50.6 % to 43.3 %, dashed lines).

To simulate such an effect, we assume that the beam has an angular chirp in the horizontal plane, which could easily be introduced in practice by a misalignment of the compressor grating. We note that a spatial chirp does not change the fluence profile in the far field.

Figure 4.14 shows the horizontal and vertical lineout in logarithmic scale, as well as the encircled energy for a PSF free of angular chirp and for a PSF with an angular chirp φ_{ac} of 0.35 µrad/nm. Apart from the angular chirp, the simulated beams are ideal super-Gaussian beams with a flat wavefront. According to [89], such an angular chirp could be obtain with the ANGUS compressor if the gratings parallelism is off by 170 µrad. Due to the spatial dispersion, the horizontal FWHM is increased by almost 50 %. Thus, the peak intensity is decreased by the same factor. Furthermore, the dispersion washes out the diffraction rings in the horizontal axis, as can be seen by the smooth horizontal lineout in figure 4.14. However, the amplitude of the wings stays at the same average value and therefore, the encircled energy in the FWHM is unchanged. We do observe that the encircled energy curve is slightly different, and in general more smooth because the diffraction rings are washed out by the dispersion.

From these three simulations, we can first conclude that the chromatic aberrations of the pre-target diagnostics are too little to significantly affect the measurements and therefore cannot explain the large mismatch between the wavefront measurement and the focal spot measurement. On the other hand, the wavefront aberrations seem to reproduce the increase of the focal spot wings and thus the decrease of the encircled energy, but does not explain the increase of the main peak size. The presence of spatio-temporal coupling could be an explanation for this larger spot. However, angular chirp only increases the beam in one direction, so only higher order couplings could lead to a symmetrical widening of the beam as we observe. To improve the focal spot quality, one would need to first improve the wavefront correction loop in order to include as much of the beam profile as reasonably possible. The accuracy of the wavefront measurement with a bad signal to noise ratio needs to be considered. Concerning spatio-temporal couplings, a retrieval of the spatio-temporal electric field is possible [90], but it is difficult to implement and therefore needs careful planning. However, the angular chirp can be rather easily tuned by adjusting the angle of the compressor gratings in order to optimize the focal spot FWHM.
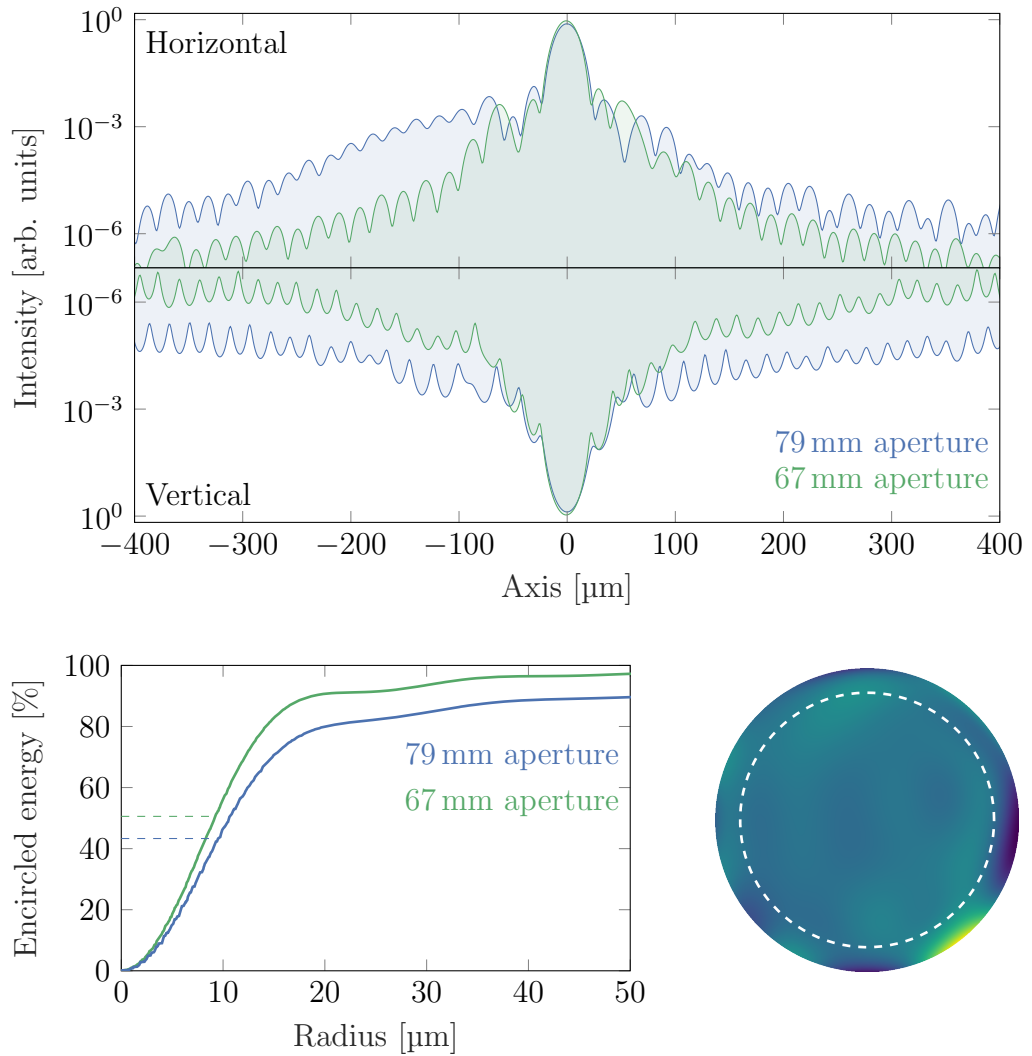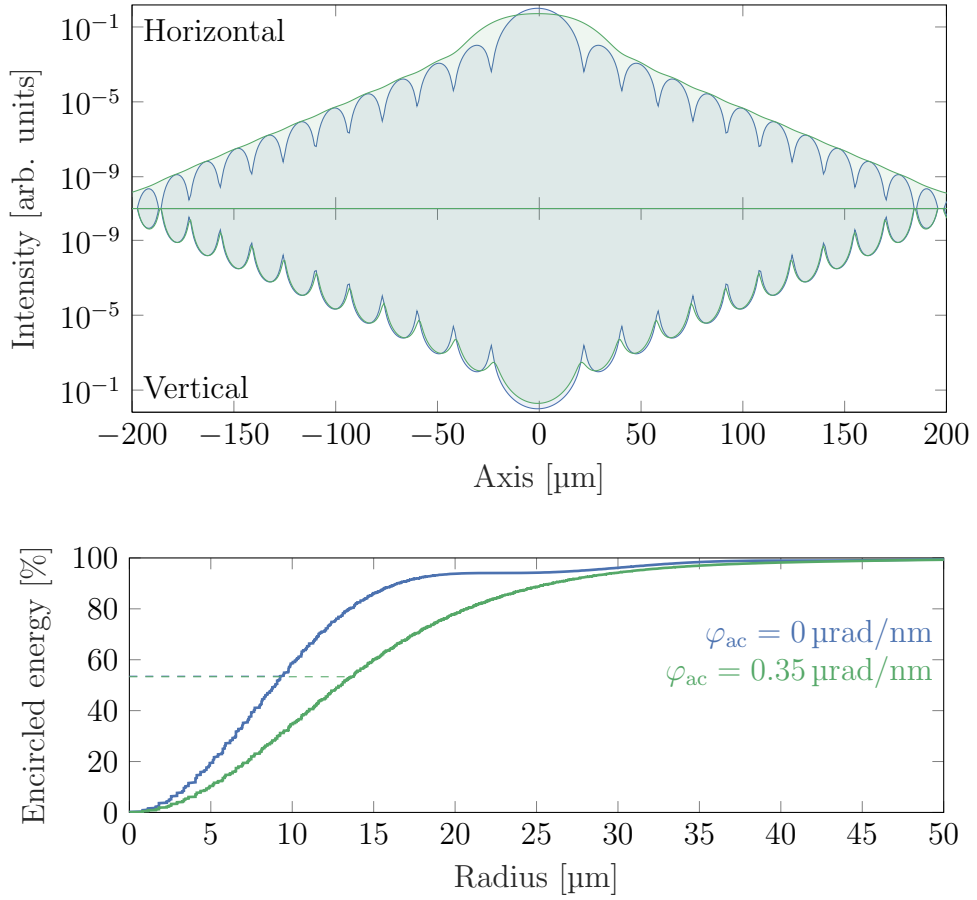
Figure 4.14: Influence of the angular chirp on the PSF. The horizontal and vertical lineouts of the PSF (top) and the encircled energy (bottom left) are shown for a beam without angular chirp (blue) and with an angular chirp φ_{ac} of $0.35\,\mu\mathrm{rad/nm}$ (green).

4.4 Phase retrieval: an alternative wavefront measurement

As seen previously, the measured wavefront and near field are not sufficient to properly reproduce the far field intensity distribution. An alternative method to obtain an information of the laser wavefront is to used a phase retrieval algorithm. From two intensity measurements, one in the object domain (near field) and one in the Fourier domain (far field), and by using iterative Fourier transformations back and forth between the two domains, the phase information of the complex field can be retrieved. Furthermore, it can be shown that the error between the intensity measurement and the

retrieved field converges [91].

One of the simplest phase retrieval method to implement is probably the Gerchberg-Saxton algorithm that consists of four steps:

1. Fourier transform an estimate of the near field (at the first iteration, we simply take the square-root of the intensity measurement),

2. replace the modulus of the resulting computed Fourier transform with the measured modulus of the far field (again, the square-root of the intensity measurement),

3. inverse Fourier transform this estimate of the far field,

4. replace the modulus of the resulting computed near field with the measured modulus to form a new estimate of the object.

Figure 4.15 shows a schematic of this algorithm, as well as an example of its convergence for a simulated beam. After a few hundreds iterations, the far field distribution is well reproduced as can be seen from the evolution of the far field pedestal.

By using this algorithm with the near field imaged at 35 m (figure 4.5), and the high dynamic range far field measurement (figure 4.10), we could retrieve a wavefront such that the RMS error of the calculated far field is 2.5×10^{-3} after 300 iterations, which takes about 10 seconds on a standard desktop computer. We observed that the error was not improving significantly, even after 100 000 iterations. The retrieved wavefront is shown in figure 4.16. The RMS and PTV wavefront amplitudes are respectively 0.15λ and 1.3λ, which leads to a Strehl ratio of 0.60, significantly worse than the results given by the wavefront sensor. Indeed, we notice that most of the wavefront deformations are contained in the bottom right part of the beam, similar to the observations on the measurement mask (figure 4.13). If the aperture of the retrieved wavefront is reduced to an approximate diameter of 70 mm, the amplitude is 0.06λ RMS and 0.55λ PTV. The Strehl ratio is then 0.87, which is closer to the measured values reported previously. Therefore, the phase retrieval algorithm tends to confirm the conclusion from the analysis of the mismatch between focal spot and direct wavefront measurement on the importance of correcting the full aperture laser beam.

Finally, we observe that the position of the higher wavefront amplitude corresponds to the extended wing of the far field, as can be seen in figure 4.10. Furthermore, the wings cover an area that is larger than the
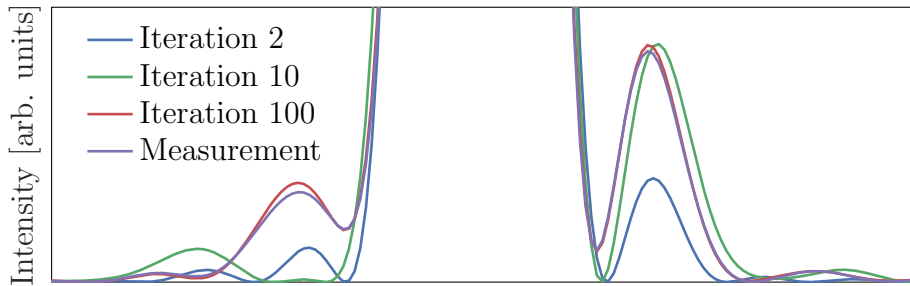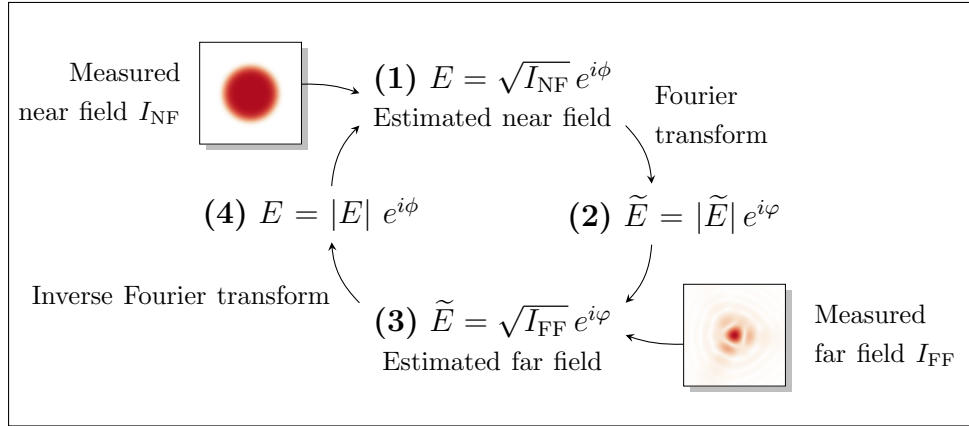
Figure 4.15: Schematic of the phase retrieval algorithm (top) with the four steps described, and example of the algorithm convergence (bottom) that shows the pedestal of the far field distribution at different iterations for a simulated beam (insets in the schematic). After 100 iterations, the retrieved field is very close to the measurement.

capillary aperture. It is thus relevant for the target lifetime to correlate the far field distribution to the degradation of the capillary.

4.5 Spatial contrast and target lifetime

During operation of the LUX experiment, we observed that the sapphire capillary target gets slowly larger to an extend such that the gas pressure is no longer sufficient to generate electrons (see P. Messner's thesis for more details on the LUX target [92]). The current design is a $500\,\mu\text{m}$ square capillary over a length of $10\,\text{mm}$ with 2 gas inlets at the bottom, and placed $2\,\text{mm}$ away from each end. The focal plane is positioned at the first inlet and the Rayleigh range is in the order of $3\,\text{mm}$ (see figure 3.14), such that the entrance of the capillary is still within the Rayleigh range.
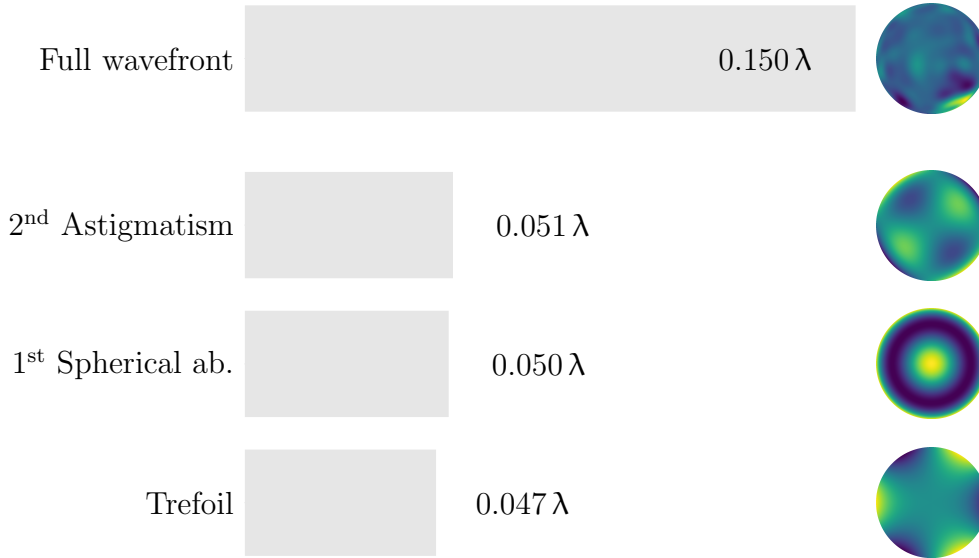
Figure 4.16: Retrieved wavefront from near and far field measurements using a phase retrieval algorithm. The RMS and peak-to-valley wavefront amplitudes are respectively 0.15λ and 1.3λ, which leads to a Strehl ratio of 0.60. Most of the wavefront deformations are contained in the bottom right part of the beam, which explains why many Zernike polynomials have a similar amplitude.

4.5.1   Characteristic damage of the target

In November 2017, the LUX beamline was operated for 24 consecutive hours, and a side view of the target was recorded every 5 minutes. Figure 4.17 shows the target profile at the beginning of the run, after 10 hours, and after 20 hours. We can see that the bottom edge of the capillary is damaged by the laser, such that after 20 hours, the entrance is 50 % larger. Furthermore, after 10 hours, only the first half of the target is widened. On the other hand, the top edge of the capillary stays identical. Therefore, the target degradation could be related to the extended wing at the bottom of the intensity distribution.

However, the standard z-scan does not have enough dynamic range to measure the evolution of this wing through the focus. Therefore, to reconstruct the intensity at the entrance plane of the target, we use the retrieved wavefront (see section 4.4) in order to accurately simulate the z-scan with a good dynamic range. Figure 4.18 shows the intensity profile in logarithmic scale for five planes around the focal plane. We see that
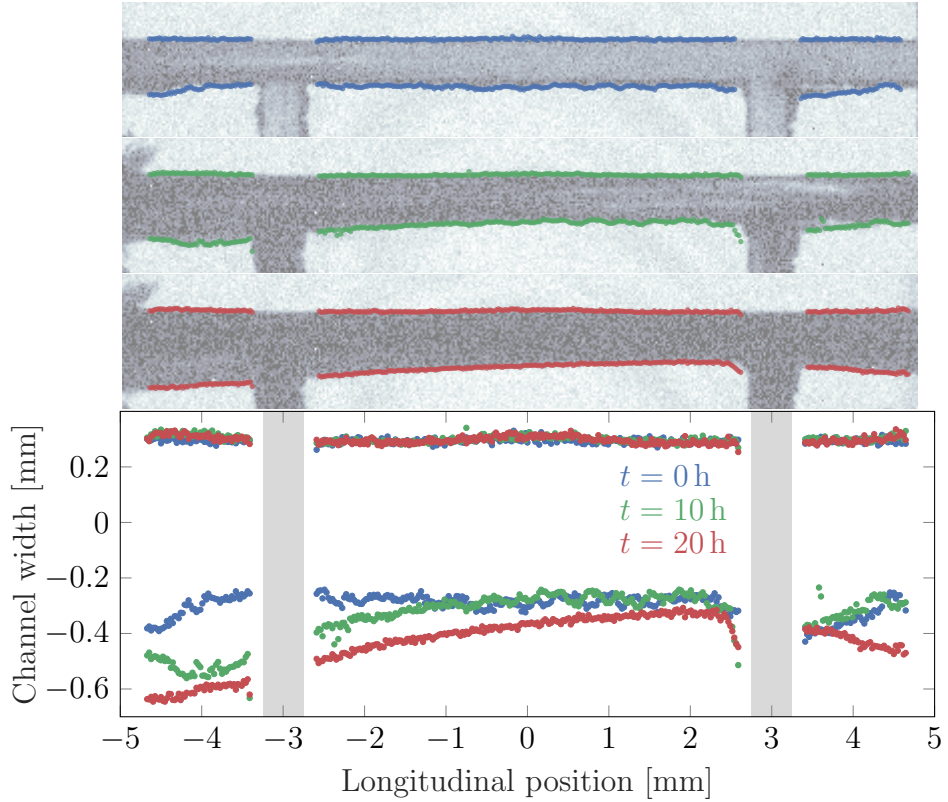
Figure 4.17: Capillary channel degradation during the 24 hours run. The pictures show a side view of the capillary at the beginning of the run (top, blue), after 10 hours (middle, green), and after 20 hours (bottom, red). The bottom plot shows the capillary dimensions retrieved from the camera images. The shaded area correspond to the inlets position.

the extended wing at the bottom is indeed present over a distance much larger than the Rayleigh length. Moreover, according to [93], the single-shot laser induced damage threshold (LIDT) for a femtosecond pulse on a non-polished sapphire plate is $5 \, \mathrm{J \, cm^{-2}}$. By comparing the maximum fluence and the mean fluence at the edge of the capillary, we see that the mean fluence is higher than twice the LIDT, and the maximum fluence is in excess of $100 \, \mathrm{J \, cm^{-2}}$, especially within this bottom wing. Furthermore, the wing extends to a distance larger than $600 \, \mathrm{\mu m}$ from the central spot, which corresponds to the characteristic size of the damage according to figure 4.17. Therefore, we can conclude that the edge of the wavefront—which is not corrected by the deformable mirror—is likely to be responsible for the degradation of the capillary target. This is reinforced from the fact that the focal spot drifted upwards during the 24 hours by $50 \, \mathrm{\mu m}$, and therefore away from the damaged edge.
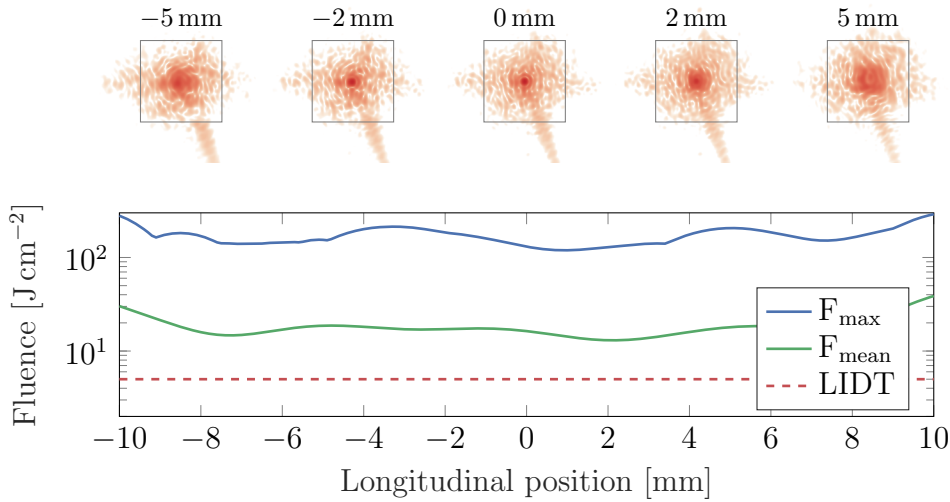
Figure 4.18: Fluence distribution around the focal spot plane (top). The logarithmic color scale only shows the fluence above the damage threshold of sapphire, and the gray box represents the capillary dimensions. The average and maximum fluence at the edge of the 500 μm capillary is plotted for a propagation distance of ± 10 mm around the focal plane (bottom). The damage threshold is indicated as a reference.

4.5.2 Workaround solutions

The solution to increase the target lifetime is of course to include the whole beam profile in the wavefront correction. However, a workaround solution would be to either remove the problematic area of the beam profile, or to increase the target dimensions. While this latter option can be troublesome to reach the needed pressure in the capillary, the first option is here considered.

Hard aperture

The easiest implementation is simply to reduce the aperture of the beam such that it does not include the edge of the near field. An iris such as the one installed before the compressor provides a tunable aperture as long as its material holds against the full power laser fluence. Figure 4.19 shows the logarithmic scale intensity pattern of the far field with the iris closed at a diameter of 70 mm, measured using the high dynamic range measurement described before. We can see that the problematic wing has indeed disappeared. However, the overall laser energy is decreased to 87 % due to the reduced aperture. Finally, while this hard aperture technique can already be used with the ANGUS laser, the diffraction from the iris
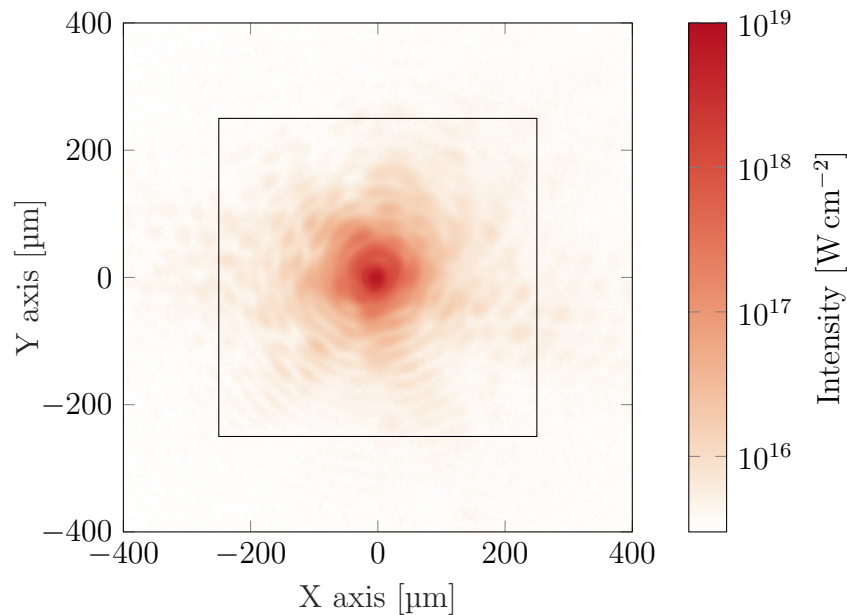
Figure 4.19: Far field intensity distribution in logarithmic scale with a 70 mm aperture before the compressor. The rectangle represents the capillary target dimensions. We notice the absence of the large wing present in the original far field due to the high wavefront amplitude at the edge of the beam profile.

should be considered and studied to ensure that it does not lead to a higher fluence on the optics such as the compressor gratings.

Gaussian mirror

Gaussian mirrors are designed to have a radially Gaussian or super-Gaussian shaped reflectivity. Therefore, by using such mirrors instead of the standard uniform high-reflectivity mirrors, it is possible to reflect only the center part of the beam, with a smooth edge that does not diffract like a hard aperture. Furthermore, by using such a mirror close to the focusing optic, it would help to reduce the position jitter of the beam on the parabola, and therefore limit the angular jitter of the focal spot. However, the maximum reflectivity of such a coating hardly goes above 90 % (according to Laser Components[2]) so the amount of such mirrors should be limited to avoid loosing too much pulse energy. Moreover, one should ensure that the coating is efficient for the whole laser bandwidth, and that its damage threshold allows it to be used with a high-power laser. Finally, as some energy will propagate

---

[2]www.lasercomponents.com

92

through the mirror, an efficient way to block or absorb the transmitted beam should be considered, as well as nonlinear effects.

Spatial filter

Finally, by spatially filtering the beam using a pinhole with a size similar to the target dimensions, the damage to the target can be drastically reduced. However, the spatial filter itself would then have to block the high intensity of the wings. An option to mitigate the intensity in the focal plane is to use two slits instead of one pinhole in combination with cylindrical or astigmatic lenses [94]. Furthermore, using long focal lengths would also reduce the intensity in the focal plane. However, in order to properly focus the beam through the spatial filter, the wavefront has to be mostly flat over the area that should go through the filter. Therefore, if the wavefront measured before the compressor (see figure 4.3) is due to a parabola misalignment, such a technique cannot be used as the focal spot would then be far too large for any efficient filter.

While using a wavefront sensor is critical for high power lasers in order to use an adaptive optics loop and to obtain a single-shot information, we have seen through this chapter that in order to obtain a high-quality focal spot, and to accurately use the Strehl ratio values computed from the measured wavefront, it is equally critical to ensure that the full beam aperture is measured. Furthermore, a non-ideal wavefront would not only decrease the usable energy which is contained in the main peak, but it also decreases the capillary target lifetime. Indeed, from the observation of the LUX target after more than 40 000 shots, the top edge is so far unaltered. Therefore, we believe that by improving the spatial contrast of the focal spot, the target could be conserved for several experiments over an extended period of time. As the current targets were damaged after a couple of days, it is however still difficult to quantify for how long such a statement would be valid.

Chapter 5

Heat-induced grating deformation

In the previous chapter, we investigated the quality of the focal spot for the LUX experiment, using the pre-target diagnostics, available only with a low power beam. For this purpose, the ANGUS beam is attenuated after the full amplification. Indeed, keeping the amplification identical in both operating modes also keeps thermal effects such as thermal lensing of the amplifiers [95] identical. Therefore, the low power beam has the same properties as the high power beam (apart from the energy obviously) and can be used to diagnose the laser before an experiment. However, if any change occurs due to the optics placed after the attenuator (see figure 3.1) while switching between low and high power, this diagnostic is no longer accurate and does not faithfully represent the high power laser parameters. The most critical elements susceptible to thermal effects are the two in-vacuum gold-coated compressor gratings. As the gold coating absorbs some of the incident laser energy (as will be shown later on), the grating substrate heats up. Then, the thermal expansion of the substrate material will deform the surface of the grating and thus change the reflected laser wavefront. The thermal expansion due to the absorbed laser energy is present for any optic, but its effects are strengthened for the gratings due to the vacuum environment that negates convective heat transfer, and to the gold coating that absorbs a much higher amount of laser energy compared to dielectric coatings commonly used for high-reflectivity mirrors.

We investigate the heat-induced grating deformation and its effects on the transient degradation of the laser wavefront to ensure that the focal spot quality measured previously is an accurate depiction of the high intensity transverse profile used in the LUX capillary target to generate electrons. We add that the lifetime of the target can be drastically shortened if the wavefront is degraded over time by the diffraction gratings. Quantifying this effect is therefore critical for a stable and reliable operation of the LUX experiment.

5.1 Increase of in-vacuum grating temperature

5.1.1 Absorption coefficient of gold

The absorption of gold can be estimated from the reflectivity based on the Fresnel equations. As the typical gold coating layer is thicker than the skin depth ($\delta_{800\,\mathrm{nm}} = 26\,\mathrm{nm}$ compared to a typical layer thickness $> 100\,\mathrm{nm}$), no energy is transmitted through it. Therefore, neglecting scattering, the absorbed energy is simply the incident energy minus the reflected energy. Using tabulated values of the complex index of refraction of gold [96, 97], we can calculate the reflectivity for an incidence angle of 51.4°, and deduce the absorption as a function of the wavelength (see figure 5.1). For the wavelengths of interest here (between 700 nm and 900 nm), the absorption of gold ranges from 3 % to 4.5 %. While these values are only estimates that neglect aspects such as scattering, they show that gold absorbs a few percents of near infrared light.
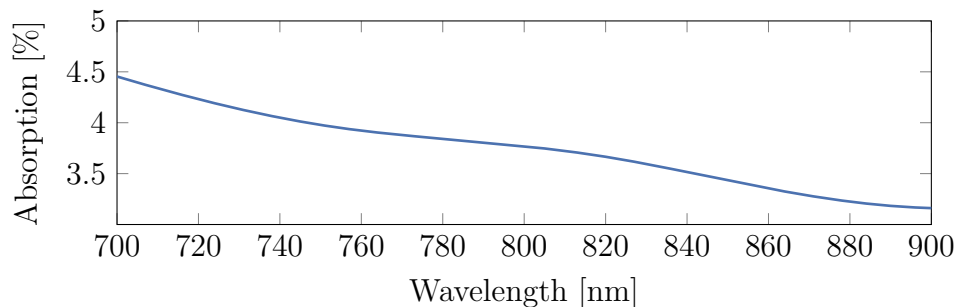
Figure 5.1: Absorption of gold as a function of the wavelength for an incidence angle of 51.4°, according to the Fresnel reflection calculated from the complex index of refraction.

Therefore, considering ANGUS parameters, the maximum average power absorbed by the first grating P_{abs} due to the first and fourth passes is given by:

$$P_{\mathrm{abs}} = E_{\mathrm{pulse}} \cdot f_{\mathrm{rep.\ rate}} \cdot \alpha_{\mathrm{Au}} \cdot \left(1 + \eta_d^3\right) = 2.0\,\mathrm{W}, \tag{5.1}$$

with $E_{\mathrm{pulse}} = 6\,\mathrm{J}$ the pulse energy, $f_{\mathrm{rep.\ rate}} = 5\,\mathrm{Hz}$ the repetition rate, $\alpha_{\mathrm{Au}} = 3.76\,\%$ the average absorption coefficient over the laser bandwidth and $\eta_d = 0.92$ the grating diffraction efficiency raised to the power of 3 to account for the energy loss of the first three passes. The absorbed average power on the second grating only differs from the first grating by less than 1 %.

96

5.1.2 Grating temperature measurement

Using a thermal camera sensitive to the wavelengths from 7.5 µm to 14 µm through a ZnSe vacuum window, we can monitor remotely the temperature of the first grating (as represented in figure 5.2). Figure 5.3 shows the evolution of the maximum temperature measured with the thermal camera while the laser was sent in the compressor during 4 hours with an average power of 30 W (6 J at 5 Hz). The camera continued to record the temperature for about 60 hours after the laser was turned off.
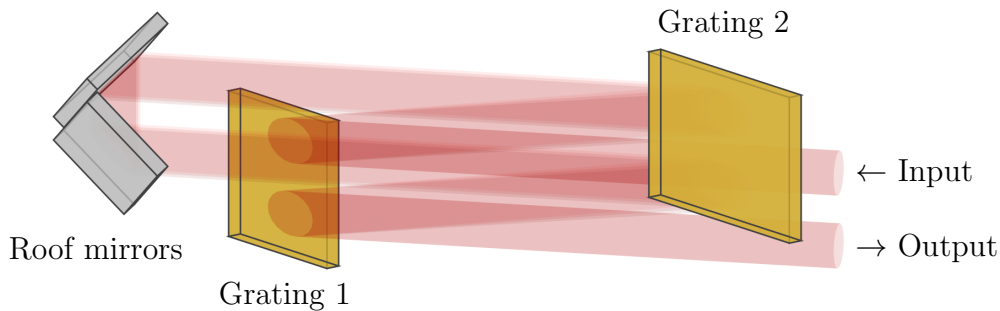
Figure 5.2: 3D model of the compressor optics, viewed from thermal camera. The camera is below the incidence plane of the gratings and is pointed at the 1st grating.

We observe that the time necessary for the grating to cool down to room temperature is very long: the half-time of the temperature exponential decrease is 7 hours. This long half-time explains why the temperature at the beginning of the run is already at 25 °C. We first had an 8 hour run which brought the grating temperature to 32 °C. The grating then cooled down over night to 25 °C when we started the next run reported here. Furthermore, while the laser heats the grating, the temperature increases linearly, with a rate of 3.2 °C/h. In fact, as the grating is in contact with the optomechanics only via small nylon-tipped screws (two are visible in the picture in figure 5.3 as white thin disks above the grating) that have a low thermal conductivity of 0.25 W/(m K), it can mainly be cooled through thermal radiation, which usually has a rather poor efficiency. Therefore, the heat transfered by the laser stays in the substrate and needs several hours until it can be radiated towards the environment. As the emissivity of gold is very low—down to 0.01 [40]—, only the heat radiated from the side of the substrate is visible. We also notice that the mount itself stays at room
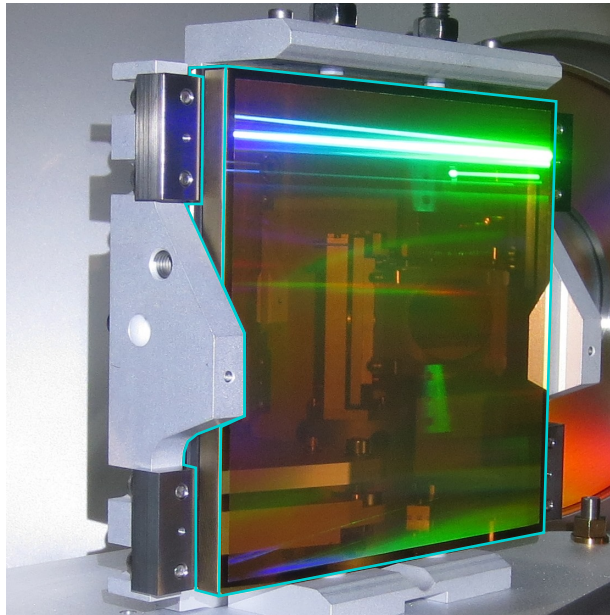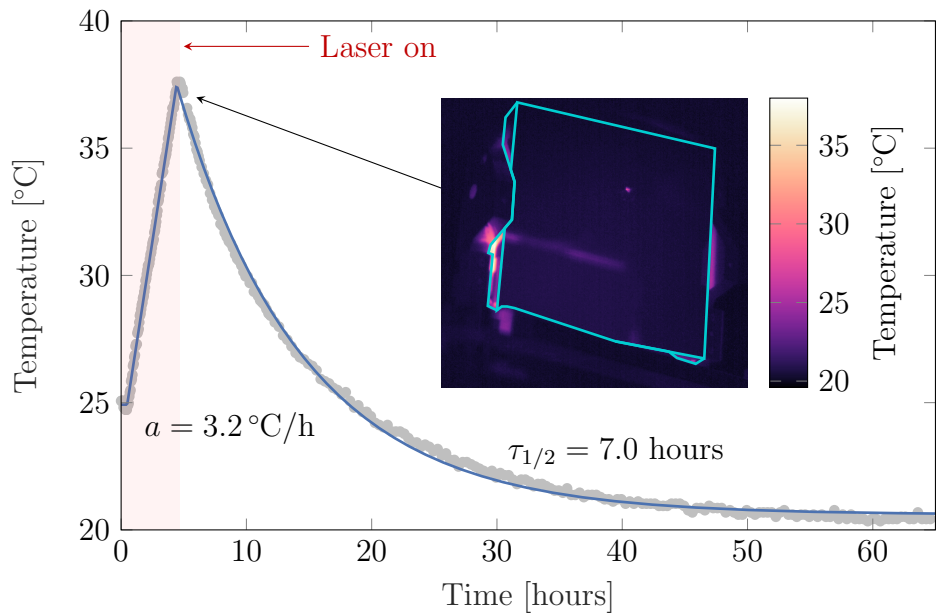
Figure 5.3: Evolution of the grating substrate temperature with 30 W average input power (top). The laser was sent during 4 hours, and the temperature measured over several days afterwards. The data (gray dots) is fitted (blue line) by a linear increase $a = 3.2\,°\mathrm{C/h}$ followed by an exponential decay with a half-time $\tau_{1/2} = 7.0$ hours. The inset shows the thermal camera image at the end of the run. A picture of the grating (bottom) shows that the measured heat comes from the side of the substrate. The turquoise line indicates the visible edges of the grating substrate for both pictures.

temperature, but seems to reflect the heat radiated from the glass substrate as visible on the trapezoidal pieces on each sides of the grating. Both the reflections and the temperature of the mount indicate a low emissivity of the material.

5.1.3 Modeling the grating temperature

Model description

We can model the grating substrate temperature by listing the heat transfers from and to the grating, and considering the laser as a source term defined by the absorbed power described above. As the grating has very little contact to the mount, and only through plastic surfaces, we ignore the temperature decrease due to conduction. However, we do include the temperature of the mount in the model, in order to consider its effect on the thermal radiation of the grating substrate. Therefore, the heat transfers considered are the following:

- radiation from the grating gold coated and uncoated surfaces to the compressor chamber,

- radiation between the grating and the mount,

- radiation from the mount to the compressor chamber,

- and the laser itself as a source term.

We assume that the compressor chamber is kept by the air conditioning to a stable temperature of $T_0 = 20\,°\text{C}$ and that it acts as a perfect black body. Furthermore, the grating and mount surfaces are considered opaque and diffuse, which means that the thermal radiation is not transmitted through these surfaces but either absorbed or reflected, and independent of direction.

The heat transfer $Q_{1 \to 2}$ between two parallel plates through a surface A considering the multiple absorptions and reflections is given by:

$$\frac{d\,Q_{1\to2}}{dt} = \sigma A \frac{\varepsilon_1 \varepsilon_2}{\varepsilon_1 + \varepsilon_2 - \varepsilon_1 \varepsilon_2} \left(T_1^4 - T_2^4\right) = \sigma A\,\varepsilon_{1-2}\left(T_1^4 - T_2^4\right), \qquad (5.2)$$

with ε_i and T_i the emissivity and temperature of the body i, and σ the Stefan-Boltzmann constant. We define ε_{1-2} the effective emissivity between two bodies for bookkeeping such that:

$$\varepsilon_{1-2} = \frac{\varepsilon_1 \varepsilon_2}{\varepsilon_1 + \varepsilon_2 - \varepsilon_1 \varepsilon_2}. \qquad (5.3)$$

If the body 2 is black ($\varepsilon_2 = 1$), we obtain $\varepsilon_{1-2} = \varepsilon_1$ and equation 5.2 gives the total power radiated by body 1 through the surface A as described by the Stefan-Boltzmann law.

Furthermore, the temperature of a system is linked to the heat transfer through the heat capacity C:

$$C = \frac{\delta Q}{dT}, \tag{5.4}$$

with dT the variation of temperature due to the transfered heat δQ. The heat capacity is an extensive property and is usually specified as a specific heat capacity $c = C/(\rho V)$ in $\mathrm{J\,kg^{-1}\,K^{-1}}$, with ρ and V the density and volume of the body considered.

Combining equations 5.2 and 5.4, we can establish two differential equations for the grating substrate and the mount. The subscript 0 refers to the vacuum chamber, 1 to the grating substrate, Au to the gold coating and 2 to the grating mount. We obtain for the grating substrate temperature T_1:

$$C_1 \frac{dT_1}{dt} = \sigma \underbrace{(\overbrace{\varepsilon_1 \, A_{1-0}}^{\text{edges}} + \overbrace{\varepsilon_{\mathrm{Au}} \, A_{\mathrm{Au}}}^{\text{front}}) \cdot \left(T_0^4 - T_1^4 \right)}_{\text{chamber}}$$
$$+ \ \sigma \underbrace{\varepsilon_{1-2} \, A_{1-2} \cdot \left(T_2^4 - T_1^4 \right)}_{\text{edges \& back – mount}} + \ \underbrace{P_{\mathrm{abs}}}_{\text{source}}, \tag{5.5}$$

with $C_1 = 3.4 \times 10^3 \ \mathrm{J\,K^{-1}}$ the heat capacity of the grating, σ the Stefan-Boltzmann constant, $\varepsilon_1 \simeq 0.73$ the emissivity of the glass with a frosted surface, A_{1-0} the grating substrate surface that does not face the aluminium mount, $\varepsilon_{\mathrm{Au}}$ the emissivity of the gold coating [40], A_{Au} the surface of the gold coating, ε_{1-2} the effective emissivity between the glass substrate and the mount, A_{1-2} the grating substrate surface that does face the mount, and P_{abs} the laser power absorbed by the grating. Similarly for the grating mount temperature T_2, we have:

$$C_2 \frac{dT_2}{dt} = \sigma \underbrace{\varepsilon_2 \, A_{2-0} \left(T_0^4 - T_2^4 \right)}_{\text{mount – chamber}} - \sigma \underbrace{\varepsilon_{1-2} \, A_{1-2} \left(T_2^4 - T_1^4 \right)}_{\text{mount – grating}}, \tag{5.6}$$

with $C_2 \simeq 5.2 \times 10^3 \ \mathrm{J\,K^{-1}}$ the heat capacity of the aluminium mount, $\varepsilon_2 \simeq 0.17$ the emissivity of rough aluminium, and A_{2-0} the surface of the mount facing the vacuum chamber. Due to the temperatures raised to the power of 4, an analytical solution is difficult—if possible—to calculate and not within

the scope of this work. However, as it only involves a single time derivative of the first order for each equation, it can be easily solved numerically using a very simple explicit finite difference method such that:

$$\frac{dT_i}{dt} \equiv \frac{T_i[k+1] - T_i[k]}{\Delta t}, \tag{5.7}$$

with $T_i[k]$ the discrete temperature at the iteration k, and Δt a constant time step. Therefore, the equations 5.5 and 5.6 can be easily computed by:

$$T_i[k+1] = T_i[k] + f_i\left(T_1[k],\ T_2[k]\right) \cdot \Delta t, \tag{5.8}$$

with f_i the appropriate function given by the equations 5.5 and 5.6. We can then iteratively calculate the evolution of the temperature of both the mount and the grating.

Comparison to measured data

Figure 5.4 compares this model to the grating temperature measured during an experiment campaign where several input laser energy where scanned from 0.6 J to 6.0 J. The second half of the data is identical to the data reported in figure 5.3. The modeled temperature of the grating agrees well with the measurement, including both the increase due to the laser beam and the cooling of the substrate when no laser is present in the vacuum chamber. Furthermore, we notice that if the mount is ignored from the model, the calculated temperature differs heavily in intensity and behavior from the measurement. Indeed, the back of the grating is facing the mount, which has a low emissivity and therefore absorption coefficient. Thus, a significant area of the total grating surface has a poor radiative cooling.

However, the simulation only agrees with the data if near field enhancement is considered. Indeed, according to Wang *et al.* [45], the grooves of the gold-coated grating enhance the amplitude of the electric field on the grating surface. Therefore, the fluence amplitude that should be considered to calculate the absorbed energy by the grating surface is about twice the incident fluence. The exact value of the near field enhancement factor depends on the grating groove shape as well [43]. Thus, in the equation 5.1, an additional factor of 2 is added to include the near field enhancement:

$$P_{\text{abs}} = 2\,E_{\text{pulse}} \cdot f_{\text{rep. rate}} \cdot \varepsilon_{\text{Au}} \cdot \left(1 + \eta_d^3\right). \tag{5.9}$$

Once this factor is included in the model, the RMS error between the measured data and the prediction is 0.75 %. We can further estimate the

2nd grating temperature using the same model but adjusting the absorbed power and the dimensions of the grating. We find out that the 2nd grating temperature is up to 10 % lower than the 1st grating. As it has a larger surface—40 % wider than the 1st grating—it emits more radiation and is therefore more efficient at evacuating heat from the substrate. Moreover, the incident power is 1 % lower than for the 1st grating due to the diffraction efficiency.
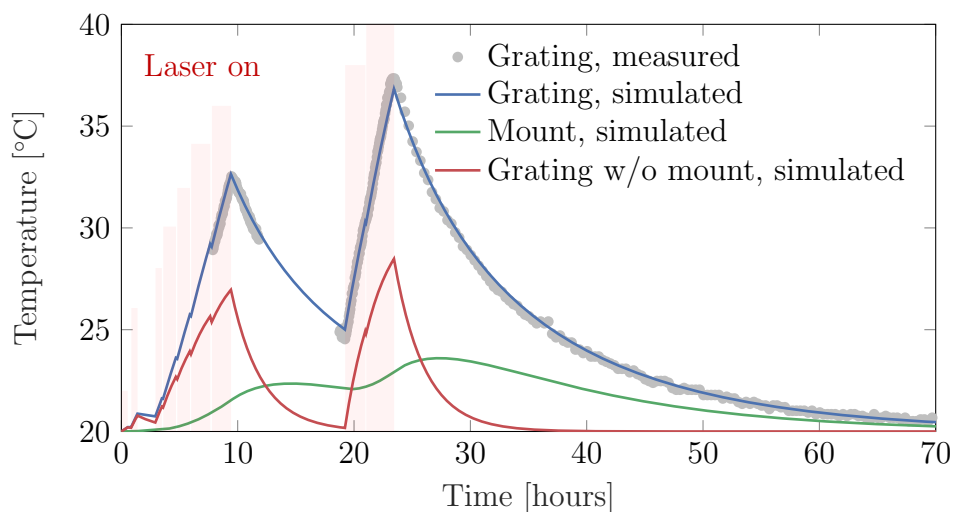
Figure 5.4: Grating temperature during an experiment campaign where several input laser energy where scanned from 0.6 J to 6.0 J. The grating temperature was measured (gray dots) only for the last three settings and for several days afterwards, as reported in figure 5.3. The model (blue line) agrees well with the measured temperature with a mean RMS error below 1 %. The temperature of the mount is reported as well (green line). The grating temperature calculated while ignoring the mount (red line) shows a severe mismatch with the data, and hence strengthens the necessity of including the optomechanics in the model. The red shaded areas are scaled according to the input laser energy.

Equilibrium temperature

Apart from estimating the grating temperature during operation, we can use the model to predict the steady-state temperature of the grating, as well as the time when this equilibrium is reached. These predictions are reported in figure 5.5 in function of the laser input power. We see that the equilibrium temperature evolves quasi-linearly with a slope of 1.16 °C/W. Furthermore, above a 5 W laser input power, the time necessary to reach

99 % of this temperature is between 40 to 45 hours. In particular for the ANGUS nominal average power of 30 W, the equilibrium temperature is 58.7 °C and it is reached after $\tau_{99\%} = 43$ h. The mount temperature also increases and reaches 33.4 °C for the same laser parameters.
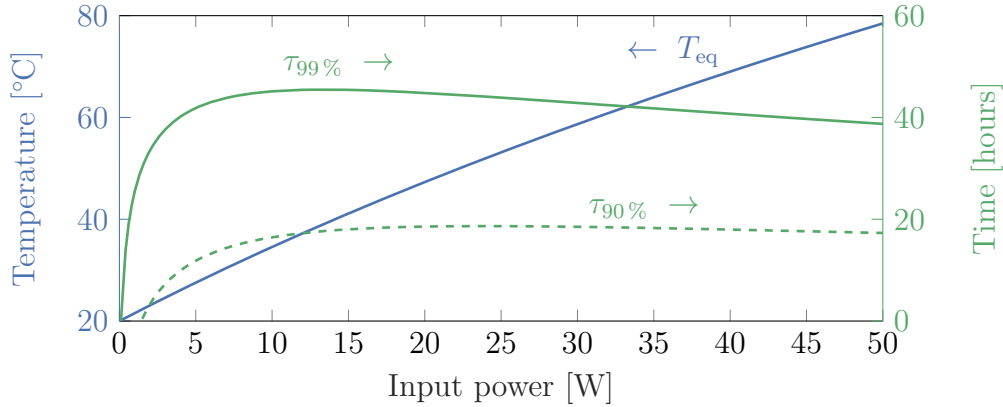
Figure 5.5: Steady-state temperature T_{eq} (blue) of the grating and time necessary to reach 90 % and 99 % of this steady-state temperature (respectively dashed and solid green) in function of the laser input power.

From this model, we conclude that the gratings can be safely operated for a long time as the steaty-state temperature is below the melting temperature of the gold coating ($T_{\mathrm{m}} = 1064$ °C) or the glass-transition temperature of either Pyrex, fused silica, or photoresists such as SU-8 ($T_{\mathrm{g,\ Pyrex}} = 500$ °C, $T_{\mathrm{g,\ fused\ silica}} = 1200$ °C, and $T_{\mathrm{g,\ SU\text{-}8}} > 200$ °C [98]). However, as more than 40 hours of constant laser operation are necessary to reach this state, it is not practical to rely on this regime. Therefore, the gratings have to be operated in a transient state where their temperature is increasing.

Finally, we note that this model assumes a homogeneous temperature of the grating. However, the mechanism for energy absorption of femtosecond pulses can be described by the two-temperature model [99]. Using this model, one can calculate the surface temperature at the time scale of the laser pulse. Extrapolating Wang *et al.* calculations [45], the surface temperature 30 ps after the pulse would be 216 °C for an input fluence of $100 \,\mathrm{mJ\,cm^{-2}}$, which corresponds to an energy of 6 J for ANGUS beam size. Therefore, the temperature distribution is not reconstructed at the scale of the pulse duration by our simple radiative model.

On the other hand, one can estimate the characteristic time of the heat diffusion through the substrate t_c from Fourier's law [100]:

$$t_c = \frac{L_c^2}{4\alpha},$$ (5.10)

with L_c a characteristic length of the substrate, and α the thermal diffusivity (see table 5.1 below). Using the grating thickness as the characteristic length, we obtain a characteristic time of 22 minutes for a Pyrex substrate and 12 minutes for a fused silica substrate. Thus, for time scales of several hours or days, the heat absorbed at the surface has diffused through the grating and we can then neglect the local heat distribution for an initial estimate on the grating temperature.

An important conclusion of the measurements and the simulation is that the temperature of the grating is constantly increasing while the compressor is used with an input power higher than a few watts. Therefore, as the heat deforms the grating through thermal expansion, the wavefront of the reflected beam will be degraded as well.

5.2   Output wavefront measurement

As explained in the previous section, a fraction of the laser energy incident on the gratings is absorbed and increases the temperature of the grating substrate. It deforms the grating surface due to thermal expansion and thus deforms the reflected laser wavefront. Moreover, as the beam is spatially dispersed after the first pass, the changes of the wavefront can couple into the temporal properties of the pulse and be detrimental to the overall compression [101]. The deformation of the laser wavefront has a direct negative impact on the laser focusability of the beam, which heavily decreases the available peak intensity as well as the energy contained within the central part of the focal spot.

Previous work has reported this issue at different pulse energies [102, 103, 104] and proposed solutions to mitigate or compensate the thermal expansion. Fourmaux *et al.* [103] propose to adjust the position of the off-axis parabola to compensate the defocusing of the 110 mJ 100 Hz laser used. On the contrary, Alessi *et al.* [104] tackle the source of the problem by actively cooling the grating substrate to efficiently extract heat and therefore reduce the surface deformation for a PW-class grating compressor, measured using a diode array with equivalent average power. We propose to

directly measure the heat-induced distortion in gold-coated gratings of our 100 TW class vacuum compressor using the actual high-energy ultrashort laser to both heat up the gratings and diagnose their deformations. The observed deformations could therefore be used to predict the grating behavior during an experiment without relying on assumptions on the influence of vacuum, beam size or pulse duration for instance. We reported these measurements in Optics Express in May 2018 [105].

5.2.1 Experimental setup

In order to measure the influence of the input power on the compressor output wavefront, we scan both the pulse energy and the laser repetition rate. Using the thin film polarizer based attenuator, we tune the energy from 0.6 J to 6.0 J at the compressor entrance. Considering the projected beam area on the grating of $S_{\text{proj.}} = 62\,\text{cm}^2$, it corresponds to average fluences ranging from approximately $10\,\text{mJ}\,\text{cm}^{-2}$ to $100\,\text{mJ}\,\text{cm}^{-2}$. For each energy step, the laser was run for a duration of 30 minutes for the low energy steps, up to 90 minutes for the high energy steps. Additionally, after selected tests, the laser energy was tuned down to 150 mJ for 20 minutes to measure the cooling behavior of the gratings while still being able to measure the laser parameters. The repetition rate was scanned by changing the laser internal trigger to allow only every other or every third pulse to be sent to the multipass power amplifiers. We therefore scanned the repetition rates of 0.5 Hz, 1.0 Hz, 1.67 Hz, 2.5 Hz, and 5.0 Hz.

To monitor the laser parameters, the pre-compressor and post-compressor diagnostics are used (see sections 3.4.1 and 3.4.2). The wavefront is measured after the compressor using a four-wave lateral shearing interferometer wavefront sensor [60]. The post-compressor diagnostics have inherent astigmatism as already explained, therefore the wavefront measurements presented in the following sections show relative results. This has the advantage of ignoring the aberrations of the setup and the laser itself, and only focus on the transient deformations of the optics. Thanks to these diagnostics, we can ensure that the laser beam does not change before the compressor and thus rely on the post-compressor diagnostics. All the data reported here was acquired for every individual shot.

As the full energy of the ANGUS laser was used, the compressor was operated at a pressure below $10^{-6}\,\text{mbar}$, the quality of the vacuum was continuously monitored by a residual gas analyzer to ensure that no contamination could disturb the experiment by increasing the absorption or

lowering the damage threshold of the gratings. We measure the quality of the vacuum by ensuring that the partial pressure of masses above 45 u is less than 10^{-3} of the total pressure [106]. The data was saved and archived into the control system and post-analysis revealed that the vacuum environment did not change during the experiment. The full power laser beam was then sent through the transport beamline towards the LUX experimental area to be dumped, as only a fraction is sampled for the post-compressor diagnostics. Therefore, the parameter scans reported here are done in realistic conditions: the vacuum system, the laser beam size, energy, and pulse duration are similar to those used for the LUX experiment and thus reflect the actual behavior of the grating compressor during everyday operation.

5.2.2 Effects on the laser divergence

We first investigate the change of the beam divergence as it directly relates to a shift of the longitudinal focus position. The impact of the input beam fluence in the grating plane is studied at a fixed repetition rate of 5 Hz, and then the repetition rate is varied while the fluence is set to a fixed value of $50 \, \mathrm{mJ \, cm^{-2}}$.

Energy scan

Figure 5.6 shows the relative change of the beam divergence over time in the horizontal (top) and vertical plane (bottom) for five fluence steps measured with the wavefront sensor, which correspond to input energies ranging from 0.6 J to 4.2 J. A clear positive correlation between the input fluence and the increase of divergence can be observed. As expected, as more energy is absorbed by the substrate, the higher thermal load leads to a higher deformation of the grating surface. Moreover, the horizontal divergence increases at a much higher rate than the vertical divergence, leading to an increase of astigmatism of the beam. Furthermore, the horizontal divergence seems to keep increasing linearly after an exponential growth while the vertical divergence saturates or even decreases after a similar exponential behavior.

The temporal evolution of the beam divergence is fitted with the sum of an exponential increase and a linear curve $f(t) = a(1 - \exp(-t/\tau)) + bt$, based on the observed pattern. All fits show a very good agreement with the measured data and we could then retrieve two time constants: the exponential time constant τ and a linear growth rate b which are plotted in figure 5.7. While the exponential time constant increases similarly in both

Figure 5.6: Evolution of the laser beam horizontal (top) and vertical (bottom) relative divergence measured after the grating compressor for different fluence level from $10\,\mathrm{mJ\,cm^{-2}}$ to $70\,\mathrm{mJ\,cm^{-2}}$ at a repetition rate of $5\,\mathrm{Hz}$. The data (gray dots) is overlaid by a fit (colored solid line) in a good agreement with the measurements.

Figure 5.7: Exponential constant (left) and linear growth rate (right) of the fitted curves (solid lines on Figure 5.6) for the different measured input fluences in the horizontal (blue circles) and vertical (green squares) planes. A linear fit (solid line) highlights the behavior of the scan.

107

planes with the input fluence, the linear growth rate is only significant in the horizontal plane. The horizontal divergence does not show saturation for higher input fluences.

In an attempt to reach such a regime, an additional 4 hour run was measured with an input energy of 6 J at 5 Hz (see figure 5.8). After the exponential growth happening in the first 10 to 20 minutes, the horizontal divergence increases quasi-linearly for two hours before saturating around 190 µrad. In the last two hours of the run, it then decreased with a rate on the order of 10 µrad/h. The vertical divergence, on the other hand, was linearly increasing with a rate of 3 µrad/h after the exponential growth. It should be noted that the grating used for this run had a heightened absorption of the incident laser energy due to a damage of the coating. The absolute value of the divergence and the time constants reported here is then higher than for an undamaged grating.
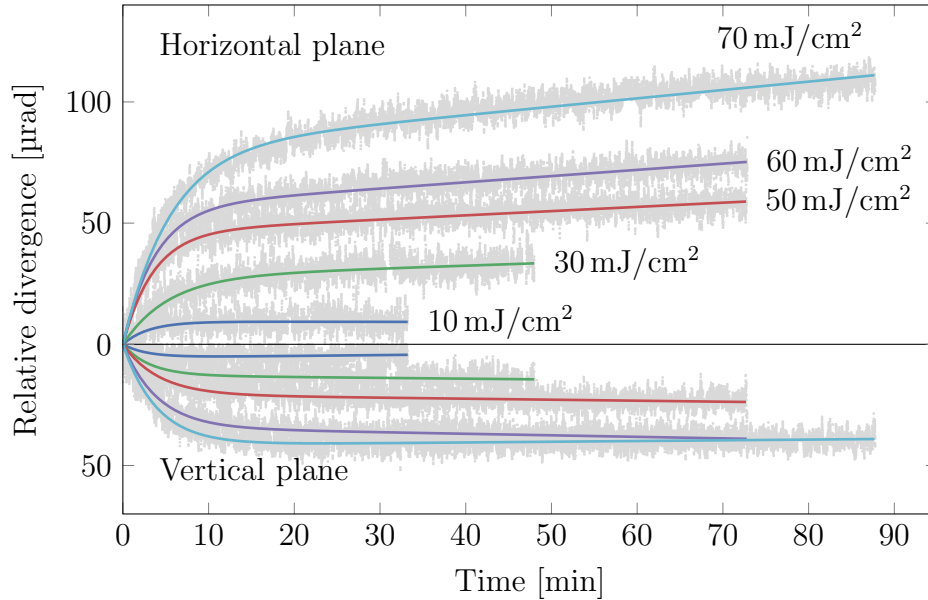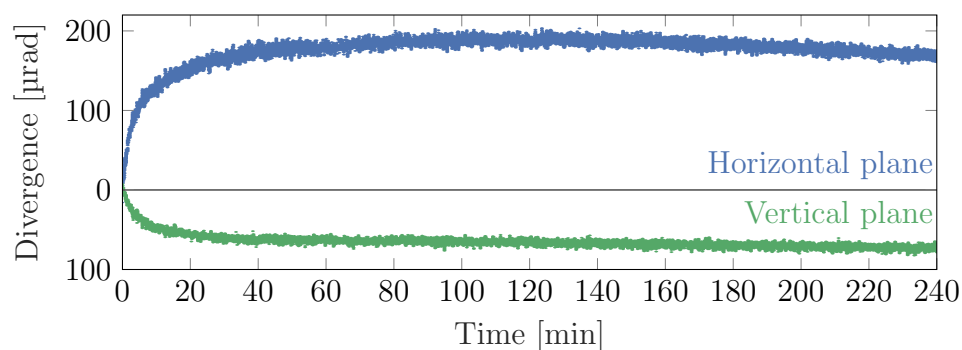

Figure 5.8: Evolution of the laser beam horizontal (top, blue) and vertical (bottom, green) relative divergence measured after the grating compressor for a 30 W average power (6 J at 5 Hz).

Nevertheless, a possible explanation of such an asymmetric behavior between horizontal and vertical divergence could be the dispersion of the beam on the second grating. Indeed, as the surface of the second grating is altered and the beam is horizontally dispersed, an additional angular chirp would be imprinted on the beam. However, this angular chirp would be seen by the wavefront sensor as an increase in divergence but only in the horizontal plane, which could explain the larger measured divergence.

One can also notice on figure 5.6 that the increase in divergence between two different energy levels is not constant. This can be explained by

a drawback in our experimental procedure. Due to the amount of laser time required, the data sets presented here were acquired over the course of several days. Therefore, the time between two runs has not always been long enough to allow the gratings temperature to go back to the initial temperature of 20 °C, as can be seen in the quasi-continuous rise of the temperature in figure 5.4 for the first day of experiment. Thus, the exponential curve on figure 5.6 would start with a higher offset which is not visible in these results showing only the relative changes during a run.

Finally, we report that for the three highest input fluence levels, we observed a deterioration of the first grating coating, which most likely increased the absorbed laser energy by the grating. Thus, the results at a repetition rate lower than 5 Hz or an input energy higher than 80 mJ cm^{-2} have been measured on the deteriorated coating. While it affects the amplitude of the wavefront deformations, the overall trends reported here would stay valid as long as the coating quality stays identical for a given set of measurements.

Repetition rate scan

The repetition rate has a direct influence on the divergence evolution as can be seen on figure 5.9, where it is varied from 1 Hz to 5 Hz at a constant input fluence of 50 mJ cm^{-2}.

As the repetition rate increases at a constant input energy, the average power and thus the heat absorbed by the gratings increases as well. Therefore, the thermal expansion deforms more and more the substrate. Furthermore, by fitting the curves with the same function described in the energy scan analysis, we observe that the linear growth rate of both the horizontal and vertical divergences is increasing with the repetition rate (see figure 5.10). However, a clear behavior cannot be extracted from the exponential constant, due to the low number of data points. Indeed, as the repetition rate is changed by rejecting a given number of pulses, we could not access repetition rates between 2.5 Hz and 5 Hz.

We observed that the heat-induced deformation of the gratings leads to an important increase of the divergence and astigmatism due to the asymmetry in the vertical and horizontal planes. Therefore, it appears necessary to investigate the evolution of the focal spot quality.
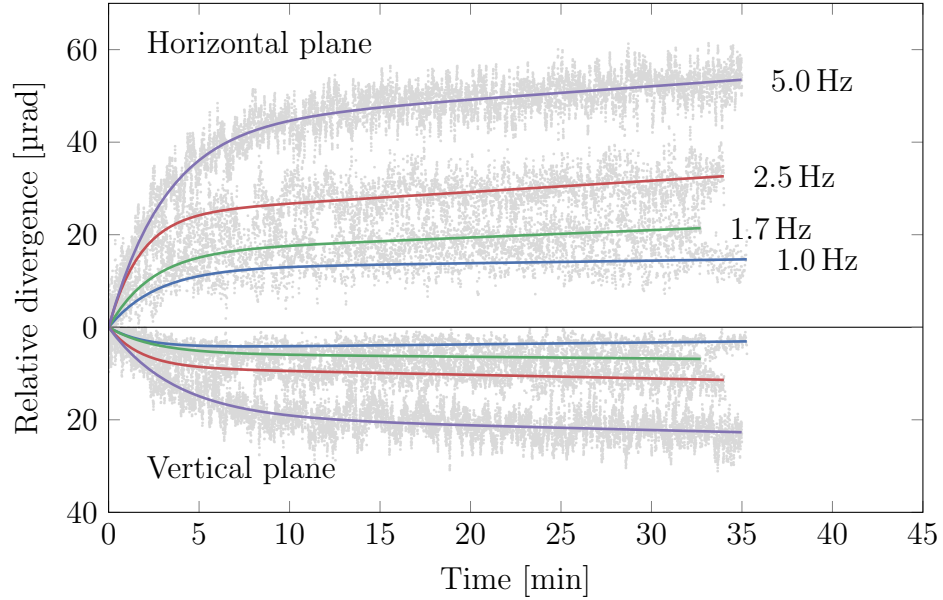
Figure 5.9: Evolution of the laser beam horizontal (top) and vertical (bottom) relative divergence measured after the grating compressor for different repetition rates from 1 Hz to 5 Hz at a fluence of $50\,\mathrm{mJ\,cm^{-2}}$. The data (gray dots) is again overlaid by a fit (colored solid line).
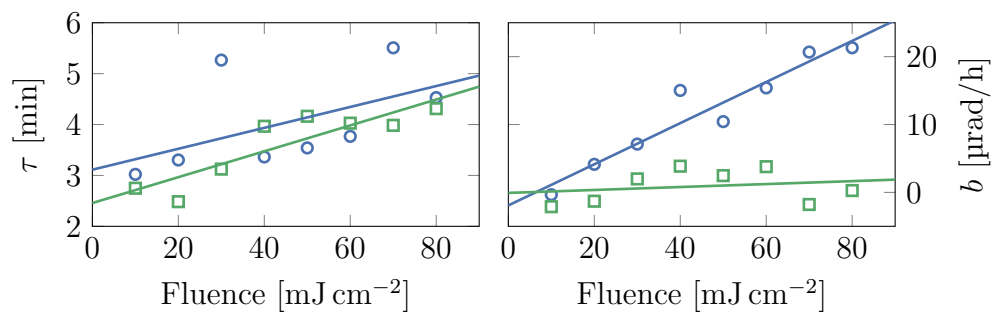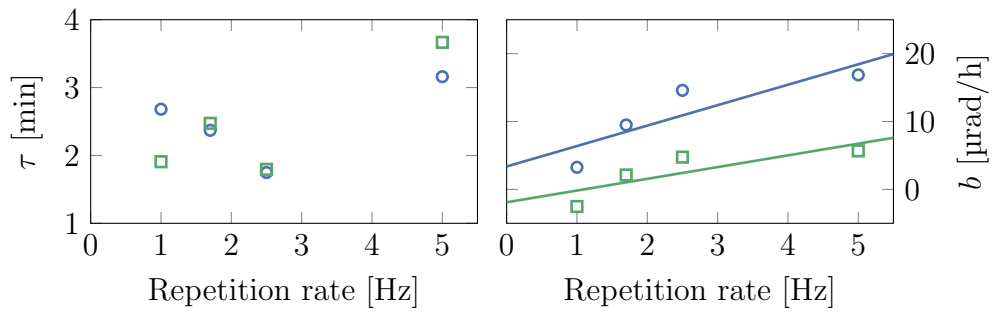

Figure 5.10: Exponential constant (left) and linear growth rate (right) of the fitted curves (solid lines on Figure 5.9) for the different repetition rates in the horizontal (blue circles) and vertical (green squares) planes. A linear fit (solid line) highlights the behavior of the scan, as previously shown.

5.2.3 Effects on the beam focusability

Using the wavefront sensor, we monitor the evolution of the relative RMS amplitude of the wavefront as well as the relative Strehl ratio, calculated from the point spread function (PSF) using the measured wavefront map. The tilts and the defocus are excluded from the analysis in order to restrict the observations to the quality of the focal spot rather than its longitudinal or transverse position. While the relative Strehl ratio does not indicate the quality of the laser beam directly, it captures the change of its focusability due to the deformation of the grating surface.

Figure 5.11 shows these two measurements for three different input fluences at $5\,\text{Hz}$. At $10\,\text{mJ}\,\text{cm}^{-2}$, the wavefront and the Strehl ratio stay almost constant to an average value of $0.05\,\lambda$ and 0.9 respectively. Over 30 minutes, the wavefront amplitude increases by $0.01\,\lambda$ and the Strehl ratio decreases by 0.05. At $50\,\text{mJ}\,\text{cm}^{-2}$ and $80\,\text{mJ}\,\text{cm}^{-2}$, we observe a behavior similar to the divergence evolution: after an exponential growth of the wavefront deformations with a time constant of about 5 minutes, they increase linearly. Especially for the $80\,\text{mJ}\,\text{cm}^{-2}$ case, which is close to the designed operating parameters of the compressor, the Strehl ratio is reduced to 0.5 in less than 2 minutes and to 0.16 after 10 minutes. This fast degradation of the laser beam spatial quality heavily reduces its usability as a driver for experiments relying on parameter scans.

Seeing how fast the wavefront degrades due to the gratings surface deformation, it is also of interest to investigate how long the gratings need to recover their initial shape. Thus, after a 90 minutes run at a fluence of $80\,\text{mJ}\,\text{cm}^{-2}$ at $5\,\text{Hz}$, the laser energy was decreased to $150\,\text{mJ}$ for 30 minutes in order to significantly reduce the absorbed power but still be able to measure the wavefront deformations (see figure 5.12). After 15 minutes, the Strehl ratio reaches the 0.5 level, and according to the exponential plus linear fit, it would reach the 0.9 level after 50 minutes as the linear slope corresponds to an improvement of $80\,\%/\text{h}$. These results coincide with the long half-time of the grating substrate temperature decrease reported in section 5.1.2.

However, the wavefront changes significantly in only a few minutes after the input laser energy is reduced. Therefore, a mitigation of the reported degradations using a deformable mirror can only be operated while the full power laser beam is heating the gratings. Such an online adaptive optics loop can be practically difficult as one need to ensure that the beam is
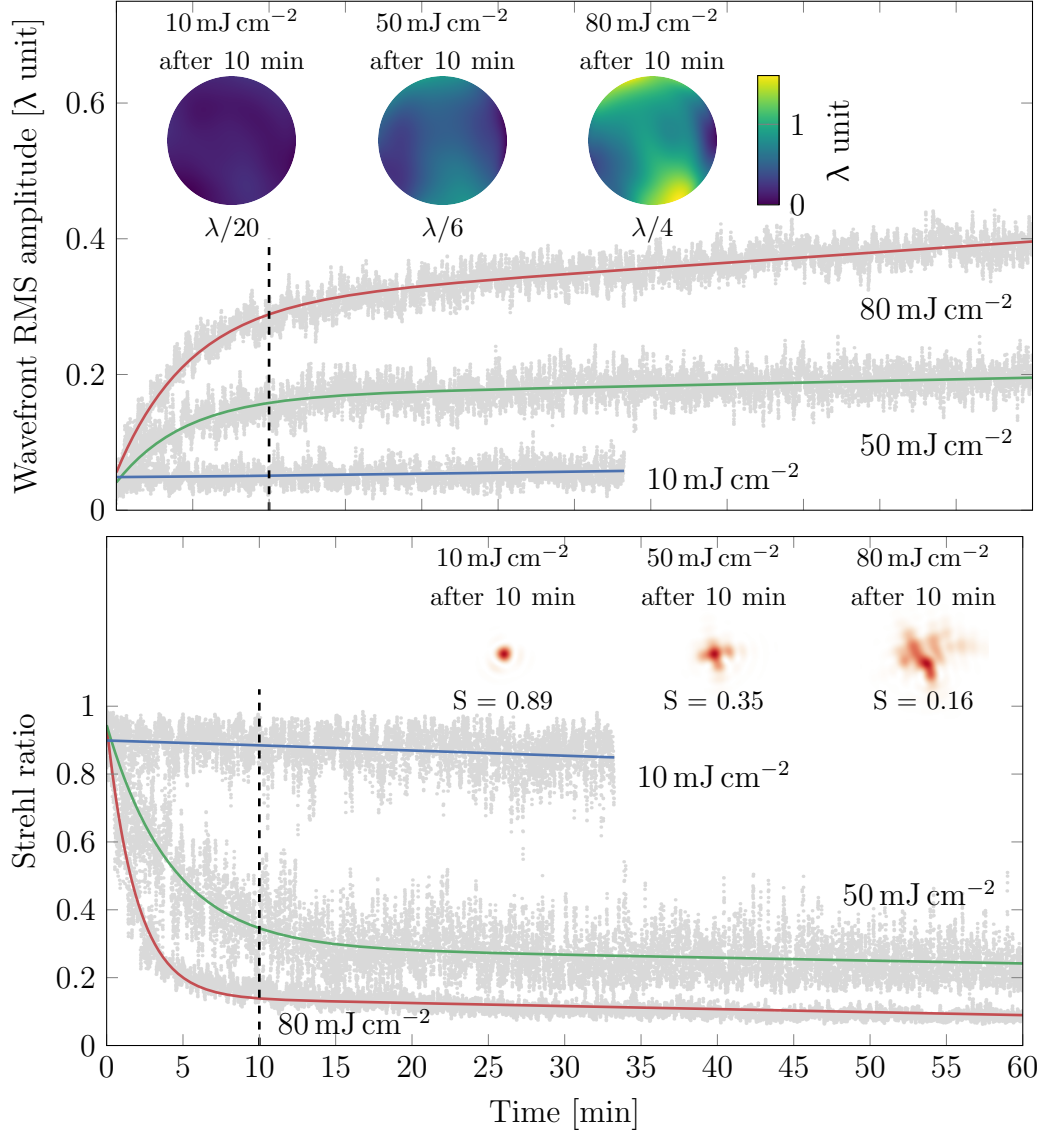
Figure 5.11: Evolution of the wavefront RMS amplitude (top) and the Strehl ratio of the point spread function (bottom) for fluences of $10\,\mathrm{mJ\,cm^{-2}}$ (blue), $50\,\mathrm{mJ\,cm^{-2}}$ (green) and $80\,\mathrm{mJ\,cm^{-2}}$ (red) into the compressor at $5\,\mathrm{Hz}$, which corresponds to average power of $3\,\mathrm{W}$, $15\,\mathrm{W}$, and $24\,\mathrm{W}$. The data (gray dots) is fitted similarly to the divergence (solid color line). The insets show respectively the wavefront map and the normalized PSF spatial profile for the three fluence levels after 10 minutes with the corresponding wavefront RMS amplitude and Strehl ratio value.
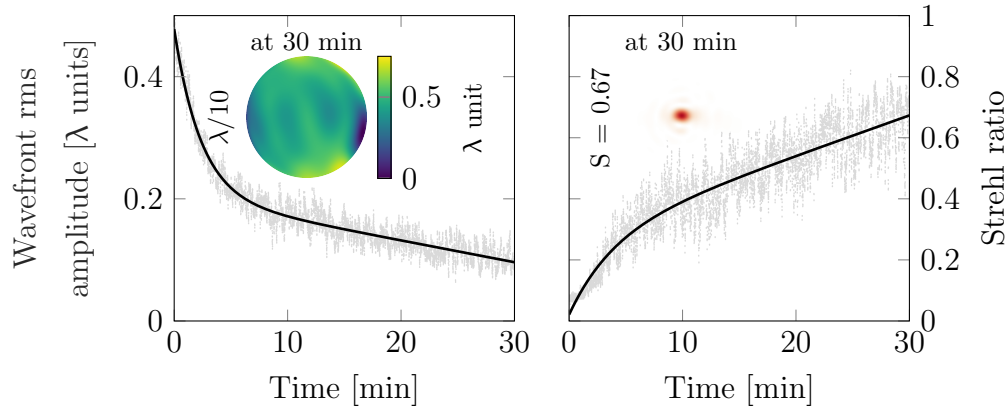
Figure 5.12: Evolution of the wavefront RMS amplitude (left) and the Strehl ratio of the point spread function (right) after a 90 minutes run at $80 \, \mathrm{mJ \, cm^{-2}}$ at $5 \, \mathrm{Hz}$. The insets show respectively the wavefront and the point spread function profile after 30 minutes.

properly sampled at high power, and that no intermediate foci are created while the deformable mirror moves the different actuators, which could increase the fluence on optics past their damage threshold.

From the previous scans, we observed an increase of the divergence and wavefront deformation for an increase of either pulse energy or laser repetition rate. It would indicate that the grating deformations are indeed correlated to the average power, as assumed previously.

5.3   Average power threshold

By combining the two scans, we can study the change of divergence depending on the average power into the compressor which is varied by changing the input energy and the repetition rate. Figure 5.13 shows the average divergence of the horizontal and vertical planes after 30 minutes for all different average power scanned. We further distinguish the data sets acquired before or after the coating deterioration. Nevertheless, the data is in good agreement with the fitted linear slope, which tends to validate the use of continuous diode lasers to reproduce the behavior observed with a compressed pulse [104].

However, we do observe with the thermal camera that the first grating temperature is significantly higher at the output beam height where the
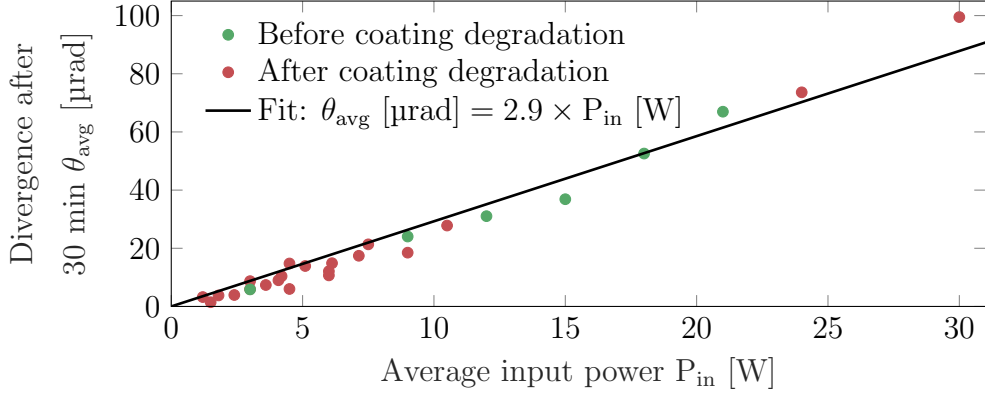
Figure 5.13: Average divergence measured after 30 minutes in function of the laser input average power, ranging from 1.2 W to 30 W. The data (dots) agrees well with the linear fit (solid line), which equation is given in the legend.

beam is compressed. It would indicate that more energy is absorbed in the substrate where the laser pulse is short, even though the pulse energy is already decreased by at least 85 % due to the grating efficiency of the first three passes.

Additionally, we use the Strehl ratio value calculated after 30 minutes as a metric in order to estimate an average power threshold above which the wavefront is too degraded to use the output compressed laser beam for experiments. We still distinguish whether the coating was deteriorated or not. The data represented in Figure 5.14 features two regions with rather constant Strehl ratio: at low input power (typically below 5 W), the deformations of the gratings are negligible and the Strehl ratio stays above 0.9. On the other hand at high average power (above 15 W), the PSF is already so degraded that an additional deformation of the gratings surface will not change significantly the Strehl ratio. From these two observation, the data is fitted by a high order Gaussian curve $\propto \exp\left(\ln\left(S_{\text{lim}}\right) \cdot \left(P/P_{\text{lim}}\right)^{2N}\right)$, to obtain two plateau-like regions at low and high average power, with a smooth transition in-between. From this fit, the order of the Gaussian is $N = 1.2$ and we can retrieve the average power limit for a given Strehl ratio value S_{lim}. For instance, at $S_{\text{lim}} = 0.9$, $P_{\text{lim}} = 5.6$ W and at $S_{\text{lim}} = 0.8$, $P_{\text{lim}} = 7.7$ W. We emphasize that this curve is only a tool to extract a threshold value from the data, and that it depends on the specific compressor design and thermal properties of the setup (i.e. grating mounts, ...).
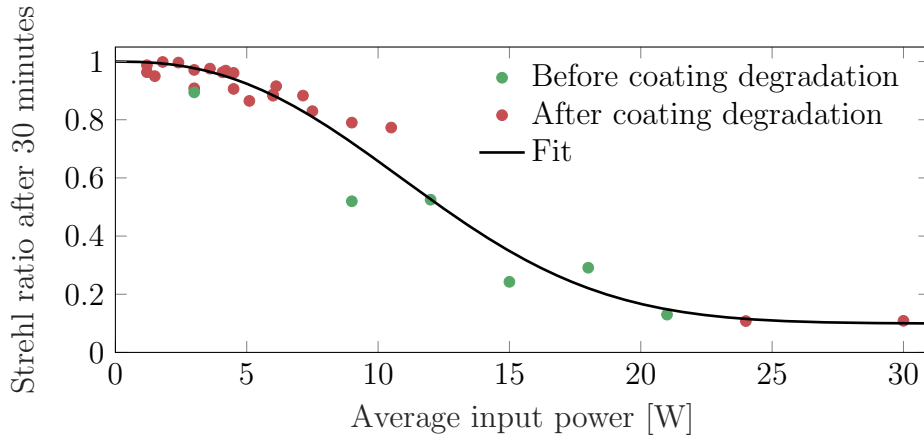
Figure 5.14: Strehl ratio calculated from the PSF after 30 minutes in function of the laser input average power, ranging from 1.2 W to 30 W. The data (dots) is fitted by a high order Gaussian curve (solid line).

Finally, from Figure 5.11, we could observe that the most prominent mode of the wavefront degradation is the astigmatism. Therefore, in combination with the divergence increase, it will shift the longitudinal position of the focal spot. Using the wavefront measured after 30 minutes for all the average power scanned, we can simulate the evolution of the focused beam for the LUX experiment (2 m focal length). We then calculate the change of the laser waist through the focus in the horizontal and vertical planes. These waists are reported in figure 5.15 for the different average power measured, where we highlight the location of the focus in both axis. We observe that above an average power of 10 W, the horizontal focus is already in the middle of the accelerating section of the target (plateau of constant gas density between the two inlets), and above 20 W, it is completely behind the target. As shown previously, the vertical divergence is not degraded as much as the horizontal one, and the location of the vertical focus stays within the target after 30 minutes. Furthermore, the wavefront aberrations increase the minimum waist of the laser, from 25 μm when the gratings are not deformed, and up to 120 μm for an input average power of 30 W.

The investigation of the wavefront degradation due to the in-vacuum deformation shows that the laser cannot be used at its full capacity. Indeed, the focal spot quality is heavily decreased, and its position displaced by more than a target length for the specific case of the LUX experiment. While an online wavefront correction loop is possible in theory, the deformable mirror used in the ANGUS lab does create intermediate foci,
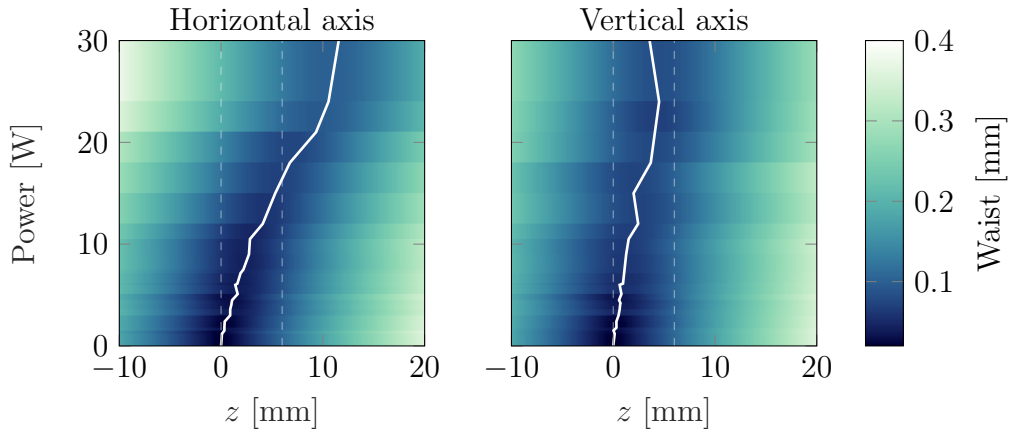
Figure 5.15: Shift of the focus waist position after 30 minutes in function of the laser input average power for the horizontal (left) and vertical (right) axis. The location of the focal planes is indicated by the white solid line. The focal plane in the vertical axis is shifted downstream by up to 4.5 mm and the horizontal axis by up to 11 mm for a laser power of 30 W, which is after the LUX capillary target (the dashed lines represent the inlets for a 10 mm target).

which would dramatically increase the risk of optics damage in the transport beamline or in the compressor.

5.4   Influence of the grating substrate

In order to limit the deformation of the wavefront, the easy and straight-forward solution is to limit the average power of the laser, which reduces the heat absorbed by the grating. However, limiting the energy is not always possible as several experiments rely on threshold processes, which require a lower limit to the energy or the peak intensity such as self-injection in laser plasma accelerator [107]. On the other hand, the repetition rate can be decreased in order to keep the laser energy high enough. While it does not affect the physics studied, it heavily hinders parameter scans and statistical analysis, which rely on a high number of shots to be meaningful. For example, an experiment that requires an afternoon at 5 Hz would need one full day at 1 Hz, where the laser parameters should not vary in the best situation (see figure 3.4 for a counterexample).

Another approach would try to reduce the deformation of the grating for a given absorbed heat. As this coupling happens due to the thermal expansion coefficient of the substrate, carefully choosing the grating material

Table 5.1: Thermal properties of some glass material commonly used for laser optics, reproduced from [108].

Glass material	Heat capacity J/(kg K)	Coefficient of thermal expansion $10^{-6}\,\mathrm{K}^{-1}$	Thermal conductivity W/(m K)	Thermal diffusivity $10^{-6}\,\mathrm{m}^2\,\mathrm{s}^{-1}$
BK7	858	7.1	1.11	0.52
Fused silica	746	0.52	1.38	0.84
Pyrex	1050	3.25	1.13	0.48
ULE (Corning)	767	0.00 ± 0.03	1.31	0.77
Zerodur (Schott)	821	0.00 ± 0.10	1.64	0.79

could limit the deformation of the surface to an acceptable or even negligible level. Table 5.1 summarizes the thermal properties of three common optics materials (BK7, Fused silica, and Pyrex), as well as two glass tailored to have a very low thermal expansion (ULE from Corning[1] and Zerodur from Schott[2]).

We partially investigated the effects of exchanging the substrate material at ANGUS. Indeed, we replaced the 1st grating only using a fused silica substrate, as a larger optic was not available to replace the 2nd grating. Fused silica having a coefficient of thermal expansion more than 6 times smaller than Pyrex, we expect that most of the deformations of the wavefront would come from the 2nd grating and therefore their amplitude would be halved compared to the full Pyrex grating compressor measured previously. Figure 5.16 compares these two situations using an input average laser power of 18 W. We indeed observe that the wavefront amplitude is more than 50 % smaller for the compressor using a fused silica grating. Furthermore, the amplitude is actually very similar to the full Pyrex compressor with a laser average power reduced by half.

Using the same metric as in the previous section, we can compare the average divergence and the relative Strehl ratio of the output laser beam after 30 minutes for different average power. Concerning the compressor with one fused silica grating, only the laser energy was scanned while the repetition rate stayed at 5 Hz. Figures 5.17 and 5.18 show respectively the divergence and the Strehl ratio mentioned. The divergence indicates again

[1]www.corning.com
[2]www.schott.com
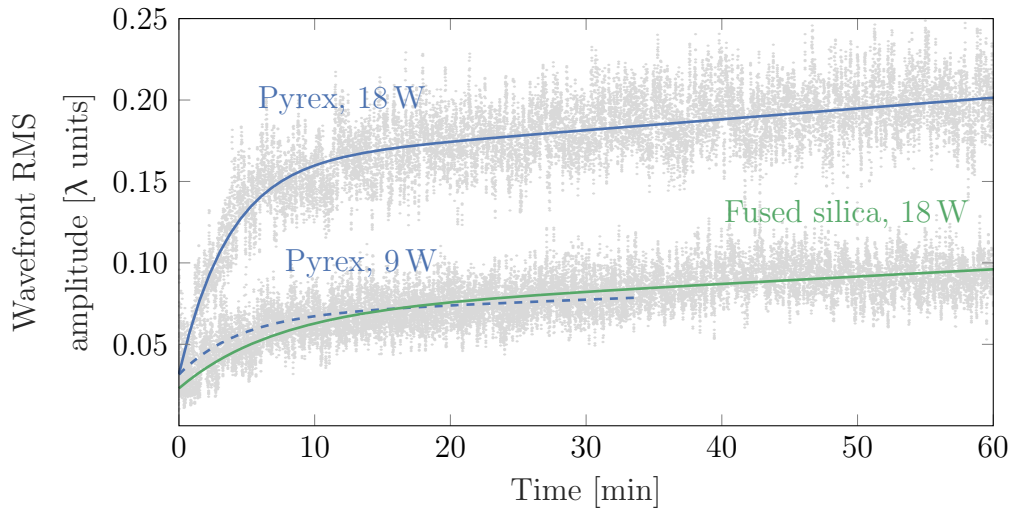
Figure 5.16: Evolution of the wavefront RMS amplitude for an input laser energy of 3.6 J at 5 Hz (solid line) or 2.5 Hz (dashed line), with a full Pyrex grating substrate (blue) or by replacing the 1st grating with a fused silica substrate (green). The amplitude of the wavefront deformation using a fused silica substrate is similar to the full Pyrex situation, but with half the input average power.

that the substrate replacement is decreasing the grating surface deformation by half. Moreover, from figure 5.18, the average power limit for a Strehl ratio of 0.9 is increased from 5.6 W to 12.8 W, which is 2.3 times higher. For a Strehl ratio of 0.8, it increases from 7.7 W to 16.3 W.

These results using a mixed substrate configuration are very promising and could be a very effective solution to drastically mitigate the grating deformation and the spoilage of the focal spot. The procurement of a 2nd grating with a fused silica substrate is currently considered in order to directly and accurately compare the effect of the substrate on the wavefront degradation. Based on figures 5.17 and 5.18, there is a good hope that a full fused silica grating compressor could actually handle the full available average power of the ANGUS laser. Furthermore, it would be interesting to investigate whether any wavefront degradation would be measurable using a glass material specially tailored to have close to no thermal expansion at room temperature. However, the substrate is only half of the story. To be used at full power, the coating of the grating should not be damaged.
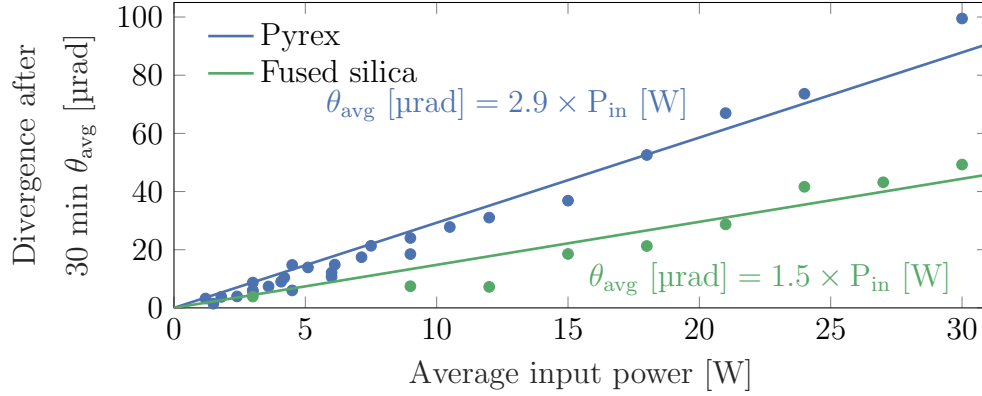
Figure 5.17: Average divergence measured after 30 minutes in function of the laser input average power, for two different substrates of the 1st grating. The Pyrex grating (green) data is identical to figure 5.13. The compressor with one fused silica grating (blue) induces half the divergence of the full Pyrex compressor. The equations of the fits (solid lines) are reported in the plot.

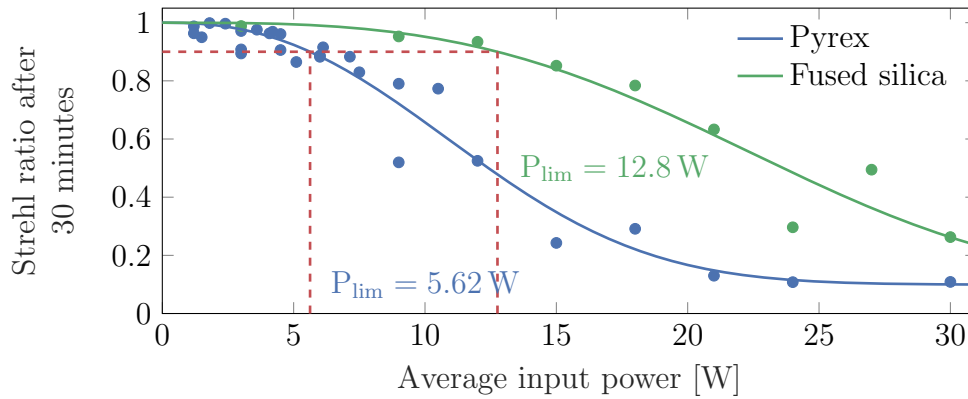Figure 5.18: Strehl ratio calculated from the PSF after 30 minutes in function of the laser input average power, for two different substrates of the 1st grating. Again, the Pyrex data (green) is reproduced from figure 5.14. The deformation is less severe if one grating is replaced by a fused silica substrate (blue), and the average power threshold defined from the fit (solid line) is more than twice higher.

119

5.5 Coating deterioration

As already reported in section 5.2.2, we observed a deterioration of the gold coating where the 4$^{\text{th}}$ pass hits the grating surface. It has the characteristic shape of the laser near field profile and looks like a veil or an imprint on the coating. For the four gratings tested (see table 5.2), this damage was present for two of them with different substrates (A and B, with respectively Pyrex and fused silica substrates). Therefore, it appears that the damage we observed is mainly due to the coating characteristics (shape of the grooves, with or without of photoresist, etc.) rather than the substrate used. However, due to a lack of knowledge on the specific manufacturing process of the grating providers, we cannot look into the specifics of the damaging process, but mainly study the features left on the grating and on the diffracted beam profile.

Table 5.2: Basic characteristics of the different gratings tested.

Grating	Substrate	Groove material	Damage observed?
A	Pyrex	Photoresist	Yes
B	Fused silica	Photoresist	Yes
C	Fused silica	Etched in substrate	Yes, but unrelated
D	Fused silica	Photoresist	No

However, the fact that the 1$^{\text{st}}$ pass was not damaged even though the laser energy is higher than the 4$^{\text{th}}$ pass suggests that the pulse duration of the laser plays a critical role in the damaging mechanism, and that the damage threshold would scale with the intensity (or the electric field amplitude) rather than the typical fluence, which is a time integrated quantity. For gratings with dielectric coating, the damage threshold scales as $1/E_{\max}^2$ [50], due to the field enhancement within the deep grooves. While Wang *et al.* [45] report a damage threshold of gold coated gratings above $400\,\text{mJ}\,\text{cm}^{-2}$, they do emphasize that the field enhancement affects the local temperature of the surface and therefore the thermal stress at the interface of the gold film and the photoresist, which could eventually result in blistering or peeling off of the gold film. Without observing the damaged area with a microscope, we cannot be sure that this process is responsible for our damage, but at least it emphasizes the importance of the pulse duration in the determination of the damage threshold.

5.5.1 Damage threshold determination

Through the sections 5.2 to 5.4, we reported on several measurements where the high power laser was sent into the compressor with different pulse energies using gratings A and B. During these tests, we observed visually the grating surface and saw an imprint of the laser profile appearing on the last pass when the input laser fluence was at $80\,\mathrm{mJ\,cm^{-2}}$. However, we could not detect this effect on the output laser energy. In fact, the beam used for diagnostics is the leakthrough of the last mirror in the compressor chamber (see figure 3.12). As the high reflectivity coating does not fully cover the mirror substrate, a small fraction of the very top edge of the beam was going through the uncoated part of the substrate and had a significantly higher energy than the rest of the beam attenuated by the high reflectivity coating. Therefore, to identify the moment when the damage appears, we used a camera looking at the grating surface with an objective. In fact, the scattering of the laser beam is visible for both the 1st and 4th passes. As the scattering is proportional to the laser fluence, we use the 1st pass to normalize the signal from the 4th pass and therefore account for the different pulse energy or camera filter settings used.
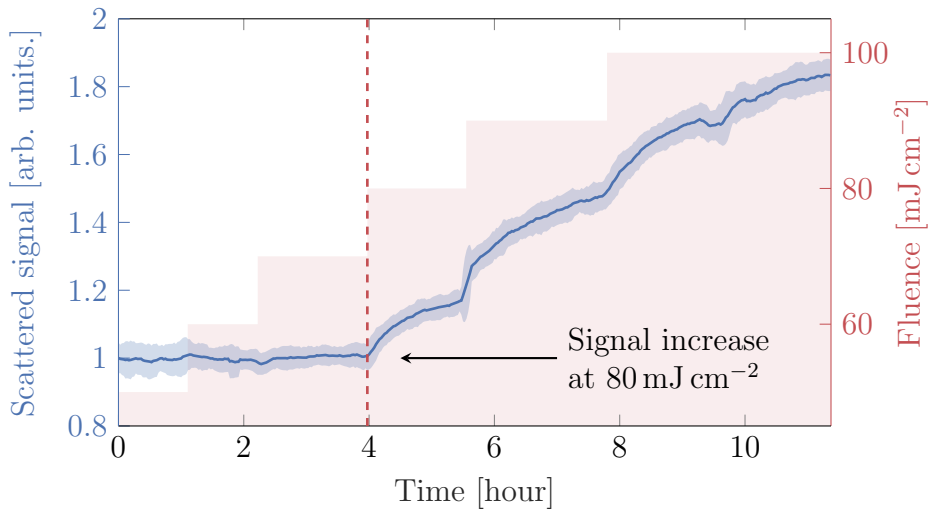
Figure 5.19: Increase of the 4th pass normalized scattering signal (blue line with 2σ shaded area) during an energy scan (red area) at constant repetition rate of $5\,\mathrm{Hz}$ with grating B. The increase of the scattering signal can be clearly identified at the beginning of the $80\,\mathrm{mJ\,cm^{-2}}$ run. While the signal increased, the camera was saturating and the filter levels were changed, explaining the jumps in the trend.

We can see from figure 5.19 that the normalized scattering signal of the 4th pass is constant up to an input fluence of $70\,\text{mJ}\,\text{cm}^{-2}$, but it is constantly increasing for a continued exposure to fluences above $80\,\text{mJ}\,\text{cm}^{-2}$. We can thus identify that the damage threshold is within these two values. Knowing that the compressed pulse duration was $40\,\text{fs}$, we can further estimate the boundaries of the intensity and the field strength required to damage the grating coating. Considering the efficiency of the grating, the intensity threshold is then between $1.4\,\text{TW/cm}^2$ and $1.6\,\text{TW/cm}^2$, and the field strength threshold is between $3.2\,\text{GV/m}$ and $3.4\,\text{GV/m}$ in the plane of the grating.

Furthermore, because the grating was under laser exposure before the first shots at $80\,\text{mJ}\,\text{cm}^{-2}$, we cannot be certain that the coating had not been worn down by the previous $90\,000$ shots at an increasing laser energy. Nevertheless, as the scattering signal increases right at the beginning of the run above the threshold, this effect could very well be small enough to be neglected. However, to test this assumption, an S-on-1 damage test (S shots at a given fluence) would be required.

5.5.2 Deterioration increase under continued exposure

After the observation of the coating damage, we decided to continue shooting on grating A for several hours over a few days at an average fluence of $100\,\text{mJ}\,\text{cm}^{-2}$ at $5\,\text{Hz}$. We could therefore monitor the evolution of the damaged area. Figure 5.20 shows pictures of the damaged surface after 4, 8, 12, and 18 hours of exposure to the ANGUS laser. We observe that an increasing area of the grating surface shows a decrease in reflectivity and has a matte appearance. This damage affecting the reflectivity of the surface implies that it degrades the gold film. However, we cannot conclude on the groove profile. If it remains unaffected, the grating could eventually be recoated to recover its original reflective properties.

In addition to the pictures, we also recorded the scattering signal while the laser was sent in the compressor as previously. The scattered light was intense enough to saturate the CCD chip. Therefore, by measuring the saturated area in the camera images, we can monitor the increase of the damaged area. Figure 5.21 shows this increase, normalized to the projected beam area. The saturated area corresponds in first approximation to the matte area of the surface which no longer reflects light. After $100\,000$ shots (roughly $5\,\frac{1}{2}$ hours), $5\,\%$ of the scattered signal is saturated, $15\,\%$ after
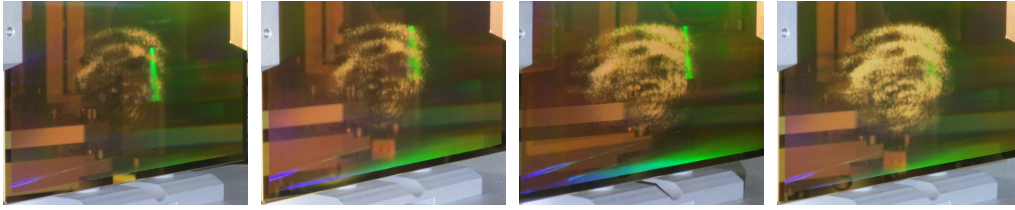
Figure 5.20: Evolution of the grating A coating deterioration after (from left to right) 4 hours, 8 hours, 12 hours and 18 hours of exposure to a $100\,\mathrm{mJ\,cm}^{-2}$ beam at $5\,\mathrm{Hz}$.

200 000 shots, and more than $30\,\%$ after 300 000 shots (17 hours). As this area corresponds to the part of the grating with a decreased reflectivity, this fraction of the beam profile will be missing from the output beam, which therefore decreases the laser energy and spoils the near field quality.
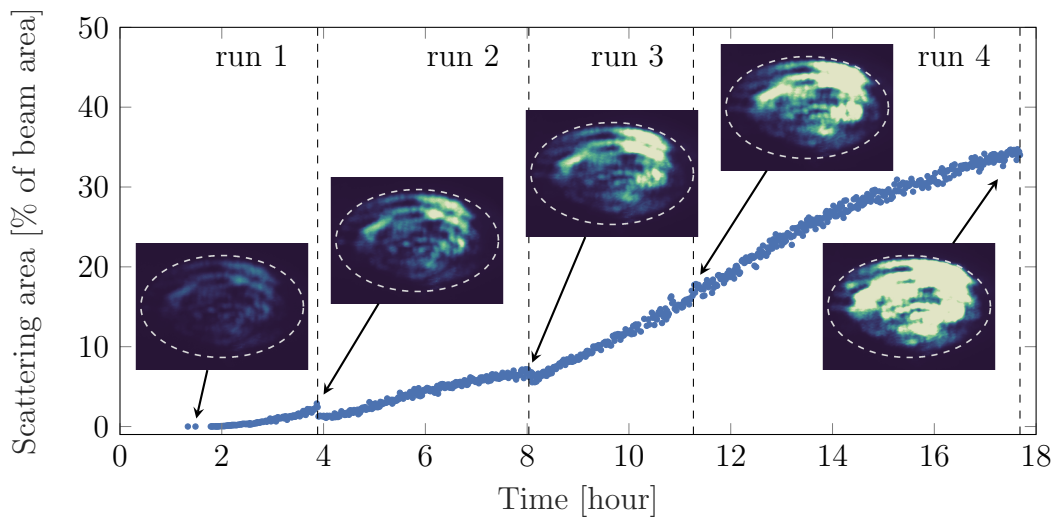
Figure 5.21: Evolution of the scattering area of grating A over 18 hours of exposure to a $100\,\mathrm{mJ\,cm}^{-2}$ beam at $5\,\mathrm{Hz}$, in percent of the full beam area (blue dots). It corresponds to the saturated signal retrieved by the camera (uniform light green area on insets). The insets show the camera signal at the beginning and end of each run, with the beam size overlaid (white dashed line). The jumps of the signal between the runs are due to a small shift of the beam position on the grating which changes the scattered signal.

5.5.3 Influence on the beam profile

Using a monochromatic continuous laser beam—called pilot beam—which is collinear to the ANGUS laser in order to pre-align optics down the beamline, we measured inside the vented compressor chamber the gratings efficiency in three places after the 4 runs presented above (after the 1$^\text{st}$ pass, before the 3$^\text{rd}$ pass, and after the 4$^\text{th}$ pass). Such a measurement is difficult with a broadband source due to the angular dispersion after the first grating. Knowing the mirrors reflectivity in the two polarizations, and assuming an equal efficiency for the 2$^\text{nd}$ and 3$^\text{rd}$ passes (second grating), we can calculate the efficiency of the gratings. We find out that the second grating efficiency is 92.5 % and the undamaged area of the first grating (1$^\text{st}$ pass) is 93.8 %, which is above the specified efficiency of 90 %. However, the damaged area of the first grating (4$^\text{th}$ pass) has an efficiency of 48.3 %, which is 1.9 times lower than the undamaged area.

Furthermore, we measured the near field of the pilot beam after the compressor with the damaged grating and with a new grating. Figure 5.22 shows the difference between the two measurements. The shadow of the damage can be clearly seen. The bottom pictures show a direct comparison of the damage features and the holes in the near field profile. They clearly show that the damaged grating is no longer usable to compress high power laser beams.

As explained at the beginning of this section, the damages were observed for two gratings with different substrates (A and B). The grating D with a fused silica substrate but with a different design of the grooves shape and coating has been tested successfully up to a fluence of $80\,\text{mJ}\,\text{cm}^{-2}$ for 2 hours, and another fused silica grating, which uses no photoresist (grating C) has also been tested up to $100\,\text{mJ}\,\text{cm}^{-2}$. A damage appeared at the last energy level, but it was due to a bad cleanliness of the surface, the damage was only present on a single spot at the edge of the laser beam profile and is therefore not related to our previous observations. These two additional tests show encouraging prospects for the usability of gold coated gratings for such ultrashort laser system at high repetition rates, as the fused silica substrate deformations could be small enough to be neglected and the coating can hold under such exposure for at least several hundred thousand shots. However, they show that the damage threshold of the gold-coated diffraction gratings can be different between optics with the same specifications, even within the products of the same company. It is the reason why damage threshold determination is difficult, but at the same time critical.
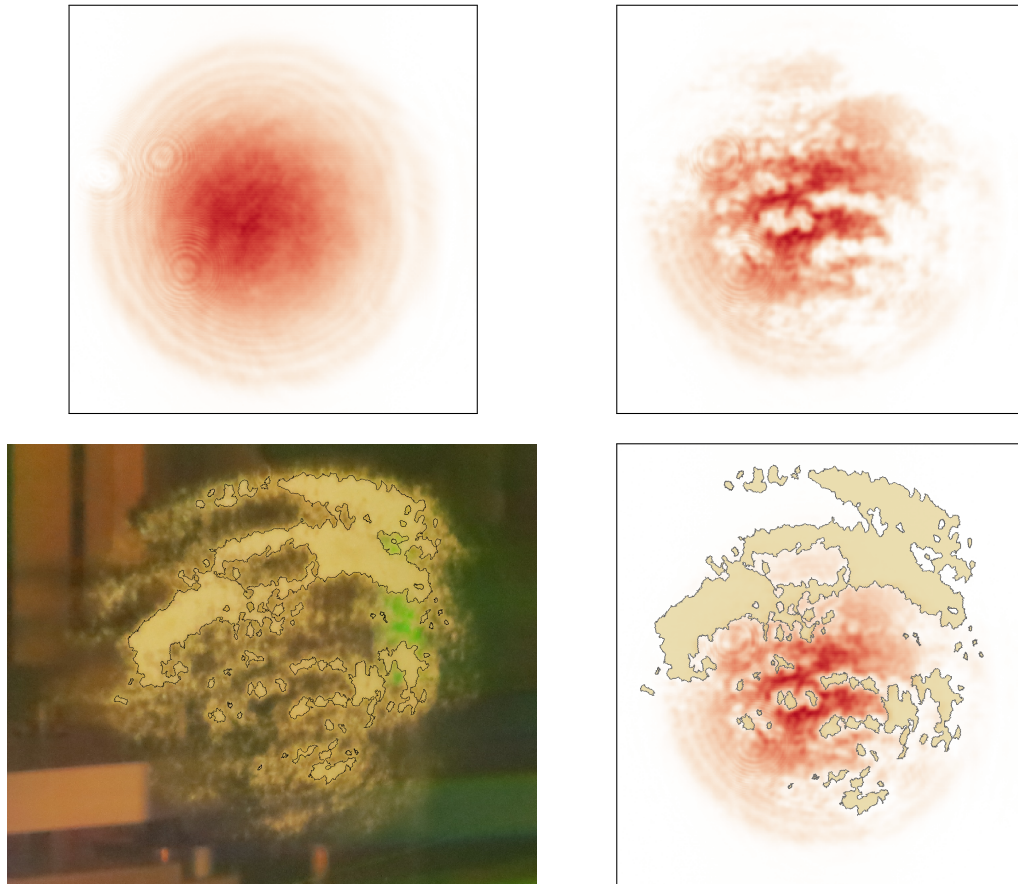
Figure 5.22: Near field profile of the pilot beam measured at the post-compressor diagnostics with an undamaged grating (top left) and with the grating after the 18 hours exposure (top right). The damaged area of the coating is outlined on the picture (bottom left) and reported on the near field (bottom right), after compensation for the perspective.

Chapter 6

Conclusion

In this work, we have outlined two critical aspects of high power laser systems that become prominent due to the high repetition rate of the ANGUS laser: the target deterioration by the spatial contrast, and the transient degradation of the laser wavefront due to the high average power absorbed by the gratings.

On the first point, we reported the measurements of the wavefront including all the aberrations of the transport beamline and focusing optic. We could conclude from this measurement that the focal spot quality was high enough to safely operate the electron source. However, a careful measurement of the far field pattern with a high dynamic range revealed features at the 10^{-4} level that were not explained by the measured wavefront. An analysis of the discrepancies showed that the most likely culprit for this difference was a reduced aperture in the measurement which limits the beam aperture where the wavefront is corrected by the deformable mirror. It was recently found that an iris in the pre-target diagnostics was indeed limiting the aperture to $82\,\%$ of the aperture measurable by the wavefront sensor. While the corrected wavefront has now a higher amplitude and thus the computed Strehl ratio is lower, they are more representative of the actual laser focus. However, a new high dynamic range measurement is still required to quantify the change in spatial contrast and to verify if the calculations from the wavefront measurement can be trusted. Finally, this measurement would also allow us to compare the direct wavefront measurement to the phase retrieval algorithm, which should give comparable results. Nevertheless, recent results of the LUX beamline showed a long-term operation of the capilary target, which was not degraded after more than $100\,000$ shots using a hard aperture as a workaround solution.

However, because of the deformation of the gratings, all the efforts put into the wavefront optimization using a low energy beam are wasted if

the average power of the laser is too high. Indeed, by performing a large parameter scan of the laser energy and repetition rate on several gratings—resulting in more than one million shots over a total of 62 hours—we could observe that the laser wavefront becomes to degraded if the input power is above 5.6 W with Pyrex based gratings. However, preliminary results on fused silica substrate show encouraging prospects towards a high average power operation of the ANGUS system. Additionally, we could observe a damage appearing on the grating where the compressed pulse hits the surface, which seems related to the specific design of the groove structure and geometry. Nevertheless, some of the tested optics showed a high enough damage threshold, which could again ensure that the compressor can be used at the full laser energy. To completely compare the influence of the substrate material, the second grating of the compressor should be replaced by a grating with a fused silica substrate, and then repeat the parameter scans.

Thanks to these two measurements, we now have a better understanding of the practical limitations to the repetition rate of the current ANGUS laser and the LUX beamline, as well as the next steps necessary to take in order to reach the full potential of our driver laser. Implementing these steps, namely having a full fused silica based compressor and ensuring the high spatial contrast for long term operation of the capillary target with the full aperture wavefront correction, would help to bridge the gap between a laser plasma acceleration experiment and a laser plasma accelerator producing GeV-range, reliable and reproducible electrons beams at 5 Hz for several hours. The LUX beamline has already taken the first steps towards that goal with several 24 hours operation at up to 1 Hz.

Bibliography

[1]   D. Strickland and G. Mourou, "Compression of amplified chirped optical pulses," *Optics Communications*, vol. 56, no. 3, pp. 219–221, 1985.

[2]   G. A. Mourou, G. Korn, W. Sandner, and J. L. Collier, *Extreme Light Infrastructure Whitebook*. Andreas Thoss.

[3]   C. Danson, D. Hillier, N. Hopps, and D. Neely, "Petawatt class lasers worldwide," *High Power Laser Science and Engineering*, vol. 3, 2015.

[4]   G. A. Mourou, T. Tajima, and S. V. Bulanov, "Optics in the relativistic regime," *Rev. Mod. Phys.*, vol. 78, pp. 309–371, 2006.

[5]   T. Tajima and J. M. Dawson, "Laser electron accelerator," *Phys. Rev. Lett.*, vol. 43, pp. 267–270, 1979.

[6]   X. F. Li, A. L'Huillier, M. Ferray, L. A. Lompré, and G. Mainfray, "Multiple-harmonic generation in rare gases at high laser intensity," *Phys. Rev. A*, vol. 39, pp. 5751–5761, 1989.

[7]   J. Hein, S. Podleska, M. Siebold, M. Hellwing, R. Bödefeld, R. Sauerbrey, D. Ehrt, and W. Wintzer, "Diode-pumped chirped pulse amplification to the joule level," *Applied Physics B*, vol. 79, no. 4, pp. 419–422, 2004.

[8]   J. Tümmler, R. Jung, H. Stiel, P. V. Nickles, and W. Sandner, "High-repetition-rate chirped-pulse-amplification thin-disk laser system with joule-level pulse energy," *Opt. Lett.*, vol. 34, no. 9, pp. 1378–1380, 2009.

[9]   C. W. Siders and C. Haefner, "High-power lasers for science and society," tech. rep., Lawrence Livermore National Lab., 2016.

[10] G. Genoud, M. S. Bloom, J. Vieira, M. Burza, Z. Najmudin, A. Persson, L. O. Silva, K. Svensson, C.-G. Wahlström, and S. P. D.

Mangles, "Increasing energy coupling into plasma waves by tailoring the laser radial focal spot distribution in a laser wakefield accelerator," *Physics of Plasmas*, vol. 20, no. 6, p. 064501, 2013.

[11]   N. Delbos, C. Werle, I. Dornmair, T. Eichner, L. Hübner, S. Jalas, S. Jolly, M. Kirchen, V. Leroux, P. Messner, M. Schnepp, M. Trunk, P. Walker, P. Winkler, and A. Maier, "LUX: A laser-plasma driven undulator beamline," *Nucl. Instr. Meth. Phys. Res. A*, 2018.

[12]   T. H. Maiman, "Stimulated optical radiation in ruby," *Nature*, vol. 187, no. 4736, pp. 493–494, 1960.

[13]   R. W. Hellwarth, "Control of Fluorescent Pulsations," in *Advances in Quantum Electronics* (J. R. Singer, ed.), p. 334, 1961.

[14]   L. E. Hargrove, R. L. Fork, and M. A. Pollack, "Locking of HeNe laser modes induced by synchronous intracavity modulation," *Applied Physics Letters*, vol. 5, no. 1, pp. 4–5, 1964.

[15]   P. Moulton, "Ti-doped sapphire: tunable solid-state laser," *Optics News*, vol. 8, no. 6, p. 9, 1982.

[16]   D. E. Spence, P. N. Kean, and W. Sibbett, "60-fsec pulse generation from a self-mode-locked Ti:sapphire laser," *Opt. Lett.*, vol. 16, no. 1, pp. 42–44, 1991.

[17]   C. E. Cook, "Pulse compression-key to more efficient radar transmission," *Proceedings of the IRE*, vol. 48, no. 3, pp. 310–316, 1960.

[18]   N. Bonod and J. Neauport, "Diffraction gratings: from principles to applications in high-intensity lasers," *Advances in Optics and Photonics*, vol. 8, no. 1, pp. 156–199, 2016.

[19]   K. Osvay and I. N. Ross, "On a pulse compressor with gratings having arbitrary orientation," *Optics Communications*, vol. 105, no. 3, pp. 271–278, 1994.

[20]   J. H. Sung, T. J. Yu, S. K. Lee, T. M. Jeong, I. W. Choi, D.-K. Ko, and J. Lee, "Design of a femtosecond Ti:sapphire laser for generation and temporal optimization of a 0.5-PW laser pulses at a 0.1-Hz repetition rate," *Journal of the Optical Society of Korea*, vol. 13, no. 1, pp. 53–59, 2009.

[21]   G. Cheriaux, B. Walker, L. F. Dimauro, P. Rousseau, F. Salin, and J. P. Chambaret, "Aberration-free stretcher design for ultrashort-pulse amplification," *Opt. Lett.*, vol. 21, no. 6, pp. 414–416, 1996.

[22] K. F. Wall and A. Sanchez, "Titanium sapphire lasers," *Lincoln Laboratory Journal*, vol. 3, pp. 447–462, 1990.

[23] K. Renk, *Basics of Laser Physics: For Students of Science and Engineering.* Graduate Texts in Physics, Springer International Publishing, 2017.

[24] P. W. Roth, A. J. Maclean, D. Burns, and A. J. Kemp, "Directly diode-laser-pumped Ti:sapphire laser," *Opt. Lett.*, vol. 34, no. 21, pp. 3334–3336, 2009.

[25] S. Backus, M. Kirchner, R. Lemons, D. Schmidt, C. Durfee, M. Murnane, and H. Kapteyn, "Direct diode pumped Ti:sapphire ultrafast regenerative amplifier system," *Opt. Express*, vol. 25, no. 4, pp. 3666–3674, 2017.

[26] P. F. Moulton, "Spectroscopic and laser characteristics of Ti:Al2O3," *J. Opt. Soc. Am. B*, vol. 3, no. 1, pp. 125–133, 1986.

[27] W. R. Rapoport and C. P. Khattak, "Titanium sapphire laser characteristics," *Appl. Opt.*, vol. 27, no. 13, pp. 2677–2684, 1988.

[28] L. M. Frantz and J. S. Nodvik, "Theory of pulse propagation in a laser amplifier," *Journal of Applied Physics*, vol. 34, no. 8, pp. 2346–2349, 1963.

[29] P. Tournois, "Acousto-optic programmable dispersive filter for adaptive compensation of group delay time dispersion in laser systems," *Optics Communications*, vol. 140, no. 4, pp. 245–249, 1997.

[30] C. Palmer and E. Loewen, *Diffraction Grating Handbook.* Newport Corporation.

[31] D. Rudolph and G. Schmal, "Verfahren zur Herstellung von Röntgenlinsen und Beugungsgittern," *Umschau Wiss. Tech.*, no. 78, p. 225, 1967.

[32] A. Labeyrie and J. Flamand, "Spectrographic performance of holographically made diffraction gratings," *Optics Communications*, vol. 1, no. 1, pp. 5–8, 1969.

[33] C. G. Chen, P. T. Konkola, R. K. Heilmann, G. S. Pati, and M. L. Schattenburg, "Image metrology and system controls for scanning beam interference lithography," *J. Vac. Sci. Technol. B*, vol. 19, no. 6, pp. 2335–2341, 2001.

[34] R. W. Wood, "On a remarkable case of uneven distribution of light in a diffraction grating spectrum," *Proceedings of the Physical Society of London*, vol. 18, no. 1, p. 269, 1902.

[35] T. Jitsuno, S. Motokoshi, T. Okamoto, T. Mikami, D. Smith, M. L. Schattenburg, H. Kitamura, H. Matsuo, T. Kawasaki, K. Kondo, H. Shiraga, Y. Nakata, H. Habara, K. Tsubakimoto, R. Kodama, K. A. Tanaka, N. Miyanaga, and K. Mima, "Development of 91 cm size gratings and mirrors for LEFX laser system," *Journal of Physics: Conference Series*, vol. 112, no. 3, p. 032002, 2008.

[36] D. A. Alessi, C. W. Carr, R. P. Hackel, R. A. Negres, K. Stanion, J. E. Fair, D. A. Cross, J. Nissen, R. Luthi, G. Guss, J. A. Britten, W. H. Gourdin, and C. Haefner, "Picosecond laser damage performance assessment of multilayer dielectric gratings in vacuum," *Opt. Express*, vol. 23, no. 12, pp. 15532–15544, 2015.

[37] K. R. P. Kafka, N. Talisa, G. Tempea, D. R. Austin, C. Neacsu, and E. A. Chowdhury in *Few-cycle pulse laser-induced damage of thin films in air and vacuum ambience*, vol. 10014, 2016.

[38] M. Ďurák, D. Kramer, P. K. Velpula, A. R. Meadows, J. Cupal, and B. Rus, "Comparison of different LIDT testing protocols for PW and multi-PW class high-reflectivity coatings," in *Proc. SPIE*, vol. 10014, 2016.

[39] B. C. Stuart, M. D. Feit, S. M. Herman, A. M. Rubenchik, B. W. Shore, and M. D. Perry, "Ultrashort-pulse optical damage," in *Proc. SPIE*, vol. 2714, pp. 2714–2728, 1996.

[40] M. A. Ordal, L. L. Long, R. J. Bell, S. E. Bell, R. R. Bell, R. W. Alexander, and C. A. Ward, "Optical properties of the metals Al, Co, Cu, Au, Fe, Pb, Ni, Pd, Pt, Ag, Ti, and W in the infrared and far infrared," *Appl. Opt.*, vol. 22, no. 7, pp. 1099–1119, 1983.

[41] S. Palmier, J. Neauport, N. Baclet, E. Lavastre, and G. Dupuy, "High reflection mirrors for pulse compression gratings," *Opt. Express*, vol. 17, no. 22, pp. 20430–20439, 2009.

[42] R. D. Boyd, J. A. Britten, D. E. Decker, B. W. Shore, B. C. Stuart, M. D. Perry, and L. Li, "High-efficiency metallic diffraction gratings for laser applications," *Appl. Opt.*, vol. 34, no. 10, pp. 1697–1706, 1995.

[43] P. Poole, S. Trendafilov, G. Shvets, D. Smith, and E. Chowdhury, "Femtosecond laser damage threshold of pulse compression gratings for petawatt scale laser systems," *Opt. Express*, vol. 21, no. 22, pp. 26341–26351, 2013.

[44] J. Neauport, E. Lavastre, G. Razé, G. Dupuy, N. Bonod, M. Balas, G. de Villele, J. Flamand, S. Kaladgew, and F. Desserouer, "Effect of electric field on laser induced damage threshold of multilayer dielectric gratings," *Opt. Express*, vol. 15, no. 19, pp. 12508–12522, 2007.

[45] L. Wang, F. Kong, Z. Xia, Y. Jin, H. Huang, L. Li, J. Chen, Y. Cui, and J. Shao, "Evaluation of femtosecond laser damage to gold pulse compression gratings fabricated by magnetron sputtering and e-beam evaporation," *Appl. Opt.*, vol. 56, no. 11, pp. 3087–3095, 2017.

[46] M. D. Perry, B. C. Stuart, P. S. Banks, M. D. Feit, V. Yanovsky, and A. M. Rubenchik, "Ultrashort-pulse laser machining of dielectric materials," *Journal of Applied Physics*, vol. 85, no. 9, pp. 6803–6810, 1999.

[47] M. D. Perry, C. Shannon, E. Shults, R. D. Boyd, J. A. Britten, D. Decker, and B. W. Shore, "High-efficiency multilayer dielectric diffraction gratings," *Opt. Lett.*, vol. 20, no. 8, pp. 940–942, 1995.

[48] D. H. Martz, H. T. Nguyen, D. Patel, J. A. Britten, D. Alessi, E. Krous, Y. Wang, M. A. Larotonda, J. George, B. Knollenberg, B. M. Luther, J. J. Rocca, and C. S. Menoni, "Large area high efficiency broad bandwidth 800 nm dielectric gratings for high energy laser pulse compression," in *CLEO/QELS: 2010 Laser Science to Photonic Applications*, pp. 1–2, 2010.

[49] F. Kong, S. Chen, Y. Jin, S. Liu, H. Guan, Y. Du, and H. He, "Investigation of fs-laser induced damage on high reflection mirrors used for 800nm broadband pulse compression gratings," *Optics & Laser Technology*, vol. 54, no. Supplement C, pp. 45–49, 2013.

[50] J. A. Britten, W. A. Molander, A. M. Komashko, and C. P. J. Barty, "Multilayer dielectric gratings for petawatt-class laser systems," in *Proc. SPIE*, vol. 5273, pp. 5273–5280, 2004.

[51] N. Bonod and J. Neauport, "Optical performance and laser induced damage threshold improvement of diffraction gratings used as compressors in ultra high intensity lasers," *Optics Communications*, vol. 260, no. 2, pp. 649–655, 2006.

[52] C. J. Stolz, J. R. Taylor, W. K. Eickelberg, and J. D. Lindh, "Effects of vacuum exposure on stress and spectral shift of high reflective coatings," *Appl. Opt.*, vol. 32, no. 28, pp. 5666–5672, 1993.

[53] D. Voelz, *Computational Fourier Optics: A MATLAB Tutorial.* SPIE Press, 2011.

[54] R. J. Noll, "Zernike polynomials and atmospheric turbulence," *J. Opt. Soc. Am.*, vol. 66, no. 3, pp. 207–211, 1976.

[55] J. F. Hartmann, "Bemerkungen über den Bau und die Justirung von Spektrographen," *Zeitschrift für Instrumentenkunde*, vol. 20, pp. 2704–2716, 1900.

[56] R. V. Shack and B. C. Platt, "Production and use of a lenticular Hartmann screen," in *Program of the 1971 Spring Meeting of the Optical Society of America*, p. 656, 1971.

[57] K. Liu, X. Wang, and Y. Li, "Local slope and curvature tests via wave front modulations in the Shack-Hartmann sensor," *IEEE Photonics Technology Letters*, vol. 29, no. 10, pp. 842–845, 2017.

[58] J. Primot, "Three-wave lateral shearing interferometer," *Appl. Opt.*, vol. 32, no. 31, pp. 6242–6249, 1993.

[59] J. Primot and L. Sogno, "Achromatic three-wave (or more) lateral shearing interferometer," *J. Opt. Soc. Am. A*, vol. 12, no. 12, pp. 2679–2685, 1995.

[60] J.-C. Chanteloup, "Multiple-wave lateral shearing interferometry for wave-front sensing," *Appl. Opt.*, vol. 44, no. 9, pp. 1559–1571, 2005.

[61] J. Primot, "Theoretical description of shackhartmann wave-front sensor," *Optics Communications*, vol. 222, no. 1, pp. 81–92, 2003.

[62] J. Primot and N. Guérineau, "Extended hartmann test based on the pseudoguiding property of a hartmann mask completed by a phase chessboard," *Appl. Opt.*, vol. 39, no. 31, pp. 5715–5720, 2000.

[63] H. W. Babcock, "The possibility of compensating astronomical seeing," *Publications of the Astronomical Society of the Pacific*, vol. 65, pp. 229–236, 1953.

[64] F. Druon, G. Chériaux, J. Faure, J. Nees, M. Nantel, A. Maksimchuk, G. Mourou, J. C. Chanteloup, and G. Vdovin, "Wave-front correction of femtosecond terawatt lasers by deformable mirrors," *Opt. Lett.*, vol. 23, no. 13, pp. 1043–1045, 1998.

[65] V. N. Mahajan, "Strehl ratio for primary aberrations in terms of their aberration variance," *J. Opt. Soc. Am.*, vol. 73, no. 6, pp. 860–861, 1983.

[66] V. V. Ivanov, A. Maksimchuk, and G. Mourou, "Amplified spontaneous emission in a ti:sapphire regenerative amplifier," *Appl. Opt.*, vol. 42, no. 36, pp. 7231–7234, 2003.

[67] A. Jullien, O. Albert, F. Burgy, G. Hamoniaux, J.-P. Rousseau, J.-P. Chambaret, F. Augé-Rochereau, G. Chériaux, J. Etchepare, N. Minkovski, and S. M. Saltiel, "10^{-10} temporal contrast for femtosecond ultraintense lasers by cross-polarized wave generation," *Opt. Lett.*, vol. 30, no. 8, pp. 920–922, 2005.

[68] A. Jullien, O. Albert, G. Chériaux, J. Etchepare, S. Kourtev, N. Minkovski, and S. M. Saltiel, "Two crystal arrangement to fight efficiency saturation in cross-polarized wave generation," *Opt. Express*, vol. 14, no. 7, pp. 2760–2769, 2006.

[69] K. Nakamura, H. S. Mao, A. J. Gonsalves, H. Vincenti, D. E. Mittelberger, J. Daniels, A. Magana, C. Toth, and W. P. Leemans, "Diagnostics, control and performance parameters for the BELLA high repetition rate petawatt class laser," *IEEE Journal of Quantum Electronics*, vol. 53, no. 4, pp. 1–21, 2017.

[70] S. W. Jolly, *Spectral Phase Manipulation of Optical Pump Pulses for mJ-Level Narrowband Terahertz Generation in PPLN*. PhD thesis, Universität Hamburg, 2017.

[71] M. Hada, J. Hirscht, D. Zhang, S. Manz, K. Pichugin, D. Mazurenko, S. Bayesteh, H. Delsim-Hashemi, K. Floettmann, M. Huening, S. Lederer, G. Moriena, C. Mueller, G. Sciaini, and D. Miller, "REGAE: New Source for Atomically Resolved Dynamics," in *Research in Optical Sciences*, 2012.

[72] E. Esarey, C. B. Schroeder, and W. P. Leemans, "Physics of laser-driven plasma-based electron accelerators," *Rev. Mod. Phys.*, vol. 81, pp. 1229–1285, 2009.

135

[73] M. Fuchs, R. Weingartner, A. Popp, Z. Major, S. Becker, J. Osterhoff, I. Cortrie, B. Zeitler, R. Hörlein, G. D. Tsakiris, U. Schramm, T. P. Rowlands-Rees, S. M. Hooker, D. Habs, F. Krausz, S. Karsch, and F. Grüner, "Laser-driven soft-x-ray undulator source," *Nature Physics*, vol. 5, pp. 826–829, 2009.

[74] P. Schmüser, M. Dohlus, J. Rossbach, and C. Behrens, *Free-Electron Lasers in the Ultraviolet and X-Ray Regime: Physical Principles, Experimental Results, Technical Realization (Springer Tracts in Modern Physics)*. Springer, 2014.

[75] G. D. Stasio, B. Gilbert, T. Nelson, R. Hansen, J. Wallace, D. Mercanti, M. Capozi, P. A. Baudat, P. Perfetti, G. Margaritondo, and B. P. Tonner, "Feasibility tests of transmission x-ray photoelectron emission microscopy of wet samples," *Review of Scientific Instruments*, vol. 71, no. 1, pp. 11–14, 2000.

[76] N. Delbos, *High Repetition Rate Laser-Plasma Accelerator: 5 Hz Electron Beam Generation and Advanced Target Design*. PhD thesis, Universität Hamburg, 2017.

[77] C. Werle, *First Undulator Experiments at the LUX Beamline: Towards a Plasma-Based Accelerator as a Soft X-ray Source*. PhD thesis, Universität Hamburg, 2018.

[78] N. Didenko, A. Konyashchenko, A. Lutsenko, and S. Tenyakov, "Contrast degradation in a chirped-pulse amplifier due to generation of prepulses by postpulses," *Opt. Express*, vol. 16, no. 5, pp. 3178–3190, 2008.

[79] Z. Bor and B. Rácz, "Group velocity dispersion in prisms and its application to pulse compression and travelling-wave excitation," *Optics Communications*, vol. 54, no. 3, pp. 165–170, 1985.

[80] K. Osvay, A. P. Kovacs, Z. Heiner, G. Kurdi, J. Klebniczki, and M. Csatari, "Angular dispersion and temporal change of femtosecond pulses from misaligned pulse compressors," *IEEE Journal of Selected Topics in Quantum Electronics*, vol. 10, no. 1, pp. 213–220, 2004.

[81] T. Oksenhendler, S. Coudreau, N. Forget, V. Crozatier, S. Grabielle, R. Herzog, O. Gobert, and D. Kaplan, "Self-referenced spectral interferometry," *Applied Physics B*, vol. 99, no. 1, pp. 7–12, 2010.

[82] P. O'Shea, M. Kimmel, X. Gu, and R. Trebino, "Highly simplified device for ultrashort-pulse measurement," *Opt. Lett.*, vol. 26, no. 12, pp. 932–934, 2001.

[83] A. E. Siegman, "How to (maybe) measure laser beam quality," in *DPSS (Diode Pumped Solid State) Lasers: Applications and Issues*, p. MQ1, Optical Society of America, 1998.

[84] J. S. Lim, *Two-dimensional signal and image processing*. Prentice Hall PTR, 1990.

[85] Z. Molnár, J. Égert, and M. Berta, "Finite element analysis of glass vacuum windows of the compass tokamak in prague," *Acta Technica Jaurinensis*, vol. 8, no. 4, pp. 330–346, 2015.

[86] T. D. Grow, A. A. Ishaaya, L. T. Vuong, A. L. Gaeta, N. Gavish, and G. Fibich, "Collapse dynamics of super-gaussian beams," *Opt. Express*, vol. 14, no. 12, pp. 5468–5475, 2006.

[87] S. P. D. Mangles, G. Genoud, M. S. Bloom, M. Burza, Z. Najmudin, A. Persson, K. Svensson, A. G. R. Thomas, and C.-G. Wahlström, "Self-injection threshold in self-guided laser wakefield accelerators," *Phys. Rev. ST Accel. Beams*, vol. 15, p. 011302, 2012.

[88] J. J. Stamnes, H. Heier, and S. Ljunggren, "Encircled energy for systems with centrally obscured circular pupils," *Appl. Opt.*, vol. 21, no. 9, pp. 1628–1633, 1982.

[89] G. Pretzler, A. Kasper, and K. Witte, "Angular chirp and tilted light pulses in cpa lasers," *Applied Physics B*, vol. 70, no. 1, pp. 1–9, 2000.

[90] G. Pariente, V. Gallet, A. Borot, O. Gobert, and F. Quéré, "Space–time characterization of ultra-intense femtosecond laser beams," *Nature Photonics*, vol. 10, no. 8, pp. 547–553, 2016.

[91] J. R. Fienup, "Phase retrieval algorithms: a comparison," *Appl. Opt.*, vol. 21, no. 15, pp. 2758–2769, 1982.

[92] P. Messner, *TBD*. PhD thesis, Universität Hamburg, 2018.

[93] O. Uteza, B. Bussière, F. Canova, J.-P. Chambaret, P. Delaporte, T. Itina, and M. Sentis, "Laser-induced damage threshold of sapphire in nanosecond, picosecond and femtosecond regimes," *Applied Surface Science*, vol. 254, no. 4, pp. 799–803, 2007.

[94] H. Xiong, T. Yu, F. Gao, X. Zhang, and X. Yuan, "Filtering characteristics of a three-lens slit spatial filter for high-power lasers," *Opt. Lett.*, vol. 42, no. 22, pp. 4593–4595, 2017.

[95] R. Lausten and P. Balling, "Thermal lensing in pulsed laser amplifiers: an analytical model," *J. Opt. Soc. Am. B*, vol. 20, no. 7, pp. 1479–1485, 2003.

[96] P. B. Johnson and R. W. Christy, "Optical constants of the noble metals," *Phys. Rev. B*, vol. 6, pp. 4370–4379, 1972.

[97] O. Loebich, "The optical properties of gold," *Gold Bulletin*, vol. 5, no. 1, pp. 2–10, 1972.

[98] N. LaBianca and J. Delorme, "High aspect ratio resist for thick film applications," in *Proceedings of SPIE vol. 2438*, 1995.

[99] S. Anisimov, "Electron emission from metal surfaces exposed to ultrshort laser pulses," *Soviet Physics JETP*, vol. 39, pp. 375–377, 1974.

[100] E. Marín, "Characteristic dimensions for heat transfer," *Latin-American Journal of Physics Education*, vol. 4, no. 1, pp. 56–60, 2010.

[101] Z. Li, K. Tsubakimoto, H. Yoshida, Y. Nakata, and N. Miyanaga, "Degradation of femtosecond petawatt laser beams: Spatio-temporal/spectral coupling induced by wavefront errors of compression gratings," *Applied Physics Express*, vol. 10, no. 10, p. 102702, 2017.

[102] S. Backus, R. Bartels, S. Thompson, R. Dollinger, H. C. Kapteyn, and M. M. Murnane, "High-efficiency, single-stage 7-khz high-average-power ultrafast laser system," *Opt. Lett.*, vol. 26, no. 7, pp. 465–467, 2001.

[103] S. Fourmaux, C. Serbanescu, L. Lecherbourg, S. Payeur, F. Martin, and J. C. Kieffer, "Investigation of the thermally induced laser beam distortion associated with vacuum compressor gratings in high energy and high average power femtosecond laser systems," *Opt. Express*, vol. 17, no. 1, pp. 178–184, 2009.

[104] D. A. Alessi, P. A. Rosso, H. T. Nguyen, M. D. Aasen, J. A. Britten, and C. Haefner, "Active cooling of pulse compression diffraction gratings for high energy, high average power ultrafast lasers," *Opt. Express*, vol. 24, no. 26, pp. 30015–30023, 2016.

[105] V. Leroux, S. W. Jolly, M. Schnepp, T. Eichner, S. Jalas, M. Kirchen, P. Messner, C. Werle, P. Winkler, and A. R. Maier, "Wavefront degradation of a 200 TW laser from heat-induced deformation of in-vacuum compressor gratings," *Opt. Express*, vol. 26, pp. 13061–13071, May 2018.

[106] U. Hahn and K. Zapfe, "Guidelines for UHV-components at DESY," tech. rep., Deutsches Elektronen-Synchrotron (DESY), 2010.

[107] D. H. Froula, C. E. Clayton, T. Döppner, K. A. Marsh, C. P. J. Barty, L. Divol, R. A. Fonseca, S. H. Glenzer, C. Joshi, W. Lu, S. F. Martins, P. Michel, W. B. Mori, J. P. Palastro, B. B. Pollock, A. Pak, J. E. Ralph, J. S. Ross, C. W. Siders, L. O. Silva, and T. Wang, "Measurements of the critical power for self-injection of electrons in a laser wakefield accelerator," *Phys. Rev. Lett.*, vol. 103, p. 215006, 2009.

[108] M. Bass *et al.*, *Handbook of optics.* McGraw-Hill, 2000.